



TECHNISCHE UNIVERSITÄT MÜNCHEN

TUM School of Engineering and Design

Numerical simulation of transcritical channel flows

Alexander Doehring

Vollständiger Abdruck der von der TUM School of Engineering and Design
der Technischen Universität München zur Erlangung des akademischen Grades eines

Doktors der Ingenieurwissenschaften (Dr.-Ing.)

genehmigten Dissertation.

Vorsitz: Prof. Wolfgang Polifke, Ph.D.
Prüfer der Dissertation: 1. Prof. Dr.-Ing. Nikolaus A. Adams
2. Prof. Dr.-Ing. habil. Stefan Hickel
3. Assoc. Prof. Jean-Pierre Hickey, Ph.D.

Die Dissertation wurde am 15.01.2024 bei der Technischen Universität München eingereicht und
durch die TUM School of Engineering and Design am 11.07.2024 angenommen.

Copyright © Alexander Doehring, 2024

All rights reserved. No part of this publication may be reproduced, modified, re-written, or distributed in any form or by any means, without the prior written permission of the author.

Released October 4, 2024
Typesetting **L^AT_EX**

ABSTRACT

Wall bounded flows with trans- or supercritical fluids are found in many technical applications. While many numerical studies have been conducted during the last two decades contributing to the understanding of transcritical flows, low cost CFD models such as Reynolds-Averaged Navier Stokes (RANS) and wall-modelled large-eddy simulations (WMLES) still have got poor prediction capabilities. In this publication-based thesis, well-resolved large-eddy simulations (LES) of transcritical channel flows are conducted. The LES are used to study the influence of strong non-linear property variations on a turbulent flow with heat transfer.

We employ our in-house code CATUM solving the fully compressible Navier-Stokes equations in conservative form. An adaptive look-up table method is used for thermodynamic and transport properties, which is more accurate than common cubic equations of state. Methane, an emerging fuel in liquid-propellant rocket engines (LRE), is utilized within this thesis. We apply a physically consistent subgrid-scale turbulence model, that is based on the Adaptive Local Deconvolution Method (ALDM) for implicit LES. A generic channel flow configuration is used to focus on the impact of non-linear thermodynamic effects on turbulent flows and on the heat transfer. On the one hand, the isothermal wall temperatures are determined to represent a cooling channel in LRE with a cold and hot wall. On the other hand, the temperatures are set to capture non-linear property variations and the pseudo-boiling within the channel geometry.

A correct prediction of the heat transfer enhancement or deterioration using RANS is still ongoing research. In the first study we pose the question, if these difficulties also hold for channel flows using transcritical methane. For this purpose, we perform RANS of a transcritical channel flow with methane and compare the results with well-resolved LES. The focus of the comparison is on the mean velocity and temperature profiles, as well as on the resulting wall shear stress and wall heat flux.

The turbulence modelling has reportedly a significant influence on the prediction capabilities of RANS or WMLES. Classical turbulence models, here in particular the closure for the momentum and energy equations, are derived from canonical flows at ideal conditions, which might contribute to the bad prediction capabilities in flows with strong non-linear property variations. In the second study we use two well-resolved LES to analyse the turbulent heat and momentum transfer in transcritical channel flows using methane. A new turbulent Prandtl number definition based on the enthalpy is proposed, which is only slightly affected by the pseudo-boiling compared to the common definitions from literature.

In the last study a comprehensive investigation of the turbulent momentum boundary layer in transcritical flows is conducted. Seven well-resolved LES are performed covering a variation of the Reynolds number, the bulk pressure and the pseudo-boiling position within the channel. After performing an averaging of the streamwise momentum equation four unclosed terms are identified. Based on the results, one of the unclosed terms, has been identified to be essential for the

ABSTRACT

turbulence modelling. The statistical analysis of all cases demonstrates the influence of non-linear thermodynamics on turbulent momentum boundary layers, which provides a foundation for the development of future low-cost turbulence models.

ZUSAMMENFASSUNG

Wandgebundene Strömungen mit trans- oder überkritischen Fluiden sind in vielen technischen Anwendungen zu finden. Obwohl in den letzten zwei Jahrzehnten zahlreiche numerische Studien durchgeführt wurden, die zum Verständnis transkritischer Strömungen beigetragen haben, haben kostengünstige CFD-Methoden, wie Reynolds-Averaged Navier Stokes (RANS) und wandmodellerte Grobstruktursimulationen (WMLES), immer noch schlechte Vorhersagefähigkeiten. In dieser veröffentlichungsbasierten Dissertation werden gut aufgelöste Grobstruktursimulationen (large-eddy simulation, LES) von transkritischen Kanalströmungen durchgeführt. Die durchgeführten LES werden verwendet, um den Einfluss von starken Änderungen der Fluideigenschaften auf eine turbulente Strömung mit Wärmeübertragung zu untersuchen.

Wir verwenden unseren institutseigenen Strömungslöser CATUM zur Lösung der kompressiblen Navier-Stokes-Gleichungen in konservativer Form. Adaptive Tabellen wurden für die Modellierung der thermodynamischen Fluideigenschaften verwendet. Die generierten Tabellen geben die Fluideigenschaften genauer wieder als gängige kubischen Zustandsgleichungen. Methan, welches ein aufkommender Treibstoff für Flüssigtreibstoffraketenantriebe (LRE) ist, wird im Rahmen dieser Arbeit benutzt. Wir verwenden ein physikalisch konsistentes Turbulenzmodell für den Feinstruktur-Spannungstensor (SGS), das auf der Methode der adaptiven lokalen Dekonvolution (ALDM) basiert. Eine generische Kanalströmungskonfiguration wird verwendet, um den Fokus auf die Auswirkungen nichtlinearer thermodynamischer Fluideigenschaften auf turbulente Strömungen mit Wärmeübertragung zu legen. Einerseits wurden die isothermen Wandtemperaturen ausgewählt, um einen Kühlkanal mit einer kalten und einer heißen Wand zu repräsentieren. Andererseits wurden die Temperaturen bestimmt, um nichtlineare Änderungen der Fluideigenschaften und das Pseudosieden innerhalb der Kanalgeometrie zu erfassen.

Eine korrekte Vorhersage der Verbesserung oder Verschlechterung der Wärmeübertragung mit Hilfe von RANS ist noch Gegenstand der Forschung. In der ersten Studie stellen wir uns die Frage, ob diese Schwierigkeiten auch für Kanalströmungen mit transkritischem Methan gelten. Zu diesem Zweck haben wir RANS auf eine transkritische Kanalströmung mit Methan angewendet und die Ergebnisse mit einer gut aufgelösten LES verglichen. Der Schwerpunkt des Vergleichs liegt auf den mittleren Geschwindigkeits- und Temperaturprofilen, sowie auf den resultierenden Wandschubspannungen und Wandwärmeströmen.

Die Turbulenzmodellierung hat einen erheblichen Einfluss auf das Vorhersagevermögen von RANS oder WMLES. Klassische Turbulenzmodelle, hier insbesondere die Schließung der Impuls- und Energiegleichung, werden basierend auf kanonischen Strömungen unter idealen Bedingungen entwickelt. Das kann zu schlechtem Vorhersagevermögen in Strömungen mit starken nichtlinearen Fluideigenschaften beitragen. In der zweiten Studie verwenden wir zwei gut aufgelöste LES zur Analyse des turbulenten Wärme- und Impulsübergangs in transkritischen Kanalströmungen mit Methan. Eine neue Definition der turbulenten Prandtl Zahl auf der Grundlage der Enthalpie wird

vorgeschlagen. Diese Definition ist im Gegensatz zu üblichen Formulierungen aus der Literatur nur geringfügig vom Pseudosieden beeinflusst.

In der letzten Studie wurde eine umfassende Untersuchung der turbulenten Impulsgrenzschicht in transkritischen Strömungen durchgeführt. Hierfür dienen sieben gut aufgelöste LES, die eine Variation der Reynoldszahl, des Gesamtdrucks und der Pseudosiededeposition abdecken. Nach dem Mitteln der Impulsgleichung in Strömungsrichtung erhalten wir vier neue Terme. Auf der Grundlage der Ergebnisse wurde einer der Terme als wesentlich für die Turbulenzmodellierung identifiziert. Die statistische Analyse aller Fälle zeigt den Einfluss der nichtlinearen Thermodynamik auf turbulente Impulsgrenzschichten und bildet eine Grundlage für die Entwicklung künftiger kostengünstiger Turbulenzmodelle.

DANKSAGUNG

An dieser Stelle möchte ich Personen danken, die ganz wesentlich zum Gelingen dieser Arbeit beigetragen haben.

Zuallererst möchte ich mich bei Professor Adams für die Ermöglichung der Promotion sowie die Betreuung und Unterstützung der letzten Jahre bedanken. Sie haben mir wissenschaftliche Freiheiten gelassen und haben sich stets Zeit für Fragen genommen. Zusätzlich haben Sie mir die Möglichkeit gegeben, mehrere internationale Konferenzen zu besuchen und einen Auslandsaufenthalt in Kanada durchzuführen. Danke!

Ein großer Dank geht auch an Steffen Schmidt, Leiter der Gasdynamik-Gruppe. Bei Fragen zu Catum hast du immer ein offenes Ohr gehabt und dein Wissen auf dem Gebiet der Numerik hat viel Licht ins Dunkle gebracht.

Für die Unterstützung und erfolgreiche Zusammenarbeit möchte ich insbesondere Thomas danken. Du hast mir Perspektiven gezeigt, wenn ich nicht mehr weiter wusste und aufbauende Worte gehabt, wenn sich ein Motivationstief breitgemacht hat. Das gemeinsame Erstellen von Folien für SFB-Treffen, die fachlichen und fachübergreifenden Diskussionen werden mir immer in Erinnerung bleiben.

Ich bedanke mich bei allen Kollegen für die schöne Zeit am Institut. Die gemeinsamen Kaffeepausen, die Gespräche beim Mittagessen in der Mensa und die gemeinsamen Aktivitäten außerhalb des Arbeitsplatzes haben die Promotionszeit viel angenehmer gemacht. Mein Dankeschön geht besonderes an Thomas, Theresa, Raffaele und Thomas H.. Zusätzlicher Dank gebührt Thomas für das Korrekturlesen dieser Arbeit und Theresa für die Latex-Vorlage.

Der wichtigste Dank geht an meine Familie. Ohne die Unterstützung meiner Eltern während meines Studiums und der Promotion wäre ich nicht so weit gekommen. Euer Rückhalt hat zum Erfolg der Arbeit beigetragen. Willi und Erik, ihr habt mir geholfen, meinen Kopf von der Arbeit freizubekommen und mit euch habe ich viele schöne Momente außerhalb der Arbeit erlebt. Charlotte, du warst trotz unzähliger Abend- und Wochenendsitzungen immer unterstützend an meiner Seite und hast mich auf den letzten Metern motiviert. Dankeschön!

PUBLICATIONS

This thesis is partly based on publications, which have been produced during this PhD. Reproduced text sections and figures are marked and permission from the corresponding publisher has been obtained.

PEER-REVIEWED JOURNAL PAPERS

1. **A. Doehring**, T. Kaller, S. J. Schmidt, N. A. Adams (2021) Large-eddy simulation of turbulent channel flow at transcritical states. *International Journal of Heat and Fluid Flow*, **89**, 108781, doi:10.1016/j.ijheatfluidflow.2021.108781.
2. R. Olmeda, **A. Doehring**, C. Stemmer (2022) Study and Application of Wall-Roughness Models in LES Flows. *International Journal of Heat and Fluid Flow*, **95**, 108948, doi:10.1016/j.ijheatfluidflow.2022.108948.
3. **A. Doehring**, S. J. Schmidt, N. A. Adams (2023) Momentum boundary layers in transcritical channel flows. *International Journal of Heat and Fluid Flow*, **103**, 109201, doi:10.1016/j.ijheatfluidflow.2023.109201.
4. **A. Doehring**, T. Kaller, S. J. Schmidt, N. A. Adams (2024) Influence of wall shear stress on the secondary flow in square ducts. *International Journal of Heat and Fluid Flow*, **105**, 109240, doi:https://doi.org/10.1016/j.ijheatfluidflow.2023.109240.

PEER-REVIEWED BOOK CHAPTER CONTRIBUTIONS

1. T. Kaller*, **A. Doehring***, S. Hickel, S. J. Schmidt and N. A. Adams (2021) Assessment of RANS turbulence models for straight cooling ducts: secondary flow and strong property variation effects. In N. A. Adams, W. Schröder, R. Radespiel, O. Haidn, T. Sattelmayer, C. Stemmer, B. Weigand (eds) *Future Space-Transport-System Components under High Thermal and Mechanical Loads: Results from the DFG Collaborative Research Center TRR40, Notes on Numerical Fluid Mechanics and Multidisciplinary Design*, vol 146, Springer, Cham. doi:10.1007/978-3-030-53847-7_20.

CONFERENCE PROCEEDINGS

1. **A. Doehring**, S. J. Schmidt, N. A. Adams (2018) Numerical investigation of transcritical turbulent channel flow. In *54th AIAA/SAE/ASEE Joint Propulsion Conference*, Cincinnati, USA. doi:10.2514/6.2018-4768.

2. **A. Doehring**, S. J. Schmidt, N. A. Adams (2019) Large-eddy simulation of turbulent channel flow at transcritical states. In *11th International Symposium on Turbulence and Shear Flow Phenomena (TSFP-11)*, Southampton, United Kingdom.
3. **A. Doehring**, T. Kaller, S. J. Schmidt, N. A. Adams, (2022). Influence of wall shear stress on secondary flow in square ducts. In *12th International Symposium on Turbulence and Shear Flow Phenomena (TSFP12)*, Osaka, Japan.
4. S. Soller, F. Grauer, K. Vollmer, W. Zeiss, M. T. Scelzo, J.-B. Gouriet, A. de Crombrughe, K. Claramunt, C. Dinescu, L. Temmerman, **A. Doehring**, S. J. Schmidt, J. Steelant (2022). Heat Transfer Phenomena in Additively Manufactured Cooling Channels. In *Space Propulsion Conference 2022*, Estoril, Portugal.
5. S. Soller, M. T. Scelzo, J.-B. Gouriet, A. de Crombrughe, C. Dinescu, L. Temmerman, **A. Doehring**, S. Schmidt, J. Steelant (2023). Investigation of Heat Transfer and Nucleate Boiling of Ethanol in Additively Manufactured Cooling Channels. In *Aerospace Europe Conference 2023 - 10th EUCASS - 9th CEAS*, Lausanne, Switzerland.

PEER-REVIEWED TECHNICAL REPORTS

1. **A. Doehring**, S. J. Schmidt, N. A. Adams (2018) Large-eddy Simulation of a Transcritical Turbulent Channel. In *Annual Report 2018 of the Sonderforschungsbereich/Transregio 40*.
2. T. Kaller, **A. Doehring**, N. A. Adams (2019) Numerical investigation of a high-aspect-ratio cooling duct flow with different RANS turbulence models. In *Annual Report 2019 of the Sonderforschungsbereich/Transregio 40*.

CONTENTS

Abstract	iii
Zusammenfassung	v
Danksagung	vi
Publications	ix
1. Introduction	1
1.1. Motivation	1
1.2. Transcritical fluids	2
1.3. Numerical studies	5
1.4. Objectives and Outline	7
2. Physical Model	9
2.1. Governing Equations	9
2.2. Thermodynamic modelling	10
3. Numerical Method	13
3.1. Finite Volume Method	13
3.2. Time integration	13
3.3. Numerical Flux	14
3.3.1. Reconstruction	15
3.3.2. Central scheme	16
3.3.3. Upwind-biased Scheme	16
3.3.4. Sub-grid scale modelling	17
4. Accomplishments	19
4.1. Assessment of RANS	19
4.1.1. Summary of the publication	19
4.1.2. Individual contribution	20
4.2. Turbulent Prandtl number	21
4.2.1. Summary of the publication	21
4.2.2. Individual contribution	23
4.3. Momentum boundary layers in transcritical channel flows	24
4.3.1. Summary of the publication	24
4.3.2. Individual contribution	26

CONTENTS

5. Concluding remarks	27
5.1. Summary	27
5.2. Outlook	28
A. Selected publications	31
A.1. Assessment of RANS Turbulence Models for Straight Cooling Ducts: Secondary Flow and Strong Property Variation Effects	31
A.1.1. Rights and permissions:	31
A.1.2. Manuscript	31
A.2. Large-eddy simulation of turbulent channel flow at transcritical states	45
A.2.1. Rights and permissions:	45
A.2.2. Manuscript	45
A.3. Momentum boundary layers in transcritical channel flows	58
A.3.1. Rights and permissions:	58
A.3.2. Manuscript	60
Bibliography	83

1. INTRODUCTION

This thesis summarises my work as a research assistant at the Chair of Aerodynamics and Fluid Mechanics of the Department of Mechanical Engineering at the Technical University of Munich. I have been investigating transcritical channel flows within the collaborative research centre SFB-TRR40¹, which was funded by the German Research Foundation DFG. The comprehensive aim of the SFB-TRR40 has been the investigation of the 'technological foundations for the design of thermally and mechanically highly loaded components of future space transport systems'. The collaborative work was focusing on liquid-propellant rocket engine (LRE) propulsion. The specific topic of my sub-project within the SFB-TRR40 has been 'heat transfer in nozzle cooling channels', which is investigated using computational fluid dynamics (CFD).

1.1. MOTIVATION

Today's requirements for propulsion system demand for energy efficient processes in order to reduce greenhouse gas emission. One possibility to enhance the efficiency of propulsion systems is to increase the operating pressure. In liquid rocket engines this is founded by the proportionality between the operating pressure and the specific impulse [1]. A similar increase of the efficiency is found in gas turbines and diesel engines. According to Huzel and Huang [2] an increase in operating pressure p_{op} leads to higher heat loads \dot{q} , following

$$\dot{q} \propto p_{op}^{0.8}. \quad (1.1)$$

Thus, LRE's face extreme thermal conditions during the operation time including temperatures up to 3600 K and heat fluxes up to 160 MW m⁻², demanding for an efficient structural cooling. One approach to cool the structure is to feed the propellant through milled passages in the combustion chamber and nozzle wall, which is referred to as regenerative cooling. Passing through the cooling channels the propellant absorbs the heat and the coolant's enthalpy increases. Thus, a performance loss is reduced, since the heated propellant is fed to the injector, where it is injected into the combustion chamber. Other significant advantages of the regenerative cooling method are the limitless operation time and the requirement of a thin combustion chamber wall with a high conductive material for a better heat exchange, which results in less weight. In Fig. 1.1a a cut through a Vulcain engine combustion chamber wall is shown, exposing its rectangular cooling channels. The combustion chamber wall is made of a copper alloy CuAgZr liner and a galvanic deposited nickel outer shell. The thin inner copper liner is exposed to the high temperatures arising from the combustion on the one side and to a cryogenic coolant on the other side. Hence, the thin copper wall, which is not thicker than 1 mm, has to endure severe thermal stresses. If

¹<http://www.sfbtr40.de/>

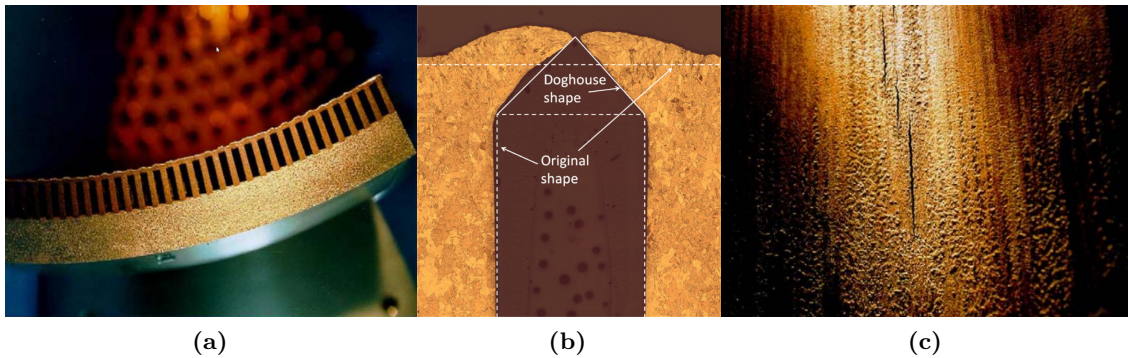


Figure 1.1.: (a) A cut through a combustion chamber wall by Haidn [3], reprinted with permission of NATO STO (© NATO STO). (b) Cut through a cooling channel illustrating the dog-house effect by Hötte et al. [4], reprinted under CC BY 4.0 Deed. (c) Longitudinal failure in a combustion chamber wall by Haidn [3] reprinted with permission of NATO STO (© NATO STO).

the cooling efficiency decreases or breaks down, the wall temperature will increase, which results in plastic deformation, a cooling channel bulging and localised wall thinning. This constitutes to the so-called *dog-house* effect (Fig. 1.1b). At an advanced stage this may lead to longitudinal cracks, see Fig. 1.1c. In consequence, a thorough understanding of the flow within the cooling channel is essential to avoid any malfunction, and ensure a save and successful mission.

1.2. TRANSCRITICAL FLUIDS

One important parameter, which has to be controlled in LRE cooling channels in order to prevent any *dog-house* effect is the wall temperature. It is a result of the turbulent flow and the heat transfer interacting with each other within the cooling channels. Both are significantly influenced by the prevalent fluid properties. Firstly, the turbulent flow is affected by the change in density and viscosity, hence, causing a change in convective heat transfer. Secondly, the heat transfer is directly affected by changes in density, thermal conductivity and specific heat capacity. As a result, the heat transfer can be either enhanced or deteriorated, which has to be incorporated in to the design of LRE.

A typical fuel and coolant in LRE is liquid hydrogen (LH2) used for example in the Space Shuttle Main Engine or in the Vulcain engine. Although LH2 has a high specific impulse I_{sp} in combination with liquid oxygen (LOX), it exhibits a low density and a very low boiling point. An alternative fuel is liquid methane (LCH4), which is applied in the Raptor rocket by SpaceX, Prometheus rocket by Ariane group and the Zhuque-2 rocket by LandSpace. Methane has the highest specific impulse among hydrocarbons and it features better storage properties due to a higher density and a higher boiling point compared to hydrogen. Additionally, the lack of hydrogen embrittlement allows for light-weight storage tanks. Furthermore, methane is supplied as a liquefied natural gas (LNG), which is widely used in the industry and can be produced on Mars through hydrogenation. However, the use of methane as coolant poses the challenge, that

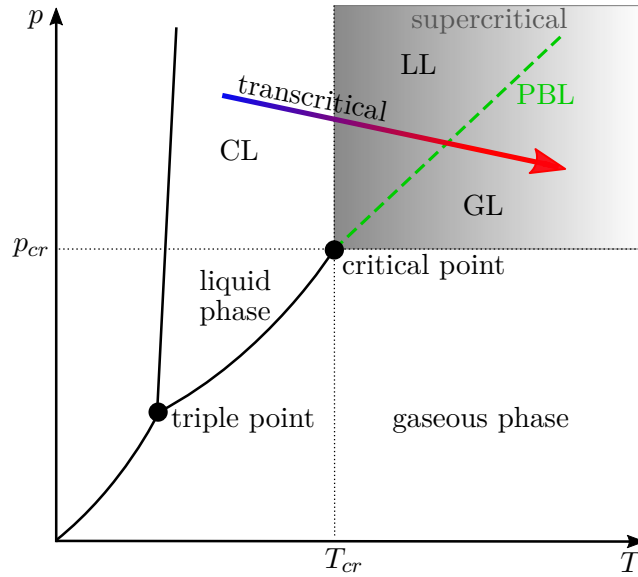


Figure 1.2.: Generic phase diagram.

the operating conditions of regenerative cooling channels are slightly above the critical point compared to hydrogen operated LRE.

The coolant in liquid rocket engines is stored at a cryogenic temperature, which is below the critical temperature ($T < T_{cr}$) and at high pressure above the critical pressure ($p > p_{cr}$). At these conditions the fluid is referred to as a *compressed liquid* (CL). Passing through the cooling channels the coolant temperature increases due to the heat flux over the hot wall surpassing its critical temperature ($T > T_{cr}$). The pressure stays above the critical pressure p_{cr} , despite the arising pressure drop, which emerges due to wall friction. Now, the fluid is at supercritical state, since both, the pressure and temperature, are above the critical point. The supercritical fluid features a gas-like diffusivity, a liquid-like density as well as a vanishing surface tension, which is a consequence of the high pressure environment. The supercritical state can be further subdivided into a *liquid like* (LL) and *gas like* (GL) state [5, 6]. Pseudo-boiling is identified between these two sub-states, which is analogously to the phase transition crossing of the vapour-liquid coexistence line. To this end a widom or pseudo-boiling line (PBL) [7] is introduced. A fluid is termed *transcritical* undergoing a pseudo phase transition from CL, over LL fluid, to GL fluid crossing the PBL. The state transition is visualised in a generic phase diagram in Fig. 1.2. In the vicinity of the critical point the relationship between the pressure, temperature and density is modified by intermolecular repulsive forces. These forces lead to strong non-linear effects, that cannot be modelled using an ideal gas law, thus, a more suitable equation of state (EOS) is needed. Furthermore, thermodynamic properties as for instance the internal energy, viscosity and specific heat capacity have to account for high pressure effects.

In Fig. 1.3 the density, specific heat capacity at constant pressure, viscosity and the speed of sound of methane are shown. Two different pressure values are included, since the fluid properties strongly depend on the distance to the critical point. For methane the critical point is at approximately 46 bar. Thus, the pressure of 50 bar represents the fluid behaviour close

1. INTRODUCTION

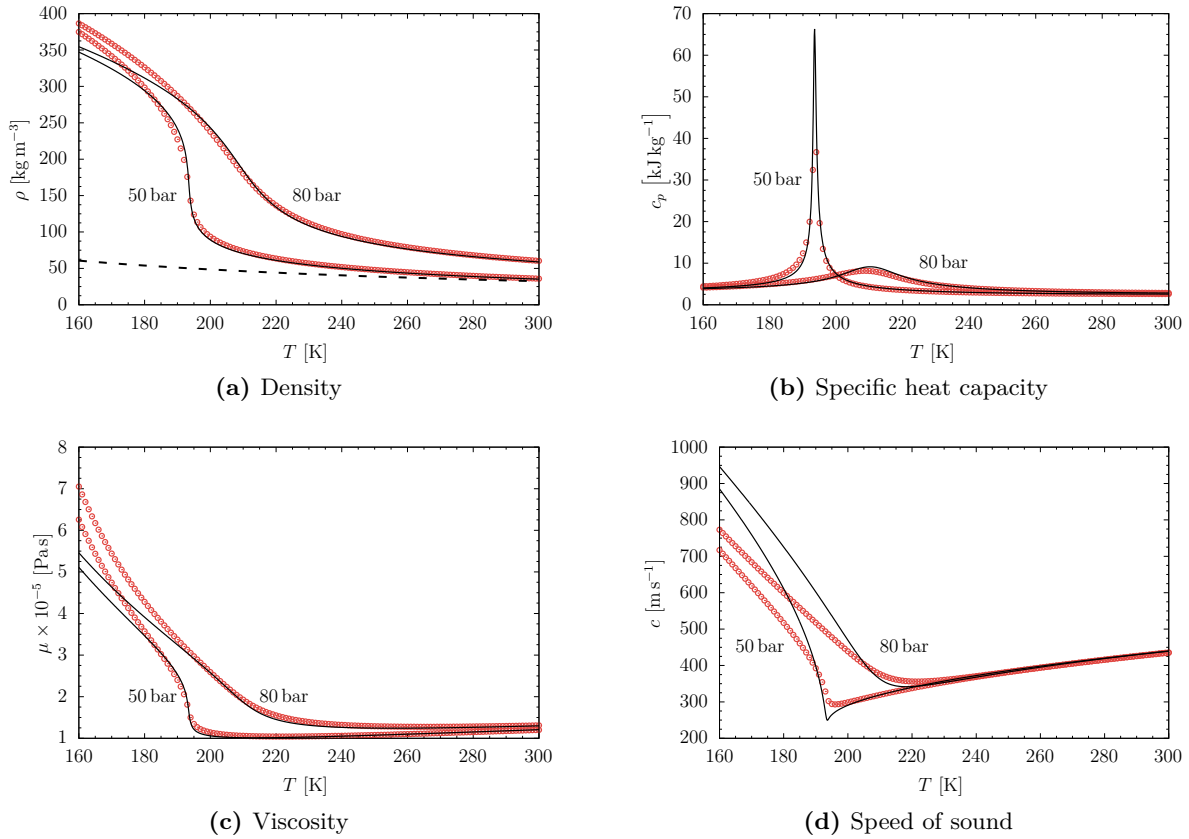


Figure 1.3.: Thermodynamic data of methane using Peng-Robinson EOS (\circ) [8] compared to NIST data base (—) [9] for a pressure of 50 bar and 80 bar, respectively. The ideal gas law is included for the density (---).

to the critical point and the pressure of 80 bar the behaviour far away from the critical point. The density is modelled using the Peng-Robinson cubic equation of state [8], which is a van der Waals type of EOS describing the relationship between pressure, density and temperature. The caloric properties are obtained by employing a departure function formalism [10, 11]. The transport properties viscosity and heat conductivity are calculated with the correlations by Chung *et al.* [12]. As a reference, we use fluid properties obtained from REFPROP/NIST [9]. For methane REFPROP employs the Helmholtz based EOS by Setzmann and Wagner [13]. Sharp changes are present for all quantities at approximately 193 K and 50 bar, which is the pseudo-boiling temperature defined by the peak position of the heat capacity [7]. With increasing pressure, hence, larger distance to the critical point the sharp changes are getting more moderate. For clarification, using the ideal gas law for the density is not suitable to capture the real gas behaviour, see Fig. 1.3a. Furthermore, the non-linear behaviour induces a high speed of sound at low temperatures, which reduces the time step in compressible CFD codes using the CFL criterion.

As it is shown in Fig. 1.3, the change in fluid properties close to the critical point are stronger, hence, a prediction of heat transfer enhancement or deterioration is more demanding for methane. For this reason, an enhanced understanding of transcritical channel flows with heat transfer prevents cooling failures and ensures a safe mission.

1.3. NUMERICAL STUDIES

Performing experimental studies at high pressure conditions is challenging, due to technical difficulties and safety reasons. As a result, experimental data on turbulent statistics and heat transfer, suitable for the development of reliable low-cost turbulence models, are scarce. For this reason, high fidelity numerical data is required to understand the effect of non-linear thermodynamics on turbulent flows in order to improve low-cost turbulence models. In this context multiple numerical studies have been performed. The following section is based on Doehring et al. [14, 15] summarizing a portion of the research relevant for this thesis.

Pizzarelli [16] provided a review of the research on the heat transfer of supercritical fluids, in particular on the heat transfer deterioration. Based on the collected work, he concluded, that Reynolds-Averaged Navier Stokes (RANS) simulations are not able to predict the onset of heat transfer deterioration and that the obtained results vary significantly depending on the used turbulence model. In addition, no heat transfer correlation was capable of predicting the heat transfer correctly. Similar statements have been already made nine years ago by Yoo [17] and twenty years ago by Pioro et al. [18], indicating the existing difficulty in prescribing the heat transfer in transcritical flows.

One of the first direct numerical simulations (DNS) of supercritical wall bounded flows have been performed by Bae et al. [19, 20]. They investigated an annular flow of supercritical CO₂ with constant wall heat flux. They observed a significant Reynolds shear stress reduction at the hot wall due to the strong property variations. Thus, the flow was stabilized leading to a reduction of turbulence. Buoyancy was found to reinforce or weaken the production of turbulence. Similar results have been obtained by Nemati et al. [21] with a DNS of a heated turbulent pipe flow with CO₂ at supercritical pressure. They ascertained a decrease of turbulent kinetic energy, which was caused by flow acceleration at the hot wall due to thermal expansion. Peeters et al. [22] concluded, that near wall streaks and streamwise vortices, which are contributing to turbulence, are affected by local property variations. Thus, turbulent motion was increased at the cold wall and decreased at the hot wall, leading to laminarization.

Ribert et al. [23] extended a WENO scheme, which is suitable for any equation of state, in order to capture large density gradients present in transcritical flows. Their large-eddy simulation (LES) results showed very elongated ligaments in the streamwise direction with a deep penetration in the wall-normal direction.

Ma et al. [24] used an entropy-stable double-flux model for DNS of a transcritical channel flow in order to avoid spurious pressure oscillations, which have been observed in trans- and supercritical flows by Terashima et al. [25]. Since the flux calculation is non-conservative, they provided a comparison of the thermodynamic properties with a fully conservative formulation. Differences are visible at the hot wall, where the temperature is above the pseudo-boiling temperature. This discrepancy is attributed to the energy conservation, which is not satisfied.

In addition, they observed the presence of a logarithmic scaling of the structure function and a k^{-1} scaling of the energy spectra, which supports the attached-eddy hypothesis in transcritical flows. Matheis *et al.* [26] included a comparison between a fully conservative (FC) and a quasi conservative (QC) formulation by replacing the energy equation with a pressure evolution equation [25]. The numerical 1-D advection-diffusion test case of a contact discontinuity has shown, that for a coarse grid the QC formulation omits pressure fluctuations, but introduces an error in the temperature distribution. With increasing grid resolution, spurious oscillations of the FC method are decreasing and the error in the temperature profile of the QC method is converging towards the FC solution.

A heated transcritical turbulent boundary layer over a flat plate has been investigated by Kawai [27] using DNS. His study shows large density fluctuations, which are induced by strong changes of thermodynamic properties in the vicinity of the pseudo-boiling. Furthermore, these fluctuations evoke non-negligible Favre-averaged velocity fluctuations, which are associated with a turbulent mass flux. In addition, he employed velocity transformations such as the van Driest transformation [28], the semi-local scaling by Huang *et al.* [29] and the transformation by Trettel and Larsson [30] without success. The objective has been to obtain a velocity distribution following the classical logarithmic layer profile for incompressible flows. The deficiency of the mentioned velocity transformations has also been ascertained by Ma *et al.* [24].

Kim *et al.* [31] controlled the pseudo-boiling position by changing the temperature difference between the walls in a DNS of a turbulent channel flow. Large streamwise turbulent structures based on Q-criterion iso-surfaces have been identified close to the walls, affirming the LES results by Ribert *et al.* [23]. This leads to the necessity of larger computational domains, thus, higher numerical costs for the study of transcritical channel flows. Despite the reduction of turbulent intensity at the hot wall, they observed intensified thermodynamic fluctuations and strong ejections of dense fluids into the channel core.

A DNS study by Chen *et al.* [32] of a turbulent channel has been performed using a dense gas in the framework of organic rankine cycle systems. They identified an increase of the wall normal and spanwise Reynolds shear stress components compared to a turbulent channel flow with an ideal gas. The turbulent energy transport and scaling laws in transcritical channel flows using DNS have been investigated by Li *et al.* [33]. They observed local equilibrium of turbulent kinetic energy transport in transcritical flows in the logarithmic layer. Thermal boundary layers in transcritical flows have been investigated by Guo *et al.* [34] applying DNS. They observed wider temperature structures in the gas-like region and contracted structures in the liquid-like regions. Close to the pseudo-boiling line they identified an enhancement of thermodynamic fluctuations, which has also been ascertained by Kim *et al.* [31].

Despite the various studies mentioned above, it is still not entirely clear, how the variable thermophysical properties of a heated or cooled fluid at supercritical pressure affect turbulent motions. This is due to the fact, that we are dealing with a multi-physics problem, which is grounded on the interplay between non-linear thermodynamics, turbulent flow and heat transfer. The lack of understanding of such systems can be demonstrated by the poor prediction capabilities of turbulence models in RANS [16, 17] and the large number of proposed mean velocity transformations to fit the incompressible mean velocity profiles [30, 35, 36, 37].

Recently, Indelicato and Creta [38] employed wall functions based on the equilibrium boundary

layer assumption in LES of transcritical pipe flow. They compared the wall modelled results with wall-resolved LES and observed a deviation in skin friction of 10 to 25%. Based on their assessment the source for the deviation is twofold. The first issue is the equilibrium assumption, which accounts up to 20% of the error. And the second source of error is the van Driest transformation used within the wall function. The latter is related to the *absence of a universal scaling for trans- and supercritical* mentioned above.

1.4. OBJECTIVES AND OUTLINE

The few selected numerical studies mentioned above show, that a lot of effort has been made over the last decades to understand transcritical flows with its unique fluid properties. But it also highlights the prevalent lack of understanding, what kind of influence strong property variations have on the turbulent flow and the heat transfer. Most of the mentioned studies are based on DNS simulations, which are limited by the Reynolds number, since the computational effort scales with Re^3 . In transcritical channel flows the molecular Prandtl number is highly non-linear with values above unity. Applying the relation between the Kolmogorov and Batchelor scales introduced by Monin and Yaglom [39] leads to the following dependence on the Prandtl number: $(1/Pr)^{0.5}$. Thus, with increasing Prandtl number a higher resolution is required to resolve the smallest thermal scales, resulting in even higher computational costs for transcritical DNS. In this regard, LES is an alternative to DNS, which allows to obtain higher Reynolds numbers and is a trade-off between modelled and resolved scales as well as computational costs.

For this reason, this publication-based thesis aims to investigate transcritical channel flows by means of well-resolved large-eddy simulations. The intention is to use the obtained insights and the data from these simulations for the development of future models in wall-modelled LES (WMLES), which is outside the scope of this thesis. The analysis of the performed LES is focused on the momentum and thermal boundary layer providing observations of the turbulent statistics and structures. As a representative of a future hydrocarbon fuel, methane was used as working fluid for all simulations, which includes the correct representation of its thermodynamic and transport properties. In total three parameters have been adjusted to study transcritical channel flows.

- Bulk pressure: This parameter controls the intensity of the pseudo-boiling.
- Pseudo-boiling position: This setting defines where strong property variations are located within the boundary layer.
- Reynolds number: This parameter helps to identify a Reynolds number dependence of the made observations.

The main objective is to analyse the interaction between transcritical fluids, the heat transfer and the turbulent flow under LRE conditions. To this end, in the first publication [40] we compared results obtained from RANS and LES with each other. The turbulent heat and momentum transfer is investigated in the second publication [41]. Finally, a thorough analysis of transcritical momentum boundary layers including unclosed terms has been performed in the third publication [15].

1. INTRODUCTION

The outline of this thesis is as follows. In Chapter 2 the governing equations and thermodynamic modelling is presented. The numerical modelling used for the LES is illustrated in Chapter 3. Chapter 4 summarizes the main findings in the three publications the thesis is based on. The discussions in Chapter 5 highlight the key features of the current work and provide an outlook for future research.

2. PHYSICAL MODEL

In the following chapter the governing equations and the thermodynamic modelling are summarized. This holds for the LES and the RANS, which have been performed with the in-house code CATUM [42, 43, 44] and ANSYS FLUENT [45, 46], respectively. This chapter is based on Doehring et al. [41, 15].

2.1. GOVERNING EQUATIONS

The governing equations used in the simulation are the continuity, momentum and total energy equations for compressible flows in fully conservative (FC) formulation.

$$\partial_t \rho + \nabla \cdot (\rho \mathbf{u}) = 0, \quad (2.1)$$

$$\partial_t (\rho \mathbf{u}) + (\mathbf{u} \cdot \nabla) \rho \mathbf{u} = -\nabla p + \nabla \cdot \mathbf{T} + \mathbf{f}, \quad (2.2)$$

$$\partial_t (E) + (\mathbf{u} \cdot \nabla) E = -(\mathbf{u} \cdot \nabla) p + \nabla \cdot (\mathbf{u} \cdot \mathbf{T} - q) + \mathbf{u} \cdot \mathbf{f}, \quad (2.3)$$

with the density ρ , pressure p , total energy E and the velocity vector $\mathbf{u} = (u, v, w)$. The total energy consists of the specific internal energy e and the kinematic energy e_{kin}

$$E = \rho (e + e_{kin}) = \rho \left(e + \frac{1}{2} \|\mathbf{u}\|^2 \right). \quad (2.4)$$

No gravitational forces are taken into account, thus, no potential energy is included. The viscous stress tensor \mathbf{T} for a Newtonian fluid using the Stokes' hypothesis is defined as

$$\mathbf{T} = \mu \left[(\nabla \mathbf{u} + (\nabla \mathbf{u})^T) - \frac{2}{3} \mathbf{I} (\nabla \cdot \mathbf{u}) \right], \quad (2.5)$$

with the identity matrix \mathbf{I} .

The heat flux is defined by Fourier's law

$$\mathbf{q} = -\lambda \nabla T, \quad (2.6)$$

with the thermal conductivity λ .

For channel flows with periodic boundary conditions in streamwise direction, a body force is required in order to maintain a constant mass flux. For this reason, a body force $\mathbf{f} = f \delta_{i1}$ based on Brun et al. [47] is introduced in the momentum and energy equations. The Kronecker-Delta function δ_{ij} is unity if $i = j$ and zero otherwise.

2.2. THERMODYNAMIC MODELLING

Methane was used as a working fluid in all performed simulations. In Table 2.1 the parameters of methane are summarized. The thermodynamic and transport properties of methane are modelled with an adaptive look-up table method based on the REFPROP database [9]. In total, two tables with different constraints are generated. One table is generated for the fluid domain imposing density and internal energy constraints, since the solver provides the density and internal energy by solving the compressible Navier-Stokes equations. A second table is provided for the boundary conditions, where a pressure and temperature value is imposed. The generated tables are not equidistant using an additional quadtree for a fast localization of data points within the table. The table generation method is similar to Liu *et al.* [48]. The resolution of the tables is increased until a tree depth of seven is reached or until an accuracy of 0.01% is achieved.

The accuracy of the used look-up tables is shown in Fig. 2.1 by means of the density, viscosity, speed of sound and specific heat capacity at constant pressure. Two different pressure values 50 bar and 80 bar are presented in order to express the degree of non-linearity. The tables are in good agreement with the NIST data base [9]. All properties feature an unsteadiness at the pseudo-boiling temperature, which is determined by means of the heat capacity peak $c_{p,max}$. The speed of sound in Fig. 2.1d ascends steeply with decreasing temperature. This has a major influence on the acoustic time step limitation, resulting in a time step of the order of 10^{-10} s in the performed LES. The look-up table method was used for all transcritical channel flow simulations performed with the in-house flow solver CATUM and the commercial RANS solver ANSYS FLUENT.

Table 2.1.: Thermodynamic properties of methane [49, 50].

Property	Methane
Boiling point (1.013 bar)	112 K
Freezing point	91 K
Density at boiling point	422.5 kg m ⁻³
Critical temperature	190.06 K
Critical pressure	4.6 MPa
Critical real gas factor	0.286 288 7
acentric factor	0.011 42
Molecular mass	16.043 kg kmol ⁻¹

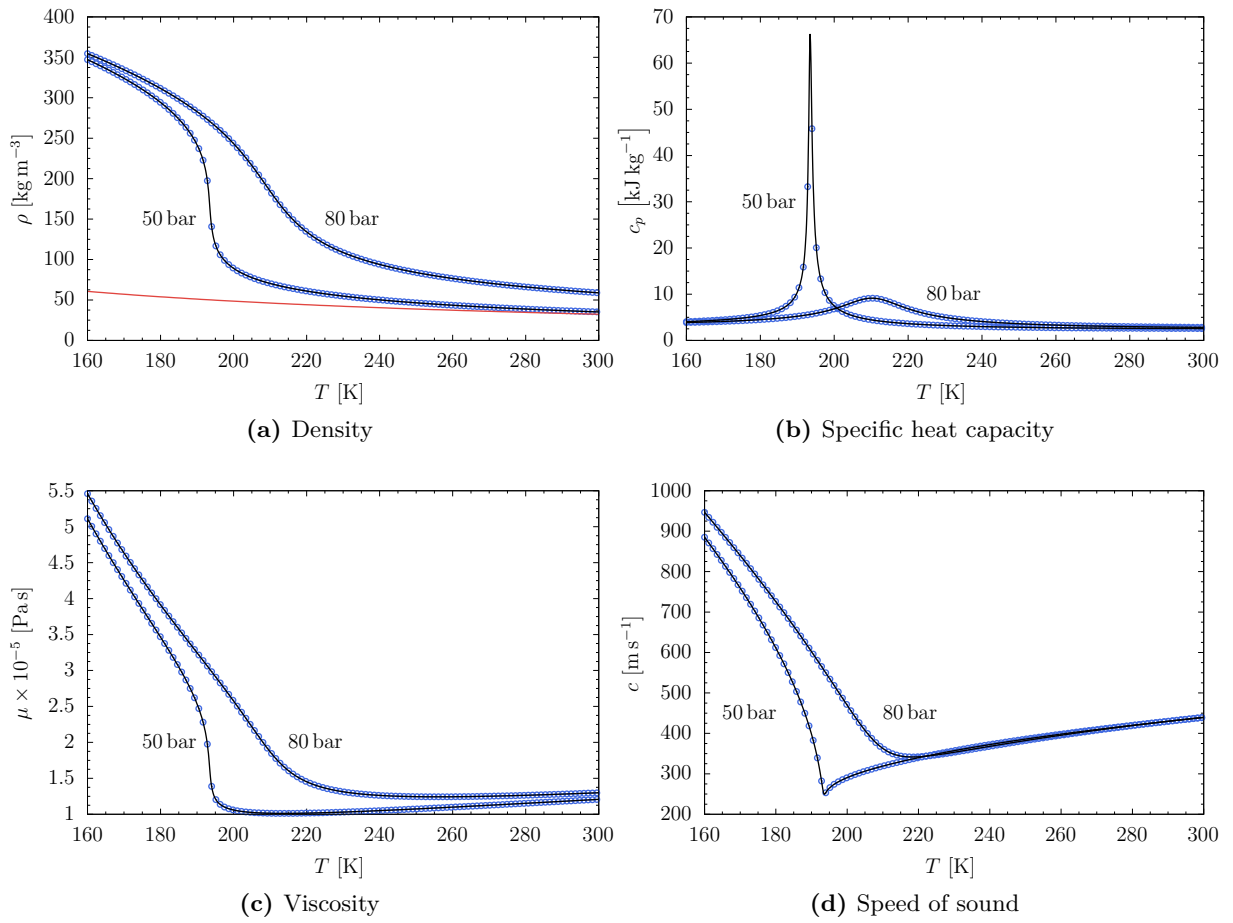


Figure 2.1.: Thermodynamic data of methane from the used look-up tables (\circ) compared to NIST data base (—) [9] for a pressure of 50 bar and 80 bar, respectively. The ideal gas law is included for the density (—).

3. NUMERICAL METHOD

The numerical methods introduced in this chapter are applied in the in-house code CATUM and are based on the preceding work at the Institute of Aerodynamics and Fluid Mechanics at the Technical University of Munich. For a detailed discussion we refer to Sezal [43], Schmidt [42] and Egerer [44]. In the following, we concisely introduce the employed numerical schemes for the flux calculation, the time integration and the implicit subgrid-scale model (SGS).

3.1. FINITE VOLUME METHOD

The flow solver CATUM is utilising the finite volume method (FVM). All performed simulations have been performed on body-fitted, block-structured, curvilinear grids with hexahedral cells. Rewriting the governing equations (Eq. (2.3)) in integral form and applying the Gauss' theorem results in

$$\partial_t \int_{\Omega} \boldsymbol{\Phi}(\mathbf{x}, t) d\mathcal{V} + \int_{\partial\Omega} \mathbf{F}(\boldsymbol{\Phi}, \mathbf{x}, t) d\mathcal{A} = \int_{\Omega} f(\mathbf{x}, t) d\mathcal{V}, \quad (3.1)$$

where f indicate body forces and the transported quantities are $\boldsymbol{\Phi} = [\rho, \rho\mathbf{u}, E]^T$. This equation is solved numerically by spatially discretizing the domain Ω with surface $\partial\Omega$ into N disjunct control volumes Ω_i , also referred to as grid cells. The volume-averaged quantity of a cell Ω_i with volume V_i is denoted with an overbar as

$$\bar{\boldsymbol{\Phi}}_i(t) = \frac{1}{V_i} \int_{\Omega_i} \boldsymbol{\Phi}_i(\mathbf{x}, t) d\mathcal{V}_i. \quad (3.2)$$

The surface integral in Eq. (3.1) for a hexahedral control volume can be numerically approximated by calculating the flux across all six cell faces ($j = 1, \dots, 6$) with area A_j and unit normal \mathbf{n}_j as

$$\int_{\partial\Omega_i} \mathbf{F}(\mathbf{U}, \mathbf{x}, t) d\mathcal{A} = \sum_{j=1}^6 (\check{\mathbf{F}}_j \mathbf{n}_j) A_j. \quad (3.3)$$

$\check{\mathbf{F}}$ denotes the numerical approximation of the physical flux \mathbf{F} . A semi-discretized form of Eq. (3.1) is obtained by combing Eq. (3.2) and Eq. (3.3)

$$\partial_t \bar{\boldsymbol{\Phi}}_i(t) \approx -\frac{1}{V_i} \sum_{j=1}^6 (\check{\mathbf{F}}_j \mathbf{n}_j) A_j + \check{f}_i. \quad (3.4)$$

3.2. TIME INTEGRATION

For all our LES we employ the explicit second-order, four-step low-storage Runge-Kutta method by Schmidt et al. [51]. Eq. (3.4) is rewritten as

$$\partial_t \bar{\boldsymbol{\Phi}}_i(t) = \mathcal{R}_i(\bar{\boldsymbol{\Phi}}_i), \quad (3.5)$$

3. NUMERICAL METHOD

where the right hand side is resumed to $\mathcal{R}(\bar{\Phi}_i)$. For the four-step Runge-Kutta time integration we split the time step Δt into four sub-steps r in order to move in time from t_n to t_{n+1} . The coefficients C_r for each sub-step are

- $C_1 = 0.11$
- $C_2 = 0.2766$
- $C_3 = 0.5$
- $C_4 = 1$

Thus, the time advancement for all quantities from $\bar{\Phi}_i^n$ to $\bar{\Phi}_i^{n+1}$ is written as

$$\bar{\Phi}_i^{n+1,r} = \bar{\Phi}_i^n + C_r \Delta t \mathcal{R}_i(\bar{\Phi}_i^{n+1,r-1}), \quad (3.6)$$

with $r = 1, \dots, 4$. The solution from the last time step is used for the first sub-step $\bar{\Phi}_i^{n+1,0} = \bar{\Phi}_i^n$. The time advancement is achieved after four steps $\bar{\Phi}_i^{n+1} = \bar{\Phi}_i^{n+1,4}$.

The global time step $\Delta t = t_{n+1} - t_n$ is limited by the Courant-Friedrichs-Lewy (CFL) number. First, a local time step Δt_i is calculated for each cell applying the CFL criterion

$$\Delta t_i = CFL \left(\frac{l_i/n_d}{|\bar{\mathbf{u}}_i| + \bar{c}_i} + \frac{(l_i/n_d)^2}{2(\bar{\nu}_i + \bar{\nu}_{t,i})} \right). \quad (3.7)$$

l_i represents a characteristic cell length, n_d the dimensions of the physical problem, $\bar{\mathbf{u}}_i$ the characteristic velocity, \bar{c}_i the speed of sound, $\bar{\nu}_i$ the dynamic viscosity and $\bar{\nu}_{t,i}$ the subgrid viscosity. The left term on the right hand side limits the time step due to convection and the second term due to diffusion, see Ferziger and Peric [52]. A CFL number of 1.4 is used for all LES, since the presented Runge-Kutta scheme has an enlarged stability region. The smallest local time step is used for the time advancement

$$\Delta t = \min(\Delta t_i). \quad (3.8)$$

3.3. NUMERICAL FLUX

CATUM employs a compact four-cell stencil in order to reconstruct the cell face values, which are needed to calculate the flux $\check{\mathbf{F}}$. A sketch of the four-cell stencil is presented in Fig. 3.1 indicating the involved cells with the subscript $i-1, i, i+1, i+2$. The numerical flux $\check{\mathbf{F}}$ consists of a convective $\check{\mathbf{C}}$, a pressure $\check{\mathbf{P}}$ and a viscous flux $\check{\mathbf{D}}$. The convective flux $\check{\mathbf{C}}_{i+\frac{1}{2}}$ on an equidistant Cartesian grid at cell face $i+\frac{1}{2}$ reads

$$\check{\mathbf{C}}_{i+\frac{1}{2}} = \check{u}_{i+\frac{1}{2}}^* \left[\begin{array}{c} \check{\rho} \\ \check{\rho}\check{\mathbf{u}} \\ \check{\rho}\check{e} + \frac{1}{2}\check{\rho}\check{\mathbf{u}}^2 + \check{p}^* \end{array} \right]_{i+\frac{1}{2}}, \quad (3.9)$$

and the pressure flux $\check{P}_{i+\frac{1}{2}}$ reads

$$\check{P}_{i+\frac{1}{2}} = \check{p}_{i+\frac{1}{2}}^* \begin{bmatrix} 0 \\ \mathbf{n} \\ 0 \end{bmatrix}, \quad (3.10)$$

where \check{u}^* is the numerical transport velocity and \check{p}^* the interface pressure.

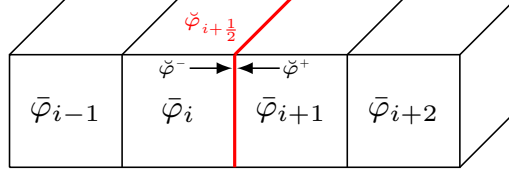


Figure 3.1.: Reconstruction of cell-face values $\check{\varphi}$ by means of cell average values using a compact four cell stencil in CATUM.

3.3.1. RECONSTRUCTION

In all LES the scheme by Egerer et al. [53] is used, which is based on the compact four-cell stencil mentioned above. The proposed scheme switches the reconstruction at the cell face between a linear fourth-order central scheme for high accuracy and a more stable upwind-biased scheme. The reconstruction of $\check{\varphi}_{i+\frac{1}{2}}$ follows

$$\check{\varphi}_{i+\frac{1}{2}} = (1 - f(\Psi)) \check{\varphi}_{i+\frac{1}{2}}^c + f(\Psi) \check{\varphi}_{i+\frac{1}{2}}^u, \quad (3.11)$$

where the superscript c denotes the central scheme and u the upwind-biased scheme. This also holds for the transport velocity and the interface pressure

$$\check{u}_{i+\frac{1}{2}}^* = (1 - f(\Psi)) \check{u}_{i+\frac{1}{2}}^{*,c} + f(\Psi) \check{u}_{i+\frac{1}{2}}^{*,u}, \quad (3.12)$$

$$\check{p}_{i+\frac{1}{2}}^* = (1 - f(\Psi)) \check{p}_{i+\frac{1}{2}}^c + f(\Psi) \check{p}_{i+\frac{1}{2}}^u. \quad (3.13)$$

A discontinuity detecting sensor functional is used to switch the reconstruction at the cell face. The vorticity-dilation based discontinuity-detector sensor proposed by Ducros et al. [54]

$$\Psi = \frac{|\nabla \cdot \mathbf{u}|}{|\nabla \cdot \mathbf{u}| + \|\nabla \times \mathbf{u}\| + \epsilon}, \quad (3.14)$$

with $\epsilon = 10^{-15}$, is employed. The sensor is switched on, if the threshold value of 0.95 is exceeded,

$$f(\Psi) = \begin{cases} 1 & , \quad \Psi \geq 0.95 \\ 0 & , \quad \Psi < 0.95. \end{cases} \quad (3.15)$$

In all LES the sensor is active on less than 0.002% of the total volume.

3.3.2. CENTRAL SCHEME

The proposed scheme by Egerer *et al.* [53] uses a high order reconstruction in smooth regions. If the sensor is not switched on $f(\Psi) = 0$, then a smooth region is present, where higher order reconstruction schemes can be applied. Hence, the velocities and the static pressure are reconstructed by a linear fourth-order central scheme

$$\check{\varphi}_{i+\frac{1}{2}}^c = \frac{1}{12}(7(\bar{\varphi}_i + \bar{\varphi}_{i+1}) - \bar{\varphi}_{i-1} - \bar{\varphi}_{i+2}), \quad (3.16)$$

whereas an arithmetic mean is employed for the density ρ and internal energy ρe

$$\check{\varphi}_{i+\frac{1}{2}}^c = \frac{1}{2}(\check{\varphi}_{i+\frac{1}{2}}^+ + \check{\varphi}_{i+\frac{1}{2}}^-). \quad (3.17)$$

The numerical transport velocity $\check{u}_{i+\frac{1}{2}}^{*,c}$ reads

$$\check{u}_{i+\frac{1}{2}}^{*,c} = \check{u}_{i+\frac{1}{2}}^c + \frac{\overline{\Delta^3 p}_{i+\frac{1}{2}}}{I^- + I^+}, \quad (3.18)$$

with the acoustic impedances I^\pm

$$I^- = \frac{1}{4}(3\bar{\rho}_i + \bar{\rho}_{i+1})\bar{c}_{max}, \quad (3.19)$$

$$I^+ = \frac{1}{4}(\bar{\rho}_i + 3\bar{\rho}_{i+1})\bar{c}_{max}. \quad (3.20)$$

\bar{c}_{max} is the maximum speed of sound within the numerical four cell stencil and $\overline{\Delta^3 p}$ represents an approximation of the third pressure derivative based on Hickel *et al.* [55]. The superscripts $+/-$ refer to the side of the reconstruction and is introduced in the next subsection.

3.3.3. UPWIND-BIASED SCHEME

Since high gradients may be present in transcritical flows, a more robust scheme is required. If discontinuities are detected by the sensor functional Ψ , then an upwind-biased reconstruction is applied for more stability. We use the scheme proposed by Schmidt [42], since it was specially designed for compressible flows with steep gradients, as they can be found in transcritical flows. In order to obtain the cell face values $\check{\varphi}_{i+\frac{1}{2}}^u$, we evaluate $\check{\varphi}_{i+\frac{1}{2}}$ from the left side $\check{\varphi}_{i+\frac{1}{2}}^-$ and the right side $\check{\varphi}_{i+\frac{1}{2}}^+$, see $-/+$ in Fig. 3.1.

$$\begin{aligned} \check{\varphi}_{i+\frac{1}{2}}^- &= \bar{\varphi}_i + \frac{1}{2}L(r_{i+\frac{1}{2}}^-)(\bar{\varphi}_i - \bar{\varphi}_{i-1}), \\ \check{\varphi}_{i+\frac{1}{2}}^+ &= \bar{\varphi}_{i+1} + \frac{1}{2}L(r_{i+\frac{1}{2}}^+)(\bar{\varphi}_{i+2} - \bar{\varphi}_{i+1}), \end{aligned} \quad (3.21)$$

where L is a slope limiter function based on the ratio between upwind and central differencing

$$\begin{aligned} r_{i+\frac{1}{2}}^- &= \frac{\bar{\varphi}_i - \bar{\varphi}_{i-1}}{\bar{\varphi}_{i+1} - \bar{\varphi}_i}, \\ r_{i+\frac{1}{2}}^+ &= \frac{\bar{\varphi}_{i+1} - \bar{\varphi}_i}{\bar{\varphi}_{i+2} - \bar{\varphi}_{i+1}}. \end{aligned} \quad (3.22)$$

The slope limiter by Koren [56] is used for the velocity components

$$L(r) = \max \left[0, \min \left(2r, \frac{1+2r}{3}, 2 \right) \right], \quad (3.23)$$

which is third-order accurate for sufficiently smooth data. The Minmod slope limiter by Roe [57] is employed for the density and energy

$$L(r) = \max(0, \min(1, r)), \quad (3.24)$$

which is second-order accurate in smooth regions.

The upwind reconstruction value is chosen based on the sign of the transport velocity $\check{u}^{*,u}$

$$\check{\varphi}_{i+\frac{1}{2}}^u = \begin{cases} \check{\varphi}_{i+\frac{1}{2}}^- & \text{for } \check{u}_{i+\frac{1}{2}}^{*,u} \geq 0 \\ \check{\varphi}_{i+\frac{1}{2}}^+ & \text{for } \check{u}_{i+\frac{1}{2}}^{*,u} < 0. \end{cases} \quad (3.25)$$

The numerical transport velocity $\check{u}_{i+\frac{1}{2}}^{*,u}$ is calculated as

$$\check{u}_{i+\frac{1}{2}}^{*,u} = \frac{I^- \check{u}_{i+\frac{1}{2}}^- + I^+ \check{u}_{i+\frac{1}{2}}^+ + \check{p}_{i+\frac{1}{2}}^- - \check{p}_{i+\frac{1}{2}}^+}{I^- + I^+}, \quad (3.26)$$

and interface pressure $\check{p}_{i+\frac{1}{2}}^u$ as

$$\check{p}_{i+\frac{1}{2}}^u = \frac{\check{p}_{i+\frac{1}{2}}^- + \check{p}_{i+\frac{1}{2}}^+}{2}. \quad (3.27)$$

The missing viscous flux $\check{D}_{i+\frac{1}{2}}$ is discretized using a linear second-order central scheme.

3.3.4. SUB-GRID SCALE MODELLING

The unresolved scales (SGS) within the performed LES are modelled implicitly based on the Adaptive Local Deconvolution Method (ALDM) [58, 59, 55]. This method provides a physically consistent subgrid-scale turbulence model by adjusting the truncation error of the convective flux calculation. The approach is based on a modified Lax-Friedrichs flux function, which consists of the physical flux and a dissipative regularisation term operating on the error of the cell face reconstruction. Based on the compressible ALDM scheme by Hickel *et al.* [55], Egerer *et al.* [53] developed a regularization term corresponding to the hybrid flux calculation of CATUM. The regularization term \check{R} is added to the convective flux

$$\check{C}^{ALDM} = \check{C} - \check{R} = \check{u}^* \begin{bmatrix} \check{\rho} \\ \check{\rho}\check{u} \\ \check{\rho}e + \frac{1}{2}\check{\rho}\check{u}^2 + \check{p}^* \end{bmatrix} - \begin{bmatrix} \check{R}^\rho \\ \check{R}^{\rho u} \\ \check{R}^{\rho e} \end{bmatrix}. \quad (3.28)$$

The definition for each element of the regularization term can be found in Egerer *et al.* [53].

An additional wall-damping is used, since the SGS dissipation is overestimated close to the walls. This wall-damping γ^{VD} is of van Driest Type [60] and is included within the regularization term \check{R} , based on Hickel and Adams [61]

$$\gamma^{VD} = \left[1 - \exp \left(- \left(\frac{y^+}{A^+} \right)^n \right) \right]^m. \quad (3.29)$$

3. NUMERICAL METHOD

The parameters are $A^+ = 50$, $n = 3$ and $m = 1/3$. $y^+ = y/l^+ = y * \rho * u_\tau / \mu$ is the dimensionless wall distance with the viscous length scale l^+ and the friction velocity u_τ . The wall damping is only active for $y^+ < 80$.

4. ACCOMPLISHMENTS

This chapter summarizes the main contributions of this thesis based on the three first-author peer-reviewed publications, which are included in Appendix A.

4.1. ASSESSMENT OF RANS

Publication:

T. KALLER*, A. DOEHRING*, S. HICKEL, S. J. SCHMIDT AND N. A. ADAMS (2021)
Assessment of RANS turbulence models for straight cooling ducts: secondary flow and strong property variation effects.

In N. A. Adams, W. Schröder, R. Radespiel, O. Haidn, T. Sattelmayer, C. Stemmer, B. Weigand (eds) Future Space-Transport-System Components under High Thermal and Mechanical Loads: Results from the DFG Collaborative Research Center TRR40, Notes on Numerical Fluid Mechanics and Multidisciplinary Design, vol 146, Springer, Cham. doi:10.1007/978-3-030-53847-7_20.

4.1.1. SUMMARY OF THE PUBLICATION

Several studies [18, 17, 16] reported the difficulties of RANS in prediction transcritical turbulent flows. In this book chapter [40] well-resolved LES are compared with RANS simulations, in order to confirm the above statement for methane at transcritical conditions. The comparison between LES and RANS is performed using the same channel extensions, grid, mass flow, boundary conditions and look-up table based thermodynamic modelling for both simulation methodologies. Pseudo-boiling is enclosed within the channel located in the vicinity of the cold wall. The position was controlled by the chosen wall temperatures. The bulk pressure of 50 bar results in a reduced pressure of $p_r = 1.09$ introducing strong property variations at the pseudo-boiling position.

RANS simulations are performed with ANSYS FLUENT using the *Baseline Reynolds stress model* (BSL RSM), which is suited for complex flows and without isotropic eddy viscosity. The turbulent heat transfer is modelled both with a constant turbulent Prandtl number of 0.85 and the algebraic formulation by Kays and Crawford [62]. A converged solution is obtained with residuals below 10^{-6} for the continuity, momentum, total energy and RSM transport equations.

Well-resolved LES are conducted with the in-house code CATUM employing the Adaptive Local Deconvolution Method (ALDM) [58, 59, 55] for physically consistent subgrid scale turbulence modelling. The high speed of sound (see Fig. 1.3d) and the CFL number criterion lead to very

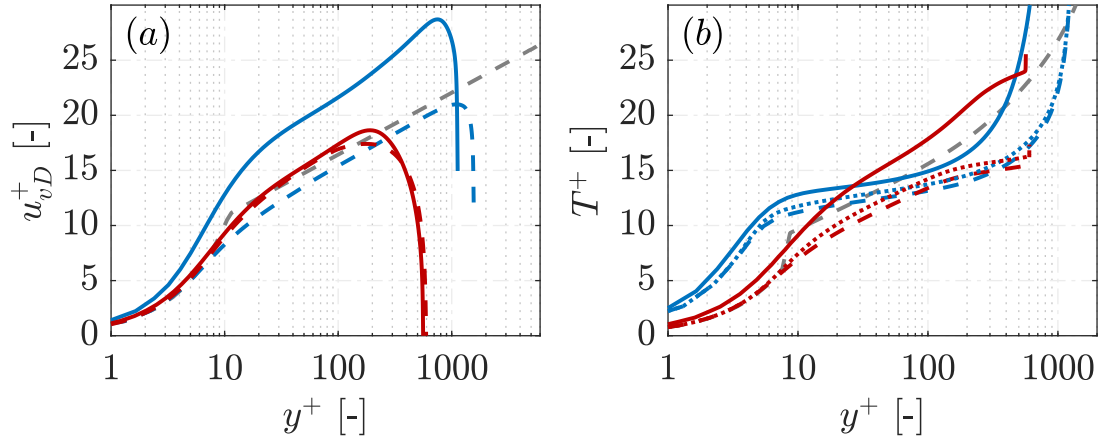


Figure 4.1.: Mean flow properties over wall units. (a) van Driest transformed velocity and (b) transformed temperature. Blue lines indicate the cold and red lines the hot wall. The analytical law of the wall with $\kappa = 0.41$ and $B = 5.2$, and the empirical function of Kader are plotted as (-----). LES (—), BSL RSM with $Pr_t = 0.85$ (---) and BSL RSM with Kays and Crawford model (.....). This figure is taken from Kaller et al. [40] under the terms of the Creative Commons CC BY.

small time steps of the order of 10^{-10} s. Hence, high computational costs arise to obtain a statistically converged solution. This holds for all LES, which are performed within this thesis.

The results of both methodologies are compared focusing on the mean velocity profiles based on the van Driest transformation [28] and the mean temperature profiles based on Kader [63], see Fig. 4.1. The profiles show a large discrepancy between RANS and LES at the cold wall, where pseudo-boiling is dominant. The more advanced turbulent heat flux closure by Kays and Crawford [62] leads only to minor improvements in the temperature distribution. Integral values such as the wall shear stress and wall heat flux are overestimated in RANS. Especially the wall shear stress at the cold wall is twice as high in RANS implying missing transcritical features, which are not covered by the RANS models.

4.1.2. INDIVIDUAL CONTRIBUTION

I developed the simulation setup and performed the numerical simulations with the in-house code CATUM and ANSYS FLUENT. The already existing look-up table generation tool was optimised and customized for transcritical channel flows using methane. The generated look-up tables have been coupled with ANSYS FLUENT as part of a student thesis, which was supervised by me. For this purpose user-defined functions (UDF) have been employed within FLUENT. I further optimized the coupling between the look-up tables and the RANS flow solver for a better performance. I also extended the post-processing and analysed the simulation data. This book chapter has two first authors. My former colleague Thomas Kaller wrote the part about the high aspect ratio cooling duct and I wrote the part about transcritical channel flows.

4.2. TURBULENT PRANDTL NUMBER

Publication:

A. DOEHRING, T. KALLER, S.J. SCHMIDT, N.A. ADAMS (2021)
Large-eddy simulation of turbulent channel flow at transcritical states
International Journal of Heat and Fluid Flow, 89, 108781.

4.2.1. SUMMARY OF THE PUBLICATION

One important parameter, controlling the prediction capability of the RANS or WMLES is the turbulence modelling, in particular the closure for the momentum and energy equation. Here, we use the equilibrium turbulent boundary layer equations, which are used in wall-stress WMLES [64] as an example:

$$\begin{aligned} \frac{\partial}{\partial y} \left[(\mu + \boldsymbol{\mu}_t) \frac{\partial \tilde{u}}{\partial y} \right] &= 0, \\ \frac{\partial}{\partial y} \left[(\mu + \boldsymbol{\mu}_t) \tilde{u} \frac{\partial \tilde{u}}{\partial y} + c_p \left(\frac{\mu}{Pr} + \frac{\boldsymbol{\mu}_t}{Pr_t} \frac{\partial \tilde{T}}{\partial y} \right) \right] &= 0. \end{aligned}$$

The bold quantities are the eddy viscosity $\boldsymbol{\mu}_t$ and the turbulent Prandtl number Pr_t , which have to be modelled in order to close the system of ordinary differential equations (ODE). Since turbulence models are developed using canonical flows at ideal conditions, they might contribute to the bad prediction capabilities in flows with strong non-linear property variations.

We performed two well-resolved LES of a transcritical channel flow in order to analyse the mentioned modelling parameters. For both simulations we used again methane at a reduced pressure of $p_r = 1.03$ and $p_r = 1.24$ in order to alter the intensity of the pseudo-boiling. Pseudo-boiling is located in the buffer layer at $y^+ \approx 14$ and $y^+ \approx 23$ very close to the cold wall. Both LES are performed with the in-house code CATUM employing the Adaptive Local Deconvolution Method (ALDM) [58, 59, 55] for physically consistent subgrid scale turbulence modelling.

Especially in industrial applications, Pr_t is set to a constant value, which is based upon the strong Reynolds analogy (SRA), assuming a correlation between the turbulent heat transfer and the turbulent momentum transfer. Experimental and numerical studies have shown, that this simple assumption does not hold, since there is at least a dependence on the wall distance and the molecular Prandtl number $f(y^+, Pr)$ [62]. For the analysis of the turbulent Prandtl number in transcritical flows we employed three different definitions:

1. $Pr_t = \frac{\overline{u'v'}}{\overline{v''T'}} \frac{\partial \tilde{T}/\partial y}{\partial \tilde{u}/\partial y}$: Based on Reynolds average and mean temperature
2. $Pr_t = \frac{\overline{u''v''}}{\overline{v''T''}} \frac{\partial \tilde{T}/\partial y}{\partial \tilde{u}/\partial y}$: Based on Favre average and mean temperature
3. $Pr_t = \frac{\overline{u''v''}}{\overline{v''h''}} \frac{\partial \tilde{h}/\partial y}{\partial \tilde{u}/\partial y}$: Based on Favre average and mean enthalpy

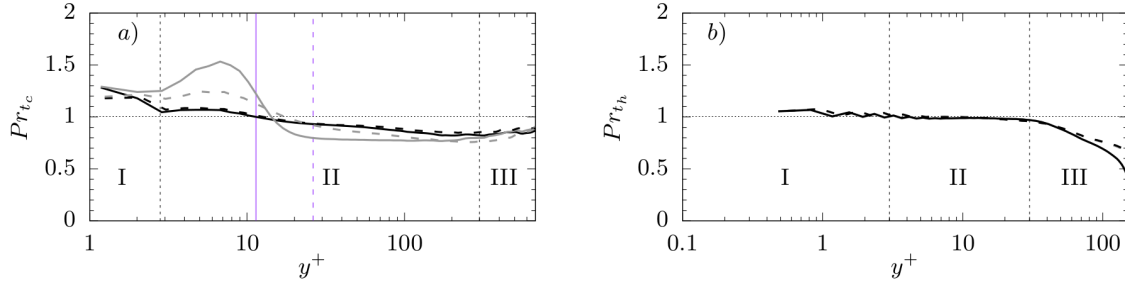


Figure 4.2.: Turbulent Prandtl number at the cold wall (a) and the hot wall (b) over wall units y^+ for $p_r = 1.03$ (—) and $p_r = 1.24$ (- - -). Included are the second (grey) and third (black) definition for Pr_t . The pseudo boiling position at the cold wall is indicated by a vertical purple line. This figure is taken from Doehring et al. [41] under the terms of the Creative Commons CC BY.

The first two definitions are taken from literature, where the turbulent Prandtl number is based on calorically perfect gas. But, using the total energy equation 2.3 and the fact, that $h \neq c_p T$ in the vicinity of the pseudo-boiling, results in the third definition based on enthalpy.

In Fig. 4.2 the turbulent Prandtl number profiles for both simulations and both walls are presented. At the hot wall the fluid features an ideal gas behaviour and the relation $h = c_p T$ holds. Consequently, no difference between the second and third formulation is observed and the turbulent Prandtl number is relatively constant in region II. Using the enthalpy based formulation at the cold wall has the following aspects:

1. Absent of s-shape profile, which is observable using the second Pr_t definition.
2. Slight increase towards the wall as it is found for ideal gas properties at the hot wall.
3. Pr_t profiles for both bulk pressure values are on top of each other. This property is of great importance in order to model Pr_t for different transcritical flow conditions.

Based on these aspects, it is recommended to use the enthalpy based formulation of the turbulent Prandtl number in transcritical flows.

Further insights obtained in this manuscript:

- Splitting the turbulent shear stress and the turbulent heat flux into three parts based on

$$\widetilde{u''v''} = \overline{u'v'} - \overline{u''} \overline{v''} + \frac{\overline{\rho' u' v'}}{\overline{\rho}},$$

$$\widetilde{v''h''} = \overline{v'h'} - \overline{v''} \overline{h''} + \frac{\overline{\rho' v' h'}}{\overline{\rho}}.$$

The tilde represents a Favre average, the overline a Reynolds average, and $''$ and $'$ the corresponding fluctuations. The results show, that the first term is the most dominant one and the other two are one order of magnitude smaller. The third term has to be taken into account if strong property variations are present.

- The turbulent eddy viscosity can be modelled using the mixing length ansatz, where the size of the eddies scales with the distance to the wall. Another possibility to obtain a mixing length is to use a stress balance as it is done by Pirozzoli [65]. The comparison of both methods showed, that only at the hot wall the mixing length based on the stress balance was reproduced. At the cold wall both methods fail to describe the mixing length in transcritical flows. This implies, that Prandtl's mixing length ansatz does not hold in transcritical flows and the formulations based on the stress balance is incomplete.
- A modified version of the proposed correlation for the turbulent Prandtl number by Bae [66] is in good agreement with the obtained Pr_t profiles.

4.2.2. INDIVIDUAL CONTRIBUTION

I developed the simulation setup and performed the numerical simulations with the in-house code CATUM. I also extended the post-processing and analysed the simulation data. Obtained data was partly compared to existing correlations and model formulations. This manuscript was written by me.

4.3. MOMENTUM BOUNDARY LAYERS IN TRANSCRITICAL CHANNEL FLOWS

Publication:

A. DOEHRING, S.J. SCHMIDT, N.A. ADAMS (2021)

Momentum boundary layers in transcritical channel flows

International Journal of Heat and Fluid Flow, 103, 109201.

4.3.1. SUMMARY OF THE PUBLICATION

In the previous paper [41] the stress balance formulation for the mixing length was not successful in the vicinity of the pseudo-boiling. From this, we imply that the stress balance formulation was not complete in transcritical flows. In this regard, Kawai *et al.* [27] reported an induced turbulent mass flux in the boundary layer due to density fluctuations. This leads to our comprehensive investigation of the turbulent momentum boundary layer in transcritical flows using methane comprised of

- mean flow properties,
- law of the wall for the velocity,
- Reynolds stresses distribution,
- turbulent mass flux,
- turbulent kinetic energy budgets,
- quadrant and octant analysis of the Reynolds shear stresses,
- invariant map to visualize the anisotropy distribution.

For this extensive analysis we performed seven well-resolved LES of transcritical channel flow, where three parameters have been varied. The first parameter is the Reynolds number Re with a value of 10000 and 20000 in order to identify any Reynolds number dependency. Secondly, the pseudo-boiling position has been varied between the cold wall, hot wall and channel centre. The last parameter is the bulk pressure, which controls the pseudo-boiling intensity. Also for this study, we used the in-house code CATUM employing the Adaptive Local Deconvolution Method (ALDM) [58, 59, 55] for physically consistent subgrid scale turbulence modelling. Compared to the previous study, we extended the domain in the stream- and spanwise directions in order to ensure a decorrelated flow, motivated by the identified larger streamwise structures in the DNS study by Kim *et al.* [31]. The grid was increased to 256 cells in each direction corresponding to $\Delta x^+ < 42.52$, $\Delta z^+ < 14.17$, $\Delta y_{\min}^+ < 0.71$, $\Delta y_{\max}^+ < 15.44$, $\Delta y_{\text{thermal, min}}^+ < 0.96$ and $\Delta y_{\text{thermal, max}}^+ < 20.86$ for all seven simulations. The resolution with respect to wall units $\Delta x^+ = \Delta x \rho_w u_\tau / \mu_w$ is based on the friction velocity $u_\tau^2 = (\tau_w / \rho_w)$ and the wall shear stress $\tau_w = (\mu \partial u / \partial y)|_w$. Thus, the viscous and the thermal scales are resolved in all simulations.

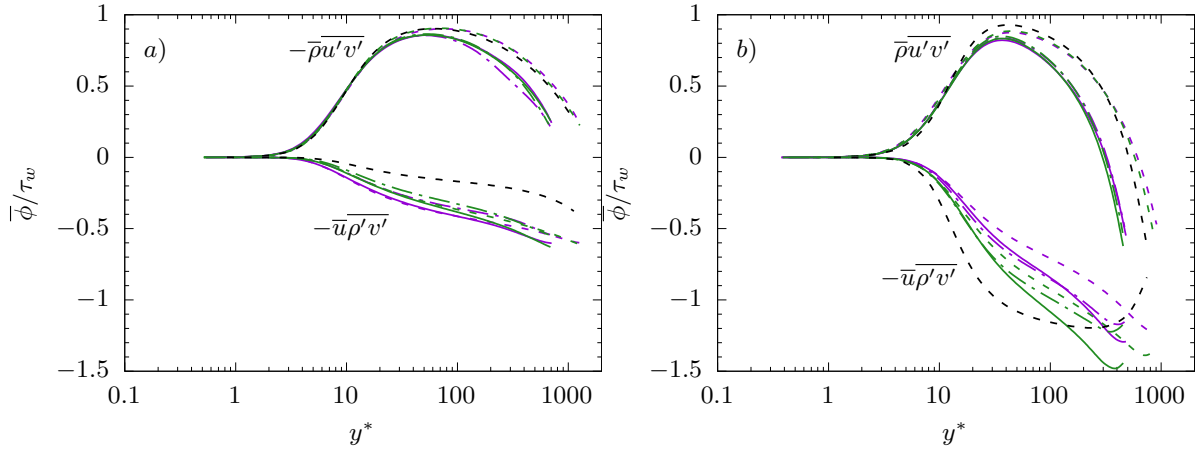


Figure 4.3.: Unclosed terms obtained by applying the Reynolds averaging to the streamwise momentum equation. The left column refers to the cold and the right column to the hot wall. The Reynolds shear stress and the mass flux in wall normal direction are shown. Cases: TCF55B (—), TCF65B (- - -), TCF55BR (- - -), TCF55M (—), TCF65M (- - -), TCF55MR (- - -), TCF60TR (- - -). This figure is taken from Doehring et al. [15] and reprinted with permission of Elsevier.

One difficulty with transcritical channel flows, which has not been mentioned is the realisation of a grid convergence study. Each simulation starts at a laminar state with a starting bulk pressure. During the laminar-turbulent transition the pressure drops to an unknown bulk pressure due to the non-linear thermodynamics. Additionally, a refinement of the grid leads to an adjustment of the wall shear stress and wall heat flux, thus, to a bulk pressure, which varies from one level to another. As a consequence, the starting bulk pressure has been adjusted by trial and error due to the non-linearity of the thermodynamics in order to match the final bulk pressure at all grid levels. As a result, every grid level is a slightly different case with a different bulk pressure, bulk temperature and bulk heat capacity distribution due to the non-linear thermodynamics.

After performing an averaging of the streamwise momentum equation four unclosed terms are identified. The turbulent mass flux is one of the unclosed terms, shown in Fig. 4.3. At both walls and for all seven cases it can be observed, that the turbulent mass flux is of the same order of magnitude as the turbulent shear stress. Although, Kawai et al. [27] observed a turbulent mass flux using parahydrogen, the magnitude was not as high as in this study using methane. Consequently, this unclosed term has to be included in RANS or WMLES modelling, which is already proposed by Kawai and Oikawa [67].

For this study, the statistics have not been calculated during the simulation, but approximately 20000 3D snapshots have been saved for each case, respectively. The presented statistical quantities are calculated after the simulations have been concluded. This requires a high amount of disk space, however, further analysis can be performed and the data can be used to develop low cost CFD models, like RANS and WMLES.

4.3.2. INDIVIDUAL CONTRIBUTION

I developed the simulation setup and performed the numerical simulations with the in-house code CATUM. I wrote a new MPI parallelized post-processing script based on python to analyse the simulation data. Obtained data was partly compared to existing correlations and model formulations. This manuscript was written by me.

5. CONCLUDING REMARKS

The concluding remarks comprise a summary of the thesis results and an outlook for future directions.

5.1. SUMMARY

Wall-bounded flows with trans- or supercritical fluids are found in many technical applications, as for instance supercritical water-cooled reactors, diesel engines, gas turbines and liquid-propellant rocket engines. A lot of effort has been made over the last decades to understand transcritical flows with its unique fluid properties using numerical studies. But still, there is a lack of understanding of the influence of strong property variations on the turbulent flow and the heat transfer. Furthermore, many studies are based on DNS simulations, which are limited by the Reynolds number.

The main focus of the present thesis was to analyse the influence of strong property variations on wall-bounded turbulent flows with heat transfer. For this analysis we employed our in-house code CATUM to perform well resolved LES. Using LES for our investigations allowed us to run the simulations at higher Reynolds numbers than most of the recent studies. Methane was used for all simulations, since it is an emerging fuel in LRE. Furthermore, to the best of the author's knowledge no high-fidelity numerical studies exist with transcritical methane. An adaptive look-up table method was used for a correct representation of methane's thermodynamic and transport properties. The used look-up tables are more accurate than common cubic equations of state, as for instance the Peng-Robinson equation of state. Adaptive Local Deconvolution Method (ALDM) has been used for a physically consistent subgrid-scale turbulence modelling.

The first study compares the results of a transcritical channel flow between RANS and well-resolved LES, in order to confirm the reported deficiencies of RANS in transcritical flows. The mean velocity and temperature profiles showed a large discrepancy between RANS and LES, especially at the cold wall, where pseudo-boiling was dominant. Including an advanced turbulent heat flux closure instead of a constant turbulent Prandtl number led only to minor improvements in the temperature distribution. The integral values such as the wall shear stress and heat flux at the walls are overestimated in RANS, in particular where fluid properties drastically change.

The second study stems from the reported influence of classical turbulence models on the prediction capabilities of RANS. For this purpose, two well-resolved LES have been performed to analyse the turbulent heat and momentum transfer in transcritical channel flows using methane. The reduced pressure was altered among the LES in order to alter the intensity of the pseudo-boiling. The chosen wall temperatures lead to pseudo-boiling in the buffer layer very close to the cold wall. For the analysis of the turbulent heat transfer in terms of the turbulent Prandtl number in transcritical flows we considered three different definitions. The proposed definition using

enthalpy was marginally affected by pseudo-boiling, thus, it is suited for turbulence modelling in context of transcritical flows. The mixing length in transcritical flows has been analysed by means of Prandtl's mixing length hypothesis as well as using a stress balance. Neither of the definitions were in agreement with the obtained mixing length at the cold wall. But, the stress balance formulation was capable to capture the mixing length at the hot wall, where an ideal gas behaviour is present. Thus, it can be concluded that Prandtl's mixing length ansatz does not work in transcritical flows and the formulation based on the stress balance is incomplete.

The third study originate from the insufficient stress balance formulation for the mixing length in transcritical flows. Seven well-resolved LES were conducted for a comprehensive investigation of the turbulent momentum boundary layer in transcritical flows. This study covered two Reynolds numbers, two bulk pressure values and three different pseudo-boiling positions. The statistical analysis is comprised of mean flow properties, law of the wall for the velocity, Reynolds stresses distribution, turbulent mass flux, turbulent kinetic energy budgets, quadrant and octant analysis of the Reynolds shear stresses and an invariant map to visualize the anisotropy distribution. One major observation was the induced turbulent mass flux, which was at the same order of magnitude as the turbulent shear stress in all seven LES.

The numerical investigation presented in this thesis provides a comprehensive analysis of transcritical channel flows using methane and contribute to a better understanding of transcritical wall-bounded flows. Different parameters, such as Reynolds number, pseudo-boiling intensity and location were covered within the presented investigations. The observed interaction between strong property variations and a turbulent flow with heat transfer provides a starting point for the development of future low-cost models in RANS or WMLES. This is further supported by the 3D data obtained in the last study.

5.2. OUTLOOK

The last study in this thesis was focusing on the momentum boundary layer. Guo *et al.* [34] investigated thermal boundary layers in transcritical flow using DNS and nitrogen. Their findings and proposed scaling laws for the temperature profiles can be compared and applied to the performed transcritical channel flows using wall-resolved LES in order to confirm their generality.

The performed well-resolved simulations require an increased spatial resolution in order to capture the non-linear thermodynamic behaviour of the fluid within the channel flow. Additionally, a very small time step arises due to the high speed of sound and the CFL criterion for compressible fluid solvers. As a consequence, the computation effort is increased. This is reinforced by the fact, that realistic cooling channel flows are at much higher Reynolds numbers. A possibility to perform numerical studies of transcritical channel flows at realistic conditions and to attenuate the numerical cost is the use of wall models. In WMLES the viscous sublayer and the logarithmic layer are modelled, which allows to increase the spatial resolution and the time step size. The well-resolved LES presented within this thesis have been performed with the objective to support the development of future wall models by providing a basis with the obtained insights and data. Recent approaches for wall modelled LES, which have to be extended for transcritical flows, are summarized in the following.

- A turbulence enrichment model for subfilter-scale motions in large eddy simulations using Fourier–Gabor modes has been proposed by Ghate and Lele [68, 69].
- A total stress balance formulation has recently been proposed by Griffin et al. [36] and Bai et al. [37] for compressible boundary layers. In the next step, the total stress formulation has been applied within a wall model for compressible boundary layers by Griffin et al. [70]. The proposed transformations can be used as a starting point for a total stress formulation in context of flows with strong property variations. Thus, based on an advanced total stress formulation existing wall models can be improved for the application in transcritical flows.
- Hansen et al. [71] augmented a wall model using a one-dimensional proper orthogonal decomposition.

The channel flow geometry used in this thesis has to be extended to a duct with a rectangular cross section in order to represent a realistic cooling channel in LRE. The extension to four walls leads to turbulence induced secondary flow. The interaction between the secondary flow and heat transfer has been investigated by Kaller et al. [72]. Their analysis can be applied to a transcritical duct flows in order to determine the sensitivity of the turbulence induced vortices to strong property variations.

A. SELECTED PUBLICATIONS

Here, the main publications are attached.

A.1. ASSESSMENT OF RANS TURBULENCE MODELS FOR STRAIGHT COOLING DUCTS: SECONDARY FLOW AND STRONG PROPERTY VARIATION EFFECTS

A.1.1. RIGHTS AND PERMISSIONS:

This chapter is licensed under the terms of the Creative Commons Attribution 4.0 International License (<http://creativecommons.org/licenses/by/4.0/>), which permits use, sharing, adaptation, distribution and reproduction in any medium or format, as long as you give appropriate credit to the original author(s) and the source, provide a link to the Creative Commons license and indicate if changes were made.

The images or other third party material in this chapter are included in the chapter's Creative Commons license, unless indicated otherwise in a credit line to the material. If material is not included in the chapter's Creative Commons license and your intended use is not permitted by statutory regulation or exceeds the permitted use, you will need to obtain permission directly from the copyright holder.

A.1.2. MANUSCRIPT

Assessment of RANS Turbulence Models for Straight Cooling Ducts: Secondary Flow and Strong Property Variation Effects



Thomas Kaller, Alexander Doehring, Stefan Hickel, Steffen J. Schmidt, and Nikolaus A. Adams

Abstract We present well-resolved RANS simulations of two generic asymmetrically heated cooling channel configurations, a high aspect ratio cooling duct operated with liquid water at $Re_b = 110 \times 10^3$ and a cryogenic transcritical channel operated with methane at $Re_b = 16 \times 10^3$. The former setup serves to investigate the interaction of turbulence-induced secondary flow and heat transfer, and the latter to investigate the influence of strong non-linear thermodynamic property variations in the vicinity of the critical point on the flow field and heat transfer. To assess the accuracy of the RANS simulations for both setups, well-resolved implicit LES simulations using the adaptive local deconvolution method as subgrid-scale turbulence model serve as comparison databases. The investigation focuses on the prediction capabilities of RANS turbulence models for the flow as well as the temperature field and turbulent heat transfer with a special focus on the turbulent heat flux closure influence.

1 Introduction

Understanding cooling duct flows is essential for efficient structural cooling in many technical applications. Examples range from ventilation systems, electrical component cooling to launcher propulsion systems. The latter use the cryogenic propellant as coolant at a supercritical state.

T. Kaller (✉) · A. Doehring (✉) · S. J. Schmidt · N. A. Adams
Chair of Aerodynamics and Fluid Mechanics, Department of Mechanical Engineering,
Technical University of Munich, Boltzmannstr. 15, D-85748 Garching bei München, Germany
e-mail: thomas.kaller@tum.de

A. Doehring
e-mail: alex.doehring@tum.de

S. Hickel
Faculty of Aerospace Engineering, Technische Universiteit Delft, Kluyverweg 1,
2629 HT Delft, The Netherlands

The turbulent flow and heat transfer within a cooling duct is highly affected by the presence of secondary flows and strong non-linear thermodynamic property variations in the vicinity of the pseudo-boiling line (PBL) [5]. Secondary flows enhance the mixing of hot and cold fluid and increase thus the overall cooling efficiency. Within the current study we focus on the relatively weak turbulence-induced secondary flow. Strong non-linear property variations are induced by intermolecular repulsive forces and significantly affect the heat transfer and shear forces. As a consequence, effects like the heat transfer enhancement as well as the onset of heat transfer deterioration in transcritical flows are difficult to correctly predict.

Three major turbulence simulation classes exist: direct numerical simulations (DNS), large-eddy simulations (LES) and Reynolds-averaged Navier-Stokes simulations (RANS). In DNS all spatial and temporal scales are fully resolved. In LES, large turbulent structures are resolved, whereas small scales or subgrid-scales (SGS) are modelled. Using RANS, the Navier-Stokes equations (NSE) are solved approximately for the averaged state and all scales are modelled. To close the equation system approximations for Reynolds stresses $\overline{u'_i u'_j}$ and turbulent heat fluxes $\overline{u'_i h'}$ have to be derived. Reynolds stress models (RSM) introduce partial differential equations (PDE) for the individual turbulent stress components offering the advantage over less complex models, like the $k - \varepsilon$ or SST models, to account for turbulence anisotropy. To approximate the unknown turbulent heat fluxes the most prevalent method is using a gradient transport approach with a constant Pr_t . To account for the anisotropy of $\overline{u'_i h'}$ additional PDEs can be introduced for the individual components or a less expensive algebraic approximation based on the Reynolds stress tensor utilised.

Relevant DNS studies of turbulence-induced secondary flow in square ducts include [11, 25], and in high aspect ratio ducts [31], the AR ranging from 1 – 7. The interaction of heating and turbulence-induced secondary flow has been analysed by [29] for square ducts and by [6] for rectangular ducts at small aspect ratios, both performed LES. DNS of a transcritical channel flow has been performed by Ma et al. [24] using an entropy-stable double-flux model in order to avoid spurious pressure oscillations. They have observed a logarithmic scaling of the second-order structure function and a k^{-1} scaling of the streamwise energy spectra, which supports the attached-eddy hypothesis in transcritical flows. A heated transcritical turbulent boundary layer over a flat plate has been investigated by Kawai [20] with DNS. His study shows large density fluctuations, which exceed Morkovin's hypothesis and lead to a non-negligible turbulent mass flux. RANS studies for cooling duct flows under realistic rocket engine conditions have been presented by [26, 27].

In the first part of the present study an asymmetrically heated high aspect ratio cooling duct (HARCD) at $Re_b = 110 \cdot 10^3$ and a moderate heating of $T_w - T_b = 40$ K is investigated using the BSL RSM and various turbulent heat flux closure models with ANSYS CFX. This setup has been studied experimentally, [28], and using a LES, [16–19] serving as comparison database. In the second part a cryogenic transcritical channel at $Re_b = 16 \cdot 10^3$ is investigated with the BSL RSM and various turbulent heat flux closure models with ANSYS FLUENT. The bulk pressure surpasses the critical value and the wall temperatures enclose the pseudo-boiling temperature. This setup has been studied in [8, 9] serving as comparison database.

The overall target is to assess the prediction capability of industrial RANS tools for cooling duct flows with a focus on the influence of the turbulent heat flux closure.

2 High Aspect Ratio Cooling Duct

This section focuses on the asymmetrically heated HARCD. Results for the RANS BSL RSM in combination with different heat flux closure models are compared to a LES to assess the prediction capability of secondary flow and turbulent heat transfer.

2.1 Equation System and Numerical Model

For the RANS simulations the compressible Navier-Stokes equations (NSE) with the total energy equation are used as implemented in ANSYS CFX, see [1, 2]. The fluid properties are evaluated based on the IAPWS IF97 formulation. To close the equation system approximations for $\overline{\rho u'_i u'_j}$ and $\overline{\rho u'_i h'}$ are required. Reference [17] showed, that the ω -based BSL RSM gives the overall best results for the HARCD setup. Additional PDEs are solved for each component of $\overline{\rho u'_i u'_j}$ and the specific dissipation ω . At the walls the so-called automatic wall treatment functionality is employed.

For modelling $\overline{\rho u'_i h'}$ we utilise the state of the art gradient approach with a constant Pr_t , two algebraic and a second moment closure model. For the gradient approach the turbulent heat fluxes are proportional to the enthalpy gradients and the isotropic turbulent diffusivity α_t with $\alpha_t = \nu_t / Pr_t$. The algebraic Daly-Harlow and the improved Younis models employ an anisotropic α_t -tensor as a function of the Reynolds stress tensor, see [7, 32]. For the second moment closure model an additional PDE is solved for each component of $\overline{\rho u'_i h'}$. The latter is a beta feature within ANSYS CFX (CADFEM GmbH, personal communication, 2018).

For the LES database of [19] the incompressible NSE with the Boussinesq approximation are applied. The transport properties are evaluated using the IAPWS correlations. For time discretisation a third-order Runge-Kutta scheme with $CFL = 1$ is utilised and for spatial discretisation a second-order finite-volume method. As an implicit LES is performed, the size of the subgrid scales (SGS) is determined by the chosen grid resolution. As SGS model the adaptive local deconvolution method (ALDM) is used, see [13].

2.2 Simulation Setup

The setup consists of two domains simulated independently, see Fig. 1. The adiabatic periodic section is $50 \times 25.8 \times 6 \text{ mm}^3$ and the heated section is $600 \times 25.8 \times 6 \text{ mm}^3$.

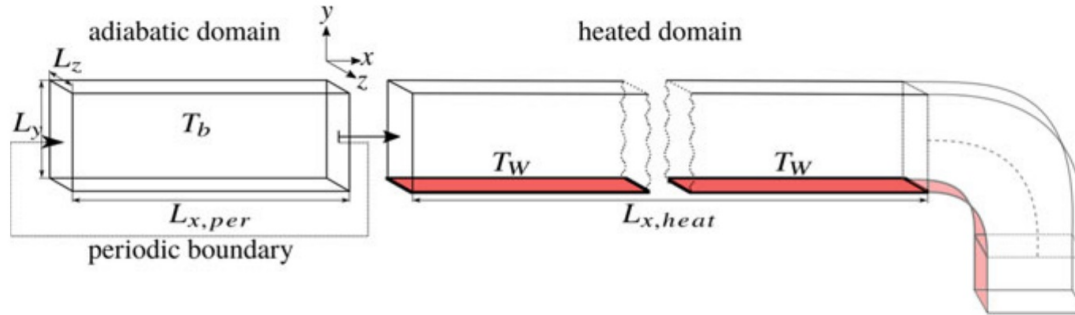


Fig. 1 Simulation setup with the focus of the current investigation on the non-faded part

The straight part is followed by a curved section, which is not part of the current study and analysed in [17]. The grid resolution for the well-resolved RANS has been determined with an extensive grid sensitivity study based on the periodic section and satisfies $y^+ \approx 1$ for the adiabatic and heated walls. In total $34/512 \times 115 \times 64$ nodes are used for the periodic, respectively the heated domain.

The periodic duct serves to generate a fully developed turbulent HARCD inflow profile. The simulation is performed with liquid water treated as incompressible with fixed fluid properties at $T_b = 333.15$ K. All walls are defined as smooth adiabatic walls. In streamwise direction a periodic boundary condition is set with a constant mass flow of $\dot{m} = 0.8193$ kg/s corresponding to $u_b = 5.3833$ m/s and $Re_b = 110 \cdot 10^3$. Convergence is accelerated by using physical and local time stepping methods and lowering the pressure update multiplier, and is reached when a RMS target value of $1 \cdot 10^{-6}$ is surpassed for the momentum and continuity equation residuals.

For the heated domain simulations the compressible NSE are used. All walls are treated as smooth walls with the automatic wall treatment option applied. The lower wall is an isothermal wall with a fixed $T_W = 373.15$ K and the remaining are adiabatic walls. At the inlet velocity and turbulence fields from the periodic domain are prescribed, and at the outlet an average pressure of $p_{out} = 101325$ Pa is set. Convergence is accelerated by using physical and local time stepping methods, and is reached when a RMS target value of $1 \cdot 10^{-6}$ is surpassed for the momentum, continuity and total energy equation residuals.

2.3 Flow and Temperature Field

In the following, the RANS results of the BSL RSM turbulence model in combination with different turbulent heat flux closures are compared to the LES of [19].

Figure 2 shows the cross-sectional flow and temperature field and Fig. 3 depicts the flow and temperature profiles along the duct midplane at $x = 300$ mm after the beginning of the heated straight HARCD. As the choice of turbulent heat flux closure has a negligible effect on the velocity field all RANS results coincide in Fig. 3a/b. We observe for the streamwise velocity of the adiabatic duct results, that the LES

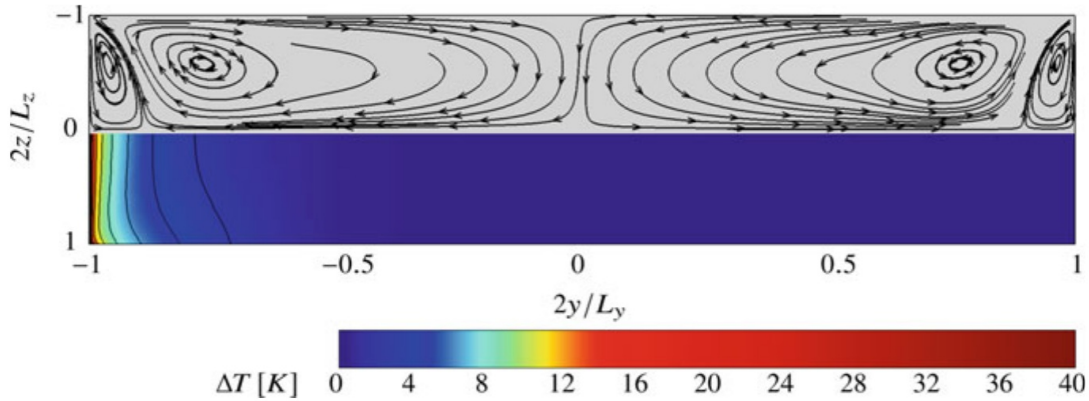


Fig. 2 Secondary flow and temperature field at $x = 300$ mm for the BSL RSM with $Pr_t = 0.9$. Isolines are drawn from 2 K to 40 K in steps of 2 K

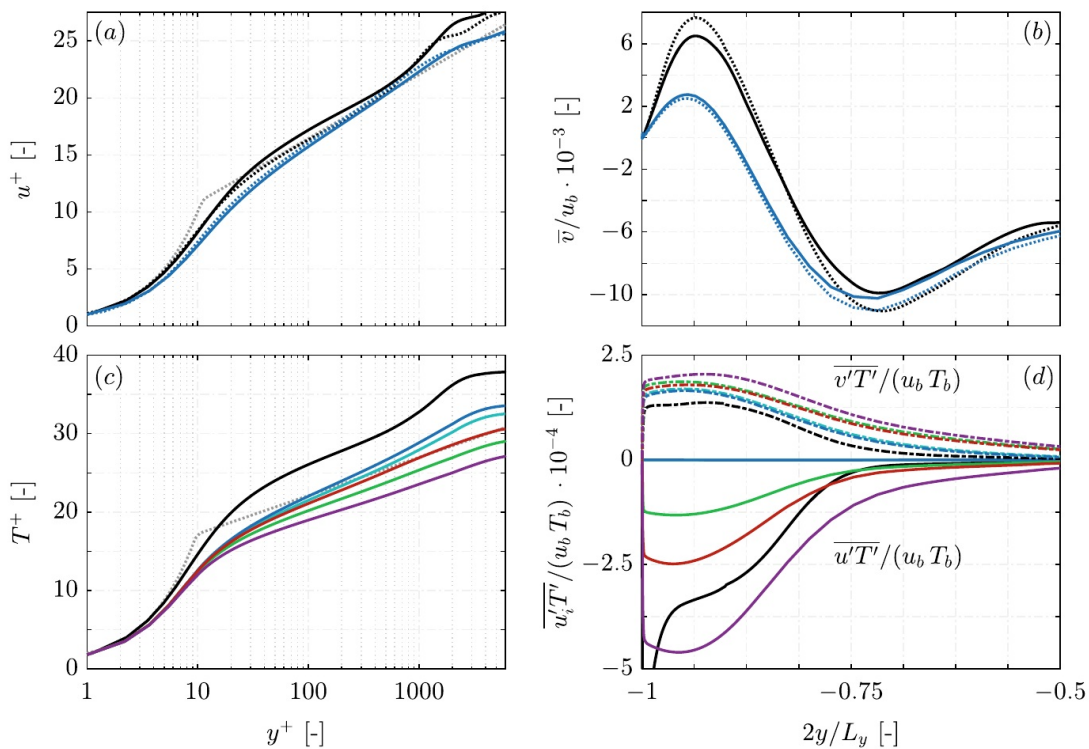


Fig. 3 Streamwise (a) and secondary flow velocity (b), temperature (c) and turbulent heat flux distribution (d) along $2z/L_z = 0$ at $x = 300$ mm for the LES (—) and the BSL RSM with $Pr_t = 0.85$ (—), $Pr_t = 0.9$ (—), Daly-Harlow model (—), Younis model (—) and PDE model (—). In a/b the adiabatic results are plotted as dotted lines. In a/c the analytical law of the wall and the empirical function of Kader are plotted as (.....)

follows closely the analytical law of the wall, $u^+ = 1/0.41 \cdot \ln y^+ + 5.2$, whereas in the RANS the velocity is underestimated in the viscous sublayer and buffer layer. The heating leads to an upwards shift in the log-law region, which is not represented by the RANS.

The secondary flow field in the HARCD consists of a counter-rotating vortex pair in each corner, a smaller vortex above the heated wall and a larger one along the lateral wall. Figure 3b depicts the heated wall-normal velocity with the maximum being the footprint of the small vortex and the minimum that of the large vortex in the duct midplane. The small vortex strength is significantly underestimated in the RANS, whereas the large vortex strength agrees well with the LES data. Using other turbulence models than the BSL RSM, the results deviate further from the LES, see [17]. When heating is applied the secondary flow strength becomes weaker along the duct, [19]. The RANS captures this behaviour only for the large vortex, whereas the small vortex strength slightly increases.

In Fig. 3c normalised temperature profiles are shown with $T^+ = T/T_\tau$ and $T_\tau = q_w/(\rho_w c_{p_w} u_\tau)$. Kader's law [15] is defined as $T^+ = Pr y^+$ for the viscous sublayer and $T^+ = 2.12 \ln(y^+) + (3.85 Pr^{1/3} - 1.3)^2 + 2.12 \ln(Pr)$ for the log-law region, assuming Pr and Pr_t to be constant and pure channel flow. The LES follows Kader's law in the sublayer and shows a significant upwards shift in the log-law region due to the secondary flow presence generating a local hot spot in the midplane. Strong differences between the RANS heat flux closure models become apparent in the log-law region, however, the temperature is underestimated for all models. One reason is the significantly weaker small vortex. From the BSL RSM with $Pr_t = 0.9$ over $Pr_t = 0.85$ and the algebraic models to the PDE-model, an increasing downwards shift of the T^+ -profile is visible and a reduction of the profile-slope. Overall the T^+ -deviation from the LES grows, accompanied by an increasing deviation of the local and global heat transfer. The integral wall heat flux over the first 500 mm increases from 3.2 kW in the LES over 3.6 kW for BSL RSM with $Pr_t = 0.9$ and 3.9 kW for the Younis-model to 4.35 kW for the PDE model. Likewise, the lower wall shear stress is overestimated in the RANS with $\tau_{w,RANS} \approx 51.0$ Pa for all closure models versus the LES value of 45.7 Pa. Without heating the values show less deviation with $\tau_{w,LES} = 53.2$ Pa and $\tau_{w,RANS} = 54.8$ Pa. The observed deviations are possibly due to the usage of the automatic wall treatment option of ANSYS CFX.

The turbulent heat flux comparison in Fig. 3d shows, that $\overline{u'T'}$ is underestimated in the RANS unless the PDE model is employed. The Younis model offers an improvement over the simpler Daly-Harlow model and the $Pr_t = const.$ models. For the latter $\overline{u'T'} \approx 0$ due to the negligible streamwise temperature gradient. The $\overline{u'T'}$ -maximum close to the heated wall cannot be represented by the RANS, see [17] for further details. The wall-normal turbulent heat flux is overestimated for all considered RANS models. A similar behaviour as for the temperature and the wall heat flux is observed: the deviation from the LES increases from the $Pr_t = const.$ models over the algebraic models to the PDE model, providing a further explanation for the overestimated heat transfer in the RANS simulations.

3 Channel Flow with Strong Property Variations

This section focuses on the transcritical channel flow. Results for the RANS BSL RSM in combination with different heat flux closure models are compared to LES to assess the prediction capability of the flow field with strong property variations.

3.1 Equation System and Numerical Model

The LES was performed solving the three-dimensional compressible continuity, momentum and total energy equations. The finite-volume method is applied in order to spatially discretise the governing equations on a block structured, curvilinear grid. The compact four cell stencil approach by [10] is used to compute the convective fluxes. A physically consistent subgrid-scale turbulence model based on ALDM [12] is implicitly included in the convective flux calculation. More information about the LES simulation can be found in [9].

The compressible NSE are solved for all transcritical RANS simulations using ANSYS FLUENT [3, 4]. The Reynolds stresses are modelled using the ω -based BSL RSM showing the best results in our preliminary tests. The free stream sensitivity within the BSL RSM model is removed by scaling the baseline $\kappa - \omega$ equations. The ω -equation can be integrated throughout the viscous sublayer allowing for a blending between the viscous sublayer and logarithmic layer formulation. The turbulent heat flux is modelled establishing a relationship between the eddy diffusivity and turbulent Prandtl number. In this study we used $Pr_t = 0.85$ (default in FLUENT) and an algebraic formulation by Kays and Crawford (KC) [21].

Thermodynamic and transport properties are obtained using an adaptive look-up table method, which is based on the REFPROP database [23]. This method has been used for the LES and RANS simulations extracting thermodynamic and transport properties from the tabulated look-up database via trilinear interpolation. The accuracy of the extracted values has been shown in [9].

3.2 Simulation Setup

A generic channel flow configuration is used to focus this study on transcritical heat transfer and on the impact of non-linear thermodynamic effects on turbulent flows. Periodic boundary conditions are imposed in stream- and spanwise direction, and isothermal no slip boundary conditions are applied at the top and bottom walls. The channel geometry is $2\pi h \times 2h \times \pi h$ in the streamwise, wall-normal and spanwise direction, respectively, see Fig. 4. The channel half-height h is used as characteristic length. A hyperbolic stretching law is applied in wall-normal direction in order to

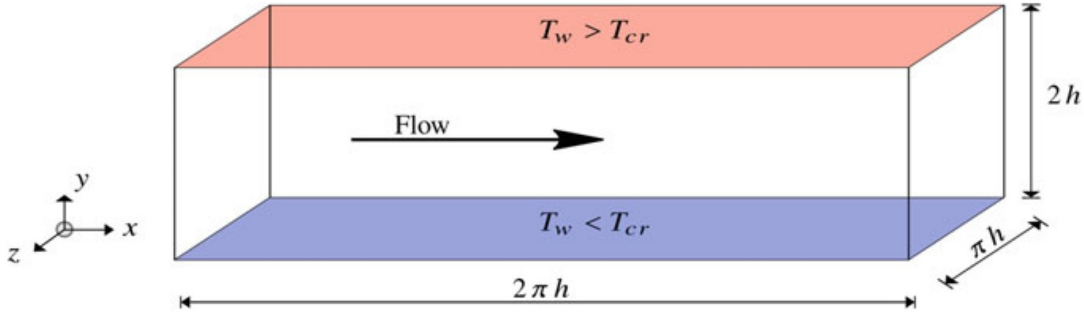


Fig. 4 Computational domain with a hot wall at the top and a cold wall at the bottom at supercritical pressure

fulfill the resolution requirements at walls, whereas a uniform grid spacing is used in the stream- and spanwise direction. Roughness and gravity effects are not considered in the simulations.

Methane is used as working fluid with its critical pressure of $p_{cr} = 4.5992$ MPa and critical temperature of $T_{cr} = 190.564$ K. The bulk pressure is $p_b \approx 5.0$ MPa, corresponding to a reduced pressure of $p_r = p_b/p_{cr} = 1.09$. The cold wall temperature is set to $T_{wc} = 180$ K ($T_{wc} < T_{cr}$) and the hot wall temperature to $T_{wh} = 400$ K ($T_{wh} > T_{cr}$), thus a temperature ratio of $T_{wh}/T_{wc} = 2.22$ is obtained. These boundary conditions encompass the pseudo-boiling temperature of $T_{pb} \approx 193.6$ K at p_b and result in a density ratio of $\rho_{wc}/\rho_{wh} = 12.0$.

A body force in the momentum and energy equation is added to maintain a constant mass flux, which corresponds to a bulk velocity of $u_b = 74$ m/s. This results in a bulk Reynolds number of $Re_b = (u_b 2h \rho_b)/\mu_b \approx 1.67 \cdot 10^4$. The LES and RANS simulations are initialised with a parabolic velocity profile. A linear temperature distribution with a bulk pressure of 5 MPa is prescribed to accelerate the convergence and reduce high gradients at the beginning of the simulations. Results obtained with the SST model are used as initial guess for the BSL RSM simulations. Convergence is reached when a RMS target value of $1 \cdot 10^6$ is surpassed for the momentum, continuity, total energy and RSM transport equation residuals.

3.3 Flow and Temperature Field

In the following, the RANS simulations using the BSL RSM turbulence model together with a constant turbulent Prandtl number and the KC model are compared with the LES. The mean flow properties in the LES are generated by averaging in time and subsequently in streamwise and spanwise direction after reaching a quasi-stationary state.

Figure 5a shows the van Driest transformed mean velocity distribution at the cold and hot wall side over wall units. Since the turbulent heat flux model has a minor effect on the velocity similar results for the constant turbulent Prandtl number and

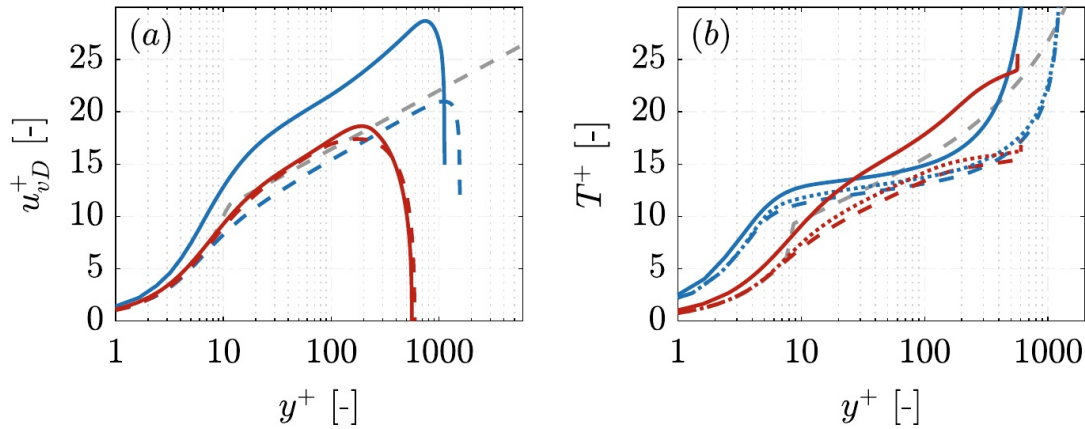


Fig. 5 Mean flow properties over wall units with the van Driest transformed velocity in (a) and transformed temperature in (b). The analytical law of the wall with $\kappa = 0.41$ and $B = 5.2$, and the empirical function of Kader are plotted as (-----). LES (——), BSL RSM with $Pr_t = 0.85$ (----) and BSL RSM with Kays and Crawford model (.....)

the KC model are achieved. For this reason, the velocity profiles using the KC model have been excluded in Fig. 5a. A good agreement is observed between the LES and the RANS simulation at the hot wall. The profiles also follow the analytical log law with $\kappa = 0.41$ and $B = 5.2$, since the fluid exhibits an ideal gas like behavior towards the hot wall. The latter has been shown using the compressibility factor in [9]. The pseudo-boiling position is located at $y^+ \approx 11$ in the vicinity of the cold wall, where strong property variations are present. As a consequence, the LES and RANS do not coincide and do not follow the law of the wall. Other studies [9, 20, 22, 24] showed, that no general transformation including the semi-local scaling [14] and the transformation by Trettel and Larsson [30] is able to collapse the mean velocity profiles for transcritical flows throughout the viscous sublayer and log law region onto the analytical law of the wall.

The temperature distribution is shown in Fig. 5b using T^+ , see Sect. 2.3. The distribution at both walls exhibits a viscous sublayer and log law with different slopes. The specific heat capacity peak at the pseudo-boiling position acting as a heat sink leads to a flattening at the cold wall. Only a small difference is observed between RANS and LES, which is slightly improved using the KC model for the turbulent Prandtl number. Due to the strongly varying molecular Prandtl number no analytical law of the wall formulation is included at the cold wall. The RANS and LES profiles at the hot wall diverge with increasing wall distance. The RANS profiles follow the empirical formulation by Kader, see Sect. 2.3, in the sublayer, but underestimate the temperature in the log layer. Using KC model for Pr_t slightly adjusts the temperature towards the Kader law.

The turbulent Prandtl number profiles are compared in Fig. 6. The turbulent Prandtl number in the LES is derived based on the enthalpy since the perfect gas relation $h = c_p T$ is not valid in transcritical flows [8]. A good agreement between RANS and LES is achieved at the cold wall for $y^+ > 10$, but the turbulent Prandtl number

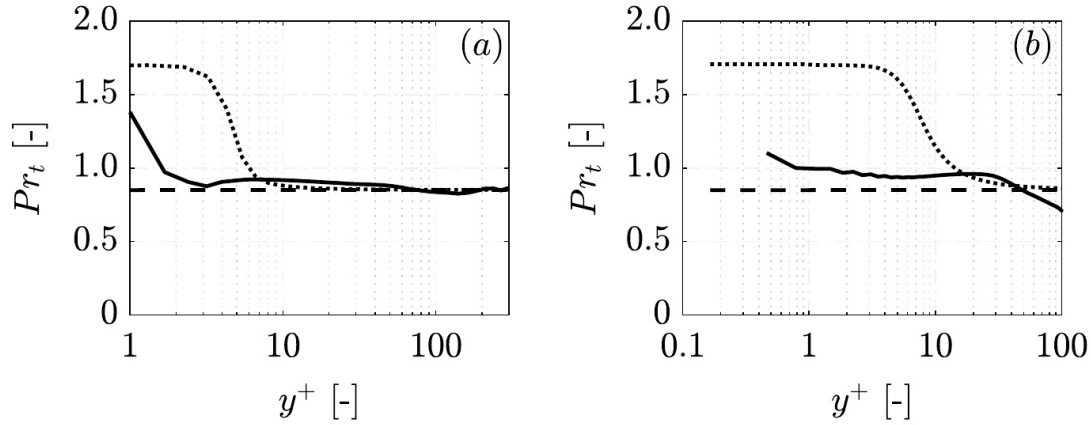


Fig. 6 Turbulent Prandtl number distribution over wall units. Pr_t at the cold (a) and hot wall (b). LES (—), BSL RSM with $Pr_t = 0.85$ (---) and BSL RSM with Kays and Crawford model (.....)

Table 1 Summary of integral values for LES and RANS simulations

	τ_{w_c} [Pa]	τ_{w_h} [Pa]	$ \dot{q}_{w_c} $ [MW m ⁻²]	$ \dot{q}_{w_h} $ [MW m ⁻²]
LES	1257	708	3.48	3.00
BSL RSM with $Pr_t = 0.85$	2420	802	5.26	4.95
BSL RSM with KC	2410	804	5.03	4.72

in the LES starts to increase closer to wall. This can also be observed at the hot wall, where the KC formulation increases earlier to the wall value of 1.70.

The evaluation of the integral wall values for the performed simulations in Table 1 shows, that the wall shear stress at the hot wall for the RANS with $Pr_t = 0.85$ is close to the LES. The discrepancy in the velocity profiles at the cold wall can also be seen by means of the wall shear stress, which is approximately double as high in the LES. Higher heat flux values in the RANS simulations result in the observed smaller temperature values compared to the LES. The use of KC for Pr_t does not lead to major improvements in the integral values. Thus, the Reynolds stress modelling has to be analysed and improved as proposed by [20].

4 Summary and Conclusion

We have conducted RANS simulations using the BSL RSM in combination with various turbulent heat flux closure models for an asymmetrically heated high aspect ratio water cooling duct and a transcritical channel flow including strong property variations within. For the former we used the commercial solver ANSYS CFX and for the latter ANSYS FLUENT. The results have been compared to well-resolved LES simulations.

For the HARCD, the BSL RSM was used in combination with $Pr_t = 0.85$, $Pr_t = 0.9$, the algebraic Daly-Harlow and Younis models and additional PDEs for the individual heat flux components. We observed for the secondary flow field, that the small vortex strength and extension is significantly underestimated and that the large vortex strength is in good agreement with the LES. Due to the weaker secondary flow the dimensionless temperature T^+ is underestimated for all RANS model combinations. Using more complex heat flux closure models, the deviation from the LES increases further from the constant Pr_t model over the algebraic models to the PDE model. Likewise, the wall-normal turbulent heat flux $\overline{v'T'}$ is overestimated and the deviation increases using a more complex heat flux closure. The T^+ -underestimation is accompanied by an overestimation of the local and the global wall heat flux. Similarly the wall shear stresses are overestimated in the RANS with a higher deviation for the heated than the adiabatic duct. A possible reason is the usage of the automatic wall treatment option by ANSYS CFX.

For the transcritical channel case thermodynamic and transport properties have been modelled using the look-up table method. The BSL RSM turbulence model has been used in combination with a constant turbulent Prandtl number of 0.85 and the formulation by Kays and Crawford as heat flux closure. The van Driest transformed velocity profiles show a good agreement between RANS and LES following the law of the wall at the hot wall. A discrepancy has been observed at the cold wall, where the pseudo-boiling is present. This mismatch can also be seen in the wall shear stress values. The temperature is flattened at the cold wall due to the heat capacity peak. The temperature profiles in the RANS simulations are underestimated compared to the LES, which is related to the higher wall heat flux values. An improved heat flux closure given by KC results in only minor improvements in the temperature profiles. These results lead to the conclusion, that the Reynolds stress modelling has to be addressed in order to overcome the mismatch in the vicinity of the pseudo-boiling to achieve the correct wall shear stresses.

Acknowledgements Financial support has been provided by the German Research Foundation (Deutsche Forschungsgemeinschaft – DFG) within the framework of the Sonderforschungsbereich Transregio 40, SFB-TRR40 (Technological foundations for the design of thermally and mechanically highly loaded components of future space transportation systems). Computational resources have been provided by the Leibniz Supercomputing Centre Munich (LRZ).

References

1. ANSYS, Inc.: ANSYS CFX-Solver Modeling Guide, Release 14.0 (2011)
2. ANSYS, Inc.: ANSYS CFX-Solver Theory Guide, Release 14.0 (2011)
3. ANSYS, Inc.: ANSYS Fluent, Release 19.2, HelpSystem, Theory Guide
4. ANSYS, Inc.: ANSYS Fluent, Release 19.2, HelpSystem, User's Guide
5. Banuti, D.T., Raju, M., Ma, P.C., Ihme, M., Hickey, J.P.: Seven questions about supercritical fluids-towards a new fluid state diagram. In: 55th AIAA Aerospace Sciences Meeting, 2017-1106 (2017)

6. Choi, H.S., Park, T.S.: The influence of streamwise vortices on turbulent heat transfer in rectangular ducts with various aspect ratios. *International Journal of Heat and Fluid Flow* **40**, 1–14 (2013)
7. Daly, B.J., Harlow, F.H.: Transport equations in turbulence. *Physics of Fluids* **13**(11), 2634–2649 (1970)
8. Doehring, A., Schmidt, S., Adams, N.: Large-eddy simulation of turbulent channel flow at transcritical states. In: Eleventh International Symposium on Turbulence and Shear Flow Phenomena (TSFP11), Southampton (2019)
9. Doehring, A., Schmidt, S., Adams, N.: Numerical Investigation of Transcritical Turbulent Channel Flow. In: 2018 Joint Propulsion Conference, Cincinnati (2018)
10. Egerer, C.P., Schmidt, S.J., Hickel, S., Adams, N.A.: Efficient implicit LES method for the simulation of turbulent cavitating flows. *Journal of Computational Physics* **316**, 453–469 (2016)
11. Gavrilakis, S.: Numerical simulation of low-Reynolds-number turbulent flow through a straight square duct. *Journal of Fluid Mechanics* **244**, 101–129 (1992)
12. Hickel, S., Egerer, C.P., Larsson, J.: Subgrid-scale modeling for implicit large eddy simulation of compressible flows and shock-turbulence interaction. *Physics of Fluids* **26**, (2014)
13. Hickel, S., Adams, N.A., Domaradzki, J.A.: An adaptive local deconvolution method for implicit LES. *Journal of Computational Physics* **213**(1), 413–436 (2006)
14. Huang, P.G., Coleman, G.N., Bradshaw, P.: Compressible turbulent channel flows: DNS results and modelling. *Journal of Fluid Mechanics* pp. 185–218 (1995)
15. Kader, B.: Temperature and concentration profiles in fully turbulent boundary layers. *International Journal of Heat and Mass Transfer* **24**, 1541–1544 (1981)
16. Kaller, T., Hickel, S., Adams, N.: LES of an Asymmetrically Heated High Aspect Ratio Duct at High Reynolds Number at Different Wall Temperatures. In: 2018 Joint Thermophysics and Heat Transfer Conference, Atlanta (2018)
17. Kaller, T., Hickel, S., Adams, N.: Prediction Capability of RANS Turbulence Models for Asymmetrically Heated High-Aspect-Ratio Duct Flows. In: 2020 AIAA SciTech Forum, Orlando (2020)
18. Kaller, T., Pasquariello, V., Hickel, S., Adams, N.: Large-eddy simulation of the high-Reynolds-number flow through a high-aspect-ratio cooling duct. In: Proceedings of the 10th International Symposium on Turbulence and Shear Flow Phenomena (TSFP-10), Chicago (2017)
19. Kaller, T., Pasquariello, V., Hickel, S., Adams, N.A.: Turbulent flow through a high aspect ratio cooling duct with asymmetric wall heating. *Journal of Fluid Mechanics* **860**, 258–299 (2019)
20. Kawai, S.: Heated transcritical and unheated non-transcritical turbulent boundary layers at supercritical pressures. *Journal of Fluid Mechanics* **865**, 563–601 (2019)
21. Kays, W.M., Crawford, M.E.: *Convective Heat and Mass Transfer*, 3rd edn. McGraw-Hill, Inc. (1993)
22. Kim, K., Hickey, J.P., Scalò, C.: Pseudophase change effects in turbulent channel flow under transcritical temperature conditions. *Journal of Fluid Mechanics* **871**, 52–91 (2019)
23. Lemmon, E.W., Huber, M.L., McLinden, M.O.: NIST Standard Reference Database 23: Reference Fluid Thermodynamic and Transport Properties-REFPROP, Version 9.1. National Institute of Standards and Technology (2013)
24. Ma, P.C., Yang, X.I.A., Ihme, M.: Structure of wall-bounded flows at transcritical conditions. *Physical Review Fluids* **3**(3), 1–24 (2018)
25. Pirozzoli, S., Modesti, D., Orlandi, P., Grasso, F.: Turbulence and secondary motions in square duct flow. *Journal of Fluid Mechanics* **840**, 631–655 (2018)
26. Pizzarelli, M., Nasuti, F., Onofri, M.: Numerical Analysis of Three-Dimensional Flow of Supercritical Fluid in Asymmetrically Heated Channels. *AIAA Journal* **47**(11), 2534–2543 (2009)
27. Pizzarelli, M., Nasuti, F., Onofri, M.: Trade-off analysis of high-aspect-ratio-cooling-channels for rocket engines. *International Journal of Heat and Fluid Flow* **44**, 458–467 (2013)
28. Rochlitz, H., Scholz, P., Fuchs, T.: The flow field in a high aspect ratio cooling duct with and without one heated wall. *Experiments in Fluids* **56**(12), 1–13 (2015)
29. Salinas-Vásquez, M., Métails, O.: Large-eddy simulation of the turbulent flow through a heated square duct. *Journal of Fluid Mechanics* **453**, 201–238 (2002)

30. Trettel, A., Larsson, J.: Mean velocity scaling for compressible wall turbulence with heat transfer. *Physics of Fluids* **28**(2), 026,102 (2016)
31. Vinuesa, R., Noorani, A., Lozano-Duran, A., El Khoury, G., Schlatter, P., Fischer, P.F., Nagib, N.M.: Aspect ratio effects in turbulent duct flows studied through direct numerical simulation. *Journal of Turbulence* **15**(10), 677–706 (2014)
32. Younis, B.A., Speziale, C.G., Clark, T.T.: A rational model for the turbulent scalar fluxes. *Proceedings of the Royal Society A: Mathematical, Physical and Engineering Sciences* **461**(2054), 575–594 (2005)

Open Access This chapter is licensed under the terms of the Creative Commons Attribution 4.0 International License (<http://creativecommons.org/licenses/by/4.0/>), which permits use, sharing, adaptation, distribution and reproduction in any medium or format, as long as you give appropriate credit to the original author(s) and the source, provide a link to the Creative Commons license and indicate if changes were made.

The images or other third party material in this chapter are included in the chapter's Creative Commons license, unless indicated otherwise in a credit line to the material. If material is not included in the chapter's Creative Commons license and your intended use is not permitted by statutory regulation or exceeds the permitted use, you will need to obtain permission directly from the copyright holder.

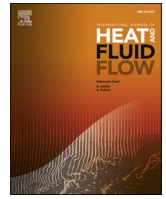


A.2. LARGE-EDDY SIMULATION OF TURBULENT CHANNEL FLOW AT TRANSCRITICAL STATES

A.2.1. RIGHTS AND PERMISSIONS:

This article is available under the Creative Commons CC-BY-NC-ND License (<https://creativecommons.org/licenses/by-nc-nd/4.0/>) and permits non-commercial use of the work as published, without adaptation or alteration provided the work is fully attributed.

A.2.2. MANUSCRIPT



Large-eddy simulation of turbulent channel flow at transcritical states

A. Doehring^{*}, T. Kaller, S.J. Schmidt, N.A. Adams

Institute of Aerodynamics and Fluid Mechanics, Department of Mechanical Engineering, Technical University of Munich, Boltzmannstr. 15, 85748 Garching, Germany

ARTICLE INFO

Keywords:

LES
Transcritical
Channel flow
Turbulent Prandtl number

ABSTRACT

We present well-resolved large-eddy simulations (LES) of a channel flow solving the fully compressible Navier–Stokes equations in conservative form. An adaptive look-up table method is used for thermodynamic and transport properties. A physically consistent subgrid-scale turbulence model is incorporated, that is based on the Adaptive Local Deconvolution Method (ALDM) for implicit LES. The wall temperatures are set to enclose the pseudo-boiling temperature at a supercritical pressure, leading to strong property variations within the channel geometry. The hot wall at the top and the cold wall at the bottom produce asymmetric mean velocity and temperature profiles which result in different momentum and thermal boundary layer thicknesses. Different turbulent Prandtl number formulations and their components are discussed in context of strong property variations.

1. Introduction

Supercritical fluids, whose pressure and temperature are above their critical values, are used in many engineering applications, as for example in gas turbines, supercritical water-cooled reactors (SCWRs) and liquid rocket engines (LRE). They are characterized by a gas-like diffusivity, a liquid-like density and their surface tension is approaching zero. The latter can be observed in the experimental study with cryogenic jets of Mayer and Tamura (1996). At a supercritical pressure the fluid in the experiments was forming finger-like entities with a continuous phase transition instead of droplets and ligaments. Studies, for instance Simeoni et al. (2010), disagree with a continuous phase transition, but have shown a supercritical liquid-like (LL) and gas-like (GL) region with a pseudo-boiling line (PBL), which extends the classical liquid–vapor-coexistence line. In this regard, the transcritical condition refers to the temperature variation from compressed fluid ($T < T_{cr}$, $p > p_{cr}$) to supercritical state ($T > T_{cr}$, $p > p_{cr}$). Furthermore, strong non-linear property variations are present in the vicinity of the PBL, which are induced by intermolecular repulsive forces. As a consequence, the heat transfer and shear forces in wall bounded flows are affected significantly, leading to poor prediction capabilities of Reynolds-averaged Navier–Stokes simulations (RANS) including established turbulence models (Yoo, 2013). Thus, effects like the heat transfer enhancement as well as the onset of heat transfer deterioration in transcritical and supercritical flows cannot be captured correctly. For this reason, high fidelity data are required to assess the heat transfer

prediction capabilities of numerically less expensive turbulence models.

Ma et al. (2018) has performed a Direct numerical simulation (DNS) of a transcritical channel flow using an entropy-stable double-flux model in order to avoid spurious pressure oscillations. They have observed the presence of a logarithmic scaling of the structure function and a k^{-1} scaling of the energy spectra, which supports the attached-eddy hypothesis in transcritical flows. A heated transcritical turbulent boundary layer over a flat plate has been investigated by Kawai (2019) with DNS. His study shows large density fluctuations which are induced by strong changes of thermodynamic properties in the vicinity of the pseudo-boiling. Furthermore, these fluctuations evoke non-negligible Favre-averaged velocity fluctuations which are associated with a turbulent mass flux. In addition, velocity transformations such as the van Driest transformation, the semi-local scaling by Huang et al. (1995) and the transformation by Trettel and Larsson (2016) have failed in transcritical boundary layers. This has also been ascertained by Ma et al. (2018) and Doehring et al. (2018).

In this study, we conduct well-resolved large-eddy simulations (LES) of a transcritical channel flow. The wall temperatures are set in order to enclose pseudo-boiling. Two cases with a different bulk pressure are performed to vary the intensity of non-linear effects. This setup is distinguished by a pseudo-boiling position at $y^+ \approx 14$ and $y^+ \approx 24$ close to the cold wall, whereby the influence of strong property variations on turbulent boundary layers but especially on turbulent eddy viscosity and thermal diffusivity are studied.

^{*} Corresponding author.

E-mail address: alex.doehring@tum.de (A. Doehring).

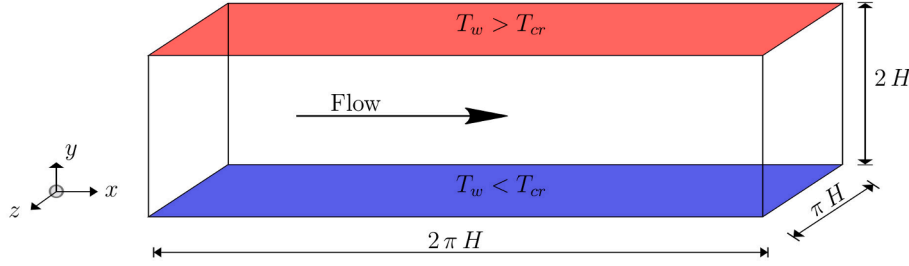


Fig. 1. Computational domain with a hot wall above and a cold wall below the critical temperature at supercritical pressure.

2. Numerical model

LES are performed solving the three-dimensional compressible continuity, momentum and total energy equations. A finite-volume method is applied in order to spatially discretize the governing equations on a block structured, curvilinear grid. An explicit second-order low-storage four-stage Runge–Kutta method with enhanced stability region is applied for time advancement (Schmidt et al., 2006). The compact four cell stencil approach by Egerer et al. (2016) is used to compute the convective fluxes. A discontinuity detecting sensor functional is used to switch the flux calculation between a linear fourth-order reconstruction for high accuracy and a more stable upwind-biased scheme. A physically consistent subgrid-scale turbulence model based on the Adaptive Local Deconvolution Method (ALDM) (Hickel et al., 2006, 2014) is included in the convective flux calculation. Viscous fluxes are determined by a linear second-order centered scheme. An extensive study of the ALDM subgrid-scale model in the context of trans- and supercritical flows was performed by Matheis and Hickel (2018).

Thermodynamic and transport properties are obtained using an adaptive look-up table method based on the REFPROP database (Lemmon et al., 2013). One table is generated for the fluid domain imposing density and internal energy constraints and a second table is used for the boundary conditions imposing pressure and temperature constraints. Thermodynamic and transport properties are extracted from the tabulated look-up database via trilinear interpolation.

3. Setup

A generic channel flow configuration is used to focus this study on transcritical heat transfer and on the impact of non-linear thermodynamic effects on turbulent flows. Periodic boundary conditions are imposed in stream- and spanwise directions, and isothermal no slip boundary conditions are applied at the top and bottom walls. The channel geometry is depicted in Fig. 1. The dimensions are based on the channel half-height H with a size of $2\pi H \times 2H \times \pi H$ in the streamwise, wall-normal and spanwise direction, respectively. In order to fulfill the resolution requirements at walls, we use a hyperbolic stretching law in wall-normal direction, whereas a uniform grid spacing is used in stream- and spanwise directions. The grid parameters are summarized in Table 1 including the number of grid points in each direction N_x , N_y , N_z and the resolution with respect to wall units $\Delta x^+ = \Delta x \rho_w u_\tau / \mu_w$, with the friction velocity $u_\tau^2 = (\tau_w / \rho_w)$ and the wall shear stress $\tau_w = (\mu \partial u / \partial y)|_w$.

Note, that the resolution is based on the whole cell size, but the flow variables are evaluated at the cell center. Therefore, the effective minimum wall distance is $\Delta y_{\min}^+ / 2$. In order to estimate the mesh resolution in terms of thermal scales we employ the ratio between the Batchelor scales η_B and the Kolmogorov scales η introduced by Monin and Yaglom (1975)

$$\frac{\eta_B}{\eta} = \left(\frac{1}{Pr} \right)^{1/2}. \quad (1)$$

This ratio has been used in context of heated transcritical and ideal gas boundary layers by Zonta et al. (2012), Lee et al. (2013), Ma et al.

Table 1
Summary of grid parameters.

	TCF47	TCF57
$N_x \times N_y \times N_z$	$192 \times 192 \times 192$	$192 \times 192 \times 192$
$L_x \times L_y \times L_z$	$2\pi H \times 2H \times \pi H$	$2\pi H \times 2H \times \pi H$
$\Delta x_{\text{cold}}^+ \times \Delta x_{\text{hot}}^+$	23.1×9.5	24.3×11.1
$\Delta z_{\text{cold}}^+ \times \Delta z_{\text{hot}}^+$	11.5×4.8	12.2×5.6
$\Delta y_{\min, \text{cold}}^+ \times \Delta y_{\min, \text{hot}}^+$	0.77×0.32	0.82×0.37
$\Delta y_{\max, \text{cold}}^+ \times \Delta y_{\max, \text{hot}}^+$	16.8×6.9	17.7×8.1
$\Delta y_{T, \min, \text{cold}}^+ \times \Delta y_{T, \min, \text{hot}}^+$	1.12×0.27	1.14×0.32
$\Delta y_{T, \max, \text{cold}}^+ \times \Delta y_{T, \max, \text{hot}}^+$	21.3×8.7	24.47×11.12

(2018), Kaller et al. (2019) and Kawai (2019). We adapt this relationship for the LES context by assuming a proportionality between the thermal and viscous scales including the molecular Prandtl number

$$l_T^+ = l^+ / \sqrt{Pr}, \quad (2)$$

$$\Delta y_T^+ = \Delta y / l_T^+ = \Delta y^+ \sqrt{Pr}. \quad (3)$$

The error made with the used assumption reduces with an increased grid resolution approaching the ratio of Eq. 1. Ma et al. (2018) reported that the grid resolution is governed by the thermal scales and not the viscous scales due to a varying molecular Prandtl number. Since the molecular Prandtl number is partly greater than one in our LES implies that the thermal scales are also smaller than the viscous scales. This can be observed in Table 1 and Fig. 2 by means of dimensionless grid resolution of Eq. 3. The thermal scales are relevant at the cold wall and the

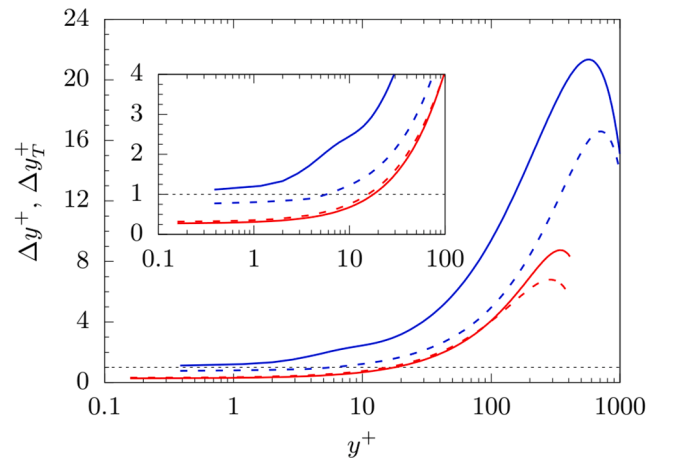


Fig. 2. Wall-normal cell sizes based on the viscous length scale l^+ (---) and thermal length scale $l_T^+ = l^+ (\overline{Pr})^{-0.5}$ (—) for case TCF47 over the dimensionless wall distance y^+ . The cold wall resolution is shown in blue and the hot wall resolution in red. A zoomed in figure is included showing the vicinity of the wall. The thin dashed black line indicates $\Delta y^+ = 1$ and $\Delta y_T^+ = 1$, respectively.

viscous scales at the hot wall regarding the resolution requirements. Based on Eq. 3 the thermal scales are slightly under-resolved, see Table 1. However, the linear behavior of the temperature profile in the viscous sublayer towards the wall shown in Fig. C.17 in the appendix implies a sufficient resolution.

In addition to the minimum and maximum resolution values a grid sensitivity study has been performed due to the strong property variations, see Appendix C. The refinement of the grid leads to an adjustment of the wall shear stress and wall heat flux, thus, to a bulk pressure, which varies from one level to another. As a consequence, the bulk density has been adjusted by trial and error due to non-linearity of the thermodynamics in order to match the bulk pressure for all grid levels. As a trade-off between accuracy and computational cost the resolution of 192^3 has been chosen, although the Reynolds stresses in the streamwise direction do not show a fully converged solution.

The same grid has been used for all performed LES simulations. Roughness and gravity effects are not considered in the simulations in order to ascribe the observed results to non-linear thermodynamic effects and not an interaction of multiple influences. The subscript w refers to values at the wall, b to bulk parameters, cr to critical values, pb to values obtained at the pseudo-boiling position, c to values at the cold wall and h to values at the hot wall.

Methane is used as working fluid with its critical pressure of $p_{cr} = 4.5992$ MPa at a critical temperature of $T_{cr} = 190.564$ K. Two simulations have been performed by adjusting the bulk density in order to obtain the desired bulk pressure. This method is similar to Kim et al. (2019). The intention is to create two cases with certain distance to the critical point in order to capture different intensities of non-linear thermodynamic effects. The naming convention for the performed simulations is related to the obtained bulk pressure. Simulation TCF47 features a bulk pressure of $p_b = 4.75$ MPa, thus a reduced pressure of $p_r = p_b/p_{cr} = 1.03$, whereas simulation TCF57 uses a bulk pressure of $p_b = 5.70$ MPa and a reduced pressure of $p_r = p_b/p_{cr} = 1.24$. In both simulations the cold wall temperature is set to $T_{wc} = 180$ K ($T_{wc} < T_{cr}$) and the hot wall temperature is $T_{wh} = 400$ K ($T_{wh} > T_{cr}$), thus a temperature ratio of $T_{wh}/T_{wc} = 2.22$ is obtained. These boundary conditions encompass the pseudo-boiling temperature and result in a density ratio of $\rho_{wc}/\rho_{wh} = 12.8$.

A body force in the momentum and energy equation is added to maintain a constant mass flux. As a result, a bulk velocity of $u_b = 74$ ms⁻¹ and a maximum Mach number of 0.27 are reached. The additional body force is based on Brun et al. (2008). Several flow parameters for TCF47 and TCF57 are summarized in Table 2.

4. Results

In the following, the mean flow properties are analyzed by averaging in time and subsequently in streamwise and spanwise direction after reaching a quasi-stationary state. The Favre average is defined as $\tilde{\phi} = \overline{\rho\phi}/\bar{\rho}$ and the Reynolds average is an ensemble average denoted with an overline $\bar{\phi}$. The fluctuations are represented as double prime ϕ'' or single prime ϕ' with respect to Favre and Reynolds averages, respectively. For both simulations over 100 flow-through-times have been used for the computation of the mean values. This high number is necessary since

Table 2
Summary of flow parameters.

	TCF47	TCF57
ρ_b [kg/m ³]	74.12	92.60
p_b [MPa]	4.75	5.70
T_b [K]	215.5	219.2
q_{wc}, q_{wh} [MW/m ²]	4.45, 4.2	5.50, 5.2
$Re_{\tau_c}, Re_{\tau_h} = u_{\tau}H/\nu$	705, 290	745, 338
$Re_b = u_bH/\nu$	16500	18500

changes close to the wall are developing very slowly, especially for high order statistics, as for instance triple correlations. For further information about averaging techniques in the context of strongly correlated fluid variables we refer to Huang et al. (1995) and Smits and Dussauge (2006).

4.1. Mean flow field

The Favre averaged mean velocity and temperature profiles are shown in Fig. 3(a) and (b). The temperature is scaled using the wall temperatures $\theta_T = (T - T_{wc})/(T_{wh} - T_{wc})$ and the velocity is scaled by the bulk value u_b . The velocity peak is shifted towards the hot wall, due to the one-sided heating from the top and the associated thermal expansion. As a consequence, the momentum boundary layer at the cold wall is thicker than at the hot wall $\delta_{M_c} > \delta_{M_h}$. The boundary layer thicknesses are determined by using the locus of zero total shear stress $\tau_{tot} = 0$. Except for a minor flattening of the peak value in TCF57 compared to TCF47 no significant difference can be observed between the two velocity profiles. The temperature distribution features strong gradients in the vicinity of the walls. In the vicinity of the cold wall the temperature profile is flattened due to the specific heat capacity peak in Fig. 3(d). The increase of the bulk density in TCF57 also leads to a slight increase of the bulk temperature, which is mostly visible at $y/H < 0.0$. The thermal boundary layers are defined as the distance between the wall and the locus of minimum heat transfer $\bar{q} = -\lambda\partial T/\partial y$. Thus, the thermal boundary layer thickness at the hot wall is approximately 5.5 times the thermal boundary layer thickness at the cold wall. Fig. 3(c) and (d) show the mean density $\theta_\rho = (\rho - \rho_{wh})/(\rho_{wc} - \rho_{wh})$ and specific heat capacity distributions. The adjustment of the bulk density in order to obtain a higher bulk pressure can be observed by an elevated profile for TCF57. The higher bulk pressure with increased distance to the critical pressure of methane leads to a smaller specific heat capacity peak. The pseudo-boiling positions are determined by means of the c_p peak with

$$y_{pb47}/H \approx -0.980 \rightarrow y^+ \approx 14 \quad (4)$$

$$y_{pb57}/H \approx -0.969 \rightarrow y^+ \approx 23. \quad (5)$$

Due to strong property variations the mean Prandtl number $\bar{Pr} = \mu c_p/\lambda$ varies over the channel height from 0.76 to 5.2, see Fig. 3(e). Especially close to the pseudo-boiling position strong changes are observed, where momentum diffusivity is dominating and thermal diffusivity $\bar{\alpha} = \lambda/(\rho c_p)$ reaches a minimum, see Fig. 3(f). This stems from the specific heat capacity peak acting as a heat sink and leading to the observed flattening of the temperature profile. In addition, a local Prandtl number minimum occurs after the peak value for TCF47 shown in the inset of Fig. 3(f). This local minimum is not observed for TCF57 or in DNS studies (Kim et al., 2019; Ma et al., 2018; Kawai, 2019) and stems from the thermal diffusivity showing a local maximum. We attribute this to real gas effects, since the bulk pressure is very close to the critical value of methane.

4.2. Turbulent Prandtl number

The highly variable Prandtl number of super- and transcritical channel flows affects the thermal boundary layer and the heat transfer over the walls. Thus, RANS turbulence models, which do not account for a highly variable Prandtl number, fail in predicting the correct heat transfer (Yoo, 2013). Likewise the turbulent Prandtl number Pr_t may lead to wrong heat transfer predictions in RANS. It is used as a modeling parameter to close RANS equations by providing a relationship between the turbulent eddy thermal diffusivity ϵ_H and turbulent eddy viscosity ϵ_M . In most cases Pr_t is set to a constant value which is based upon the strong Reynolds analogy (SRA), assuming a correlation between the turbulent heat transfer and the turbulent momentum transfer resulting in

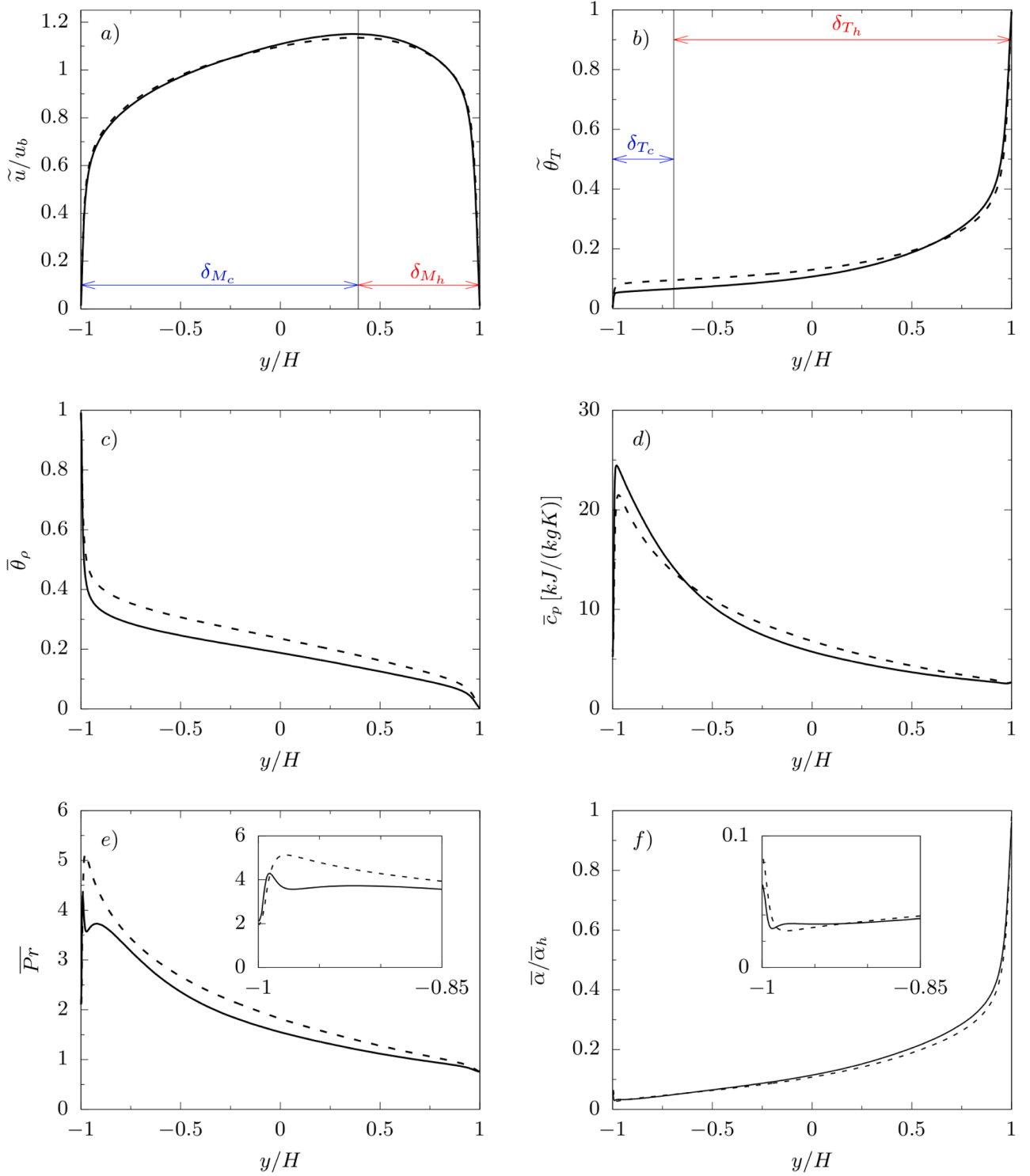


Fig. 3. Mean profiles are depicted over the channel height for case TCF47 — and TCF57 - - -. Favre averaged mean velocity and temperature are shown in a) and b) and mean density and specific heat capacity in c) and d), respectively. Momentum δ_M and thermal δ_T boundary layer thicknesses are included for the cold and hot side regarding case TCF47. Mean Prandtl number e) and mean thermal diffusivity f) profiles are shown over the channel height. The mean thermal diffusivity is scaled with the value at the hot wall $\bar{\alpha}_h$. A zoomed in figure is included for the area close the cold wall.

$$Pr_t = \frac{\epsilon_M}{\epsilon_H} = 1. \quad (6)$$

Experimental and DNS studies have shown, that this simple assumption is not correct, since the turbulent Prandtl number is at least dependent on the wall distance and the molecular Prandtl number, $Pr_t = f(y^+, Pr)$ (Kays, 1994). It was observed, that Pr_t is relatively constant in

the logarithmic region, whereas it is increasing towards the wall and decreasing in the wake region.

For the analysis of the turbulent Prandtl number in the transcritical LES we included two different formulations taken from the literature:

Incompressible:

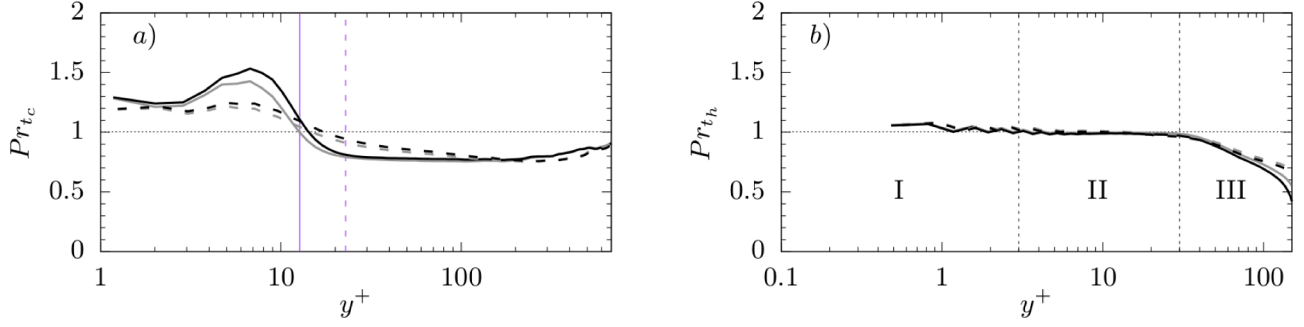


Fig. 4. Turbulent Prandtl number at the cold wall (a) and the hot wall (b) over wall units y^+ for case TCF47 — and TCF57 ----. Included are the incompressible (grey) and compressible (black) formulation. The pseudo boiling position at the cold wall is indicated by a vertical purple line.

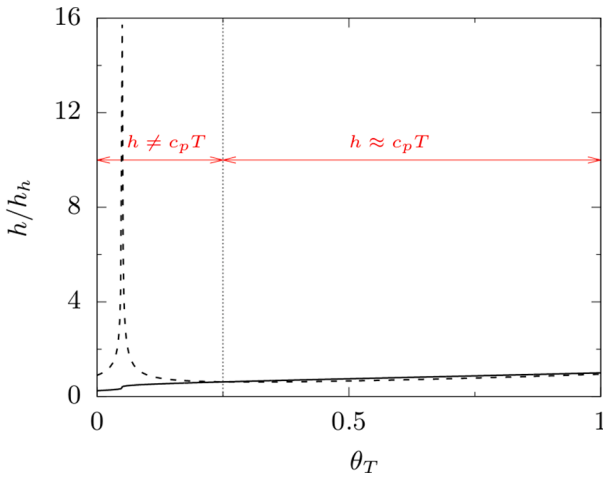


Fig. 5. Comparison of enthalpy h — with the relationship for a calorically perfect gas $c_p T$ ---- at a bulk pressure of $p_b = 47\text{bar}$. Enthalpy h , specific heat capacity c_p and temperature T are taken from the NIST data base. The profiles are scaled with the hot wall value and presented over the scaled temperature range which is present within the channel.

$$Pr_t = \frac{\overline{u'v'}}{\overline{v'T'}} \frac{\partial \overline{T}/\partial y}{\partial \overline{u}/\partial y} \quad (7)$$

Compressible:

$$Pr_t = \frac{\overline{u'v'}}{\overline{v'h'}} \frac{\partial \overline{T}/\partial y}{\partial \overline{u}/\partial y} \quad (8)$$

Reynolds averaged quantities are used for the incompressible formulation in Eq. 7, whereas Favre averaged values are included in the compressible definition in Eq. 8.

Fig. 4 shows the turbulent Prandtl number at the cold and hot wall over the wall normal distance $y^+ = y/l^+$ with $l^+ = \mu_w/(u_w \rho_w)$. A relatively constant turbulent Prandtl number is observed in region II at the hot wall, which is in accordance with ideal gas studies, cf. Kays (1994). This is not surprising, since the compressibility factor (not shown) is close to one and the molecular Prandtl number does not change significantly close to the hot wall ($0.76 < Pr < 0.9$). Approaching the hot wall in region I Pr_t increases up to 1.11 and region III features a linear decrease violating the SRA. For a better prediction of the behavior in region I, a higher resolution at the wall is required. Only a minor difference is observed between the compressible and incompressible formulation and between the two simulations, leading to the conclusion,

that minor compressible effects are present at the hot wall. The turbulent Prandtl number at the cold wall varies strongly close to the pseudo-boiling positions indicated by a purple line. Both formulations feature an s-shaped profile in the vicinity of y_{pb} with different intensities. With increasing bulk pressure in TCF57 and a milder specific heat capacity peak, the difference between the Reynolds and Favre averaged formulations is shrinking and the s-shape is stretched out. In contrast to the hot wall no constant turbulent Prandtl number is observed for both formulations. Hence, the turbulent Prandtl number variation is more intense at the cold wall in the vicinity of y_{pb} and increases as one gets closer to the critical pressure.

So far, we have used common turbulent Prandtl number formulations from the literature, which are applicable for a wide range of flows, but at a closer look both are not suitable for transcritical channel flows. In general, applying a Favre averaging on the governing equations results in the Reynolds stress tensor $\overline{\rho u_i' u_j'}$ for the momentum equations and in the turbulent heat flux $\overline{\rho u_i' h'}$ for the energy equation, where h is the enthalpy. Since transcritical and supercritical fluids are characterized by strong non-linear property variations induced by intermolecular repulsive forces in the vicinity of the PBL, the enthalpy is not proportional to the temperature as for a calorically perfect gas. In Fig. 5 the enthalpy is compared with the relation $c_p T$, which is used for calorically perfect gas. All three quantities are taken from the NIST data base and the profiles are plotted over the scaled temperature range present in the channel at the bulk pressure of $p_b = 47\text{bar}$. A strong deviation is observable close to the pseudo-boiling position ($0 < \theta_T < 0.25$), where the enthalpy has a change in the slope, but does not show a peak. This peak featured by the perfect gas relation stems from the heat capacity, which can be seen in Fig. 3(d). Since the relation $c_p T$ for a calorically perfect gas leads to a significant error in the vicinity of the pseudo-boiling, we suggest to use an enthalpy based turbulent Prandtl number formulation for transcritical channel flows:

$$Pr_t = \frac{\overline{u'v'}}{\overline{v'h'}} \frac{\partial \overline{h}/\partial y}{\partial \overline{u}/\partial y} \quad (9)$$

Fig. 6 shows the turbulent Prandtl number profiles based on the new formulations at the cold and the hot wall. For comparison, also the compressible formulation using temperature is included. Since the specific heat capacity change is relatively small over the hot wall boundary layer, the enthalpy can be approximated using the relation for a calorically perfect gas $h \approx c_p T$. For this reason, all three profiles coincide and feature a relatively constant value in region II at the hot wall. In Fig. 6 (a), the s-shape disappears in region II using the enthalpy based formulation compared to the compressible definition of Pr_t .

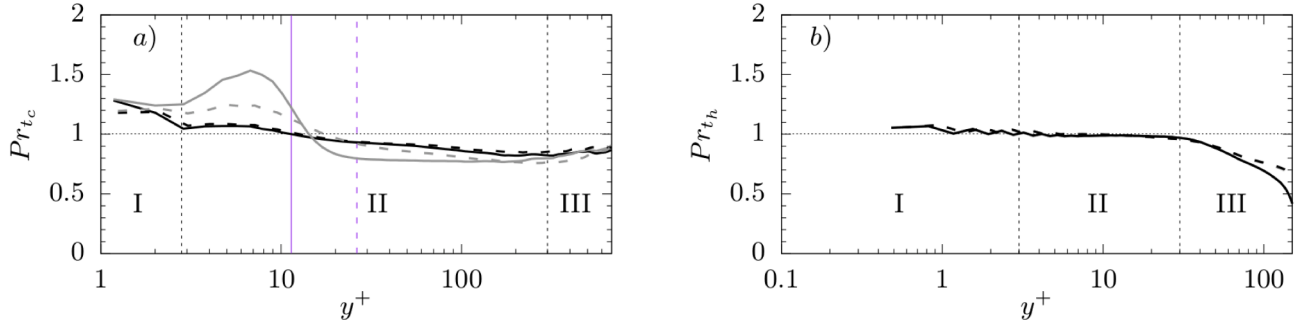


Fig. 6. Turbulent Prandtl number at the cold wall (a) and the hot wall (b) over wall units y^+ for case TCF47 — and TCF57 ----. Included are the compressible (grey) and enthalpy (black) formulation. The pseudo-boiling position at the cold wall is indicated by a vertical purple line.

Furthermore, the turbulent Prandtl number increases approaching the cold wall as it is observed at the hot wall. An additional positive effect using the enthalpy formulation is the good agreement between TCF47 and TCF57 for the most part of the boundary layer.

In the following, the influence of pseudo-boiling on the turbulent shear stress and the heat flux is analyzed, since they are included in the turbulent Prandtl number formulation. Based on the work of Huang et al. (1995), both components can be split in three parts

$$\widetilde{u^i v^j} = \overline{u^i v^j} - \overline{u^i} \overline{v^j} + \frac{\overline{\rho^i u^i v^j}}{\overline{\rho}}, \quad (10)$$

$$\widetilde{v^i h^i} = \overline{v^i h^i} - \overline{v^i} \overline{h^i} + \frac{\overline{\rho^i v^i h^i}}{\overline{\rho}}. \quad (11)$$

His analysis has shown, that the second term in Eqs. 10 and 11 is only 1% of the total and is confined to the sublayer ($y^* < 17$) in compressible channel flows. Thus, the second term can be neglected. For the normalization of the terms the semi-local friction velocity $u_\tau^* = (\tau_w/\rho)$ and enthalpy $h_\tau^* = q_w/(\rho u_\tau^*)$ are used. In order to align the peak positions for the different cases the semi-local wall distance $y^* = y u_\tau^* \rho/\mu$ is applied. Using semi-local values leads to a better collapse between

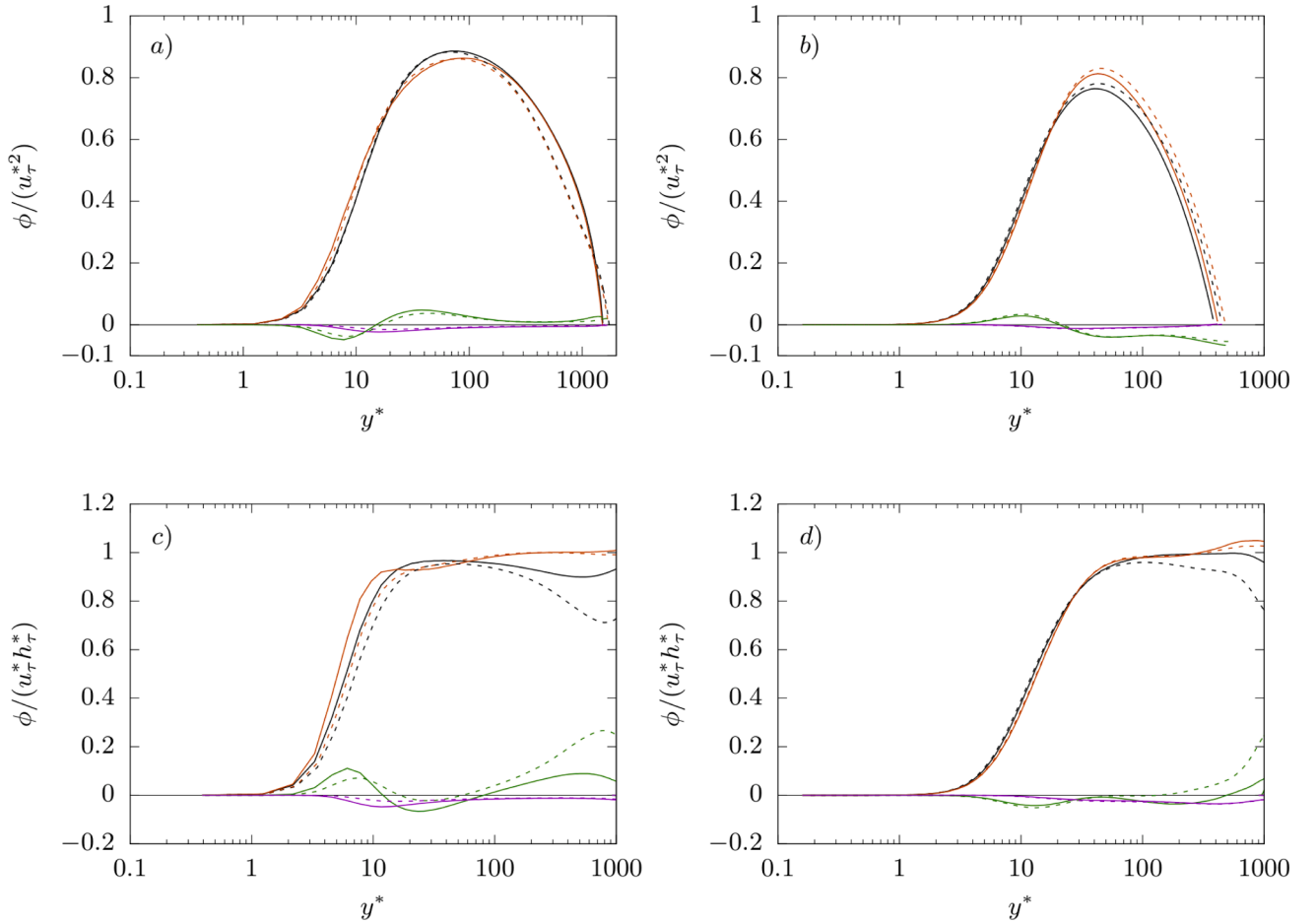


Fig. 7. Terms of Favre averaged turbulent shear stress (a,b) and turbulent heat flux (c,d) normalized with semi-local values over semi-local wall units. The cold wall is shown on the left (a,c) and the hot wall on the right (b,d) with Case TCF47 — and TCF57 ----. Colors: ϕ represents $\widetilde{u^i v^j}$ and $\widetilde{v^i h^i}$ —; $\overline{u^i v^j}$ and $\overline{v^i h^i}$ —; $\overline{\rho^i u^i v^j} / \overline{\rho}$ and $\overline{\rho^i v^i h^i} / \overline{\rho}$ —.

TCF47 and TCF57 compared to a scaling using constant wall properties. The comparison between these two scalings is shown in Appendix B. These observations have also been presented by Patel et al. (2016). The contribution of each term to the total Favre averaged quantity is computed by dividing the respective term by the total Favre averaged stress or flux. Fig. 7(a) and (b) show, that the second and third term of turbulent shear stress are an order of magnitude smaller than the first term. The second term is confined to the buffer and log-layer and reaches 5% and 1.5% of the total shear stress at the cold and hot wall in case TCF47, respectively. It can be observed by comparing to TCF57, that an increase of the property variations leads to slightly higher contributions of the second term. The triple correlation is characterized by an s-shaped profile around zero and contributes to the total shear stress by approximately 25% and 9% at the cold and hot wall in case TCF47, respectively. Hence, the triple correlation has to be taken into account if strong property variations are observed, whereas the second term is negligible, as already observed in compressible flows by Huang et al. (1995). The total shear stress collapses from the wall to the peak position for the two cases, which can also be seen in the study by Patel et al. (2016).

Similar trends can be seen for the turbulent heat flux in Fig. 7(c) and (d). The second term is small enough at both walls in order to be neglected. The triple correlation also features an s-shape with a higher contribution to the total flux compared to the turbulent shear stress. Furthermore, the pseudo-boiling affects the intensity of the second and third term in comparison between the two cases TCF47 and TCF57. The cooling and heating of the walls result in a one-way heat flow towards the cold wall. This leads to an s-shaped temperature profile as shown in Fig. 3 and a heat flux, which does not have a zero crossing. This can be seen in the turbulent heat flux profile, which stays relatively constant throughout the log- and outer layer instead of decreasing after a peak value, as it is the case for the turbulent shear stress.

4.3. Towards RANS modeling

We have shown that the turbulent Prandtl number is not constant in transcritical flows. In order to improve the prediction capabilities of RANS a correct representation of the turbulent stresses and the turbulent Prandtl number is required.

In the following, turbulent Prandtl number models given by Kays and Crawford (1993) and Bae (2016), which are derived using different assumption and models, are assessed. We evaluate these assumptions

with regard to transcritical flows, before comparing their models with the present Pr_t distribution from our LES. At first, a distance l , which is referred to as a 'mixing length', is used to derive the Reynolds analogy for the turbulent heat transfer. Classically, this mixing length is associated with the turbulent viscosity and the turbulent shear stress

$$\overline{u''v''} \sim -\epsilon_M \frac{d\bar{u}}{dy} - l^2 \left| \frac{d\bar{u}}{dy} \right| \frac{d\bar{u}}{dy}. \quad (12)$$

In order to determine the turbulent eddy viscosity without the knowledge of the mean velocity distribution Prandtl (1925) assumed, that the size of the eddies is proportional to their distance to the wall leading to $l = \kappa y$, where κ is the von Kármán constant. The following evaluation of the mixing length for transcritical flows is based on Pirozzoli (2014). We use the turbulent eddy viscosity and the velocity gradient for a posteriori analysis.

$$\frac{l_M(\eta)}{H} = \frac{-\sqrt{\overline{u''v''}}}{u_\tau} \left(\frac{d\bar{u}}{d\eta} \right)^{-1}, \quad (13)$$

with $\eta = y/H$. Fig. 8(a) and (b) show the Prandtl mixing length hypothesis and a formulation derived from the stress balance

$$\frac{l_M(\eta)}{H} = \kappa\eta \quad (\text{black line}), \quad (14)$$

$$\frac{l_M(\eta)}{H} = \kappa\eta(1-\eta)^{0.5} \quad (\text{pink line}). \quad (15)$$

The log-law region is indicated by vertical lines and determined graphically by observing u^+ over y^+ . It has to be mentioned that the Reynolds number is relatively low and an extensive log-law region does not develop. The mixing length at the cold wall shows for both scaling laws the same behavior of a decrease after a peak value. No plateau can be observed within the indicated log-law region that would indicate a constant value κ . At the heated wall the Prandtl mixing length hypothesis features the same behavior whereas the stress balance formulation has a plateau at $\kappa \approx 0.375$. Pirozzoli (2014) observed in his DNS, that the Prandtl mixing length hypothesis performs worse compared to the stress balance scaling. This is in agreement with our observations at the heated wall, but strong property variations affect the stress balance formulation at the cold wall.

The near wall behavior of the turbulent eddy viscosity and thermal

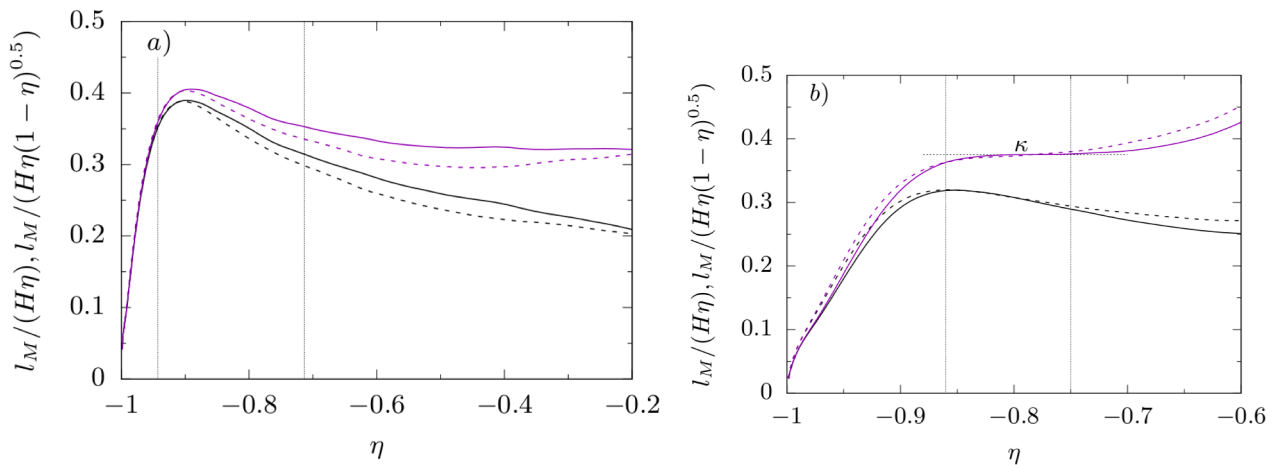


Fig. 8. Mixing length with different scaling at the cold (a) and hot (b) wall over the wall normal distance $\eta = y/H$. The lengths for case TCF47 ——— and TCF57 - - - - are scaled with respect to the wall distance $l_m/(H\eta)$ in black and with respect to the momentum balance $l_m/(H\eta(1-\eta)^{0.5})$ in pink. The beginning and ending of the log-law region are indicated by vertical lines.

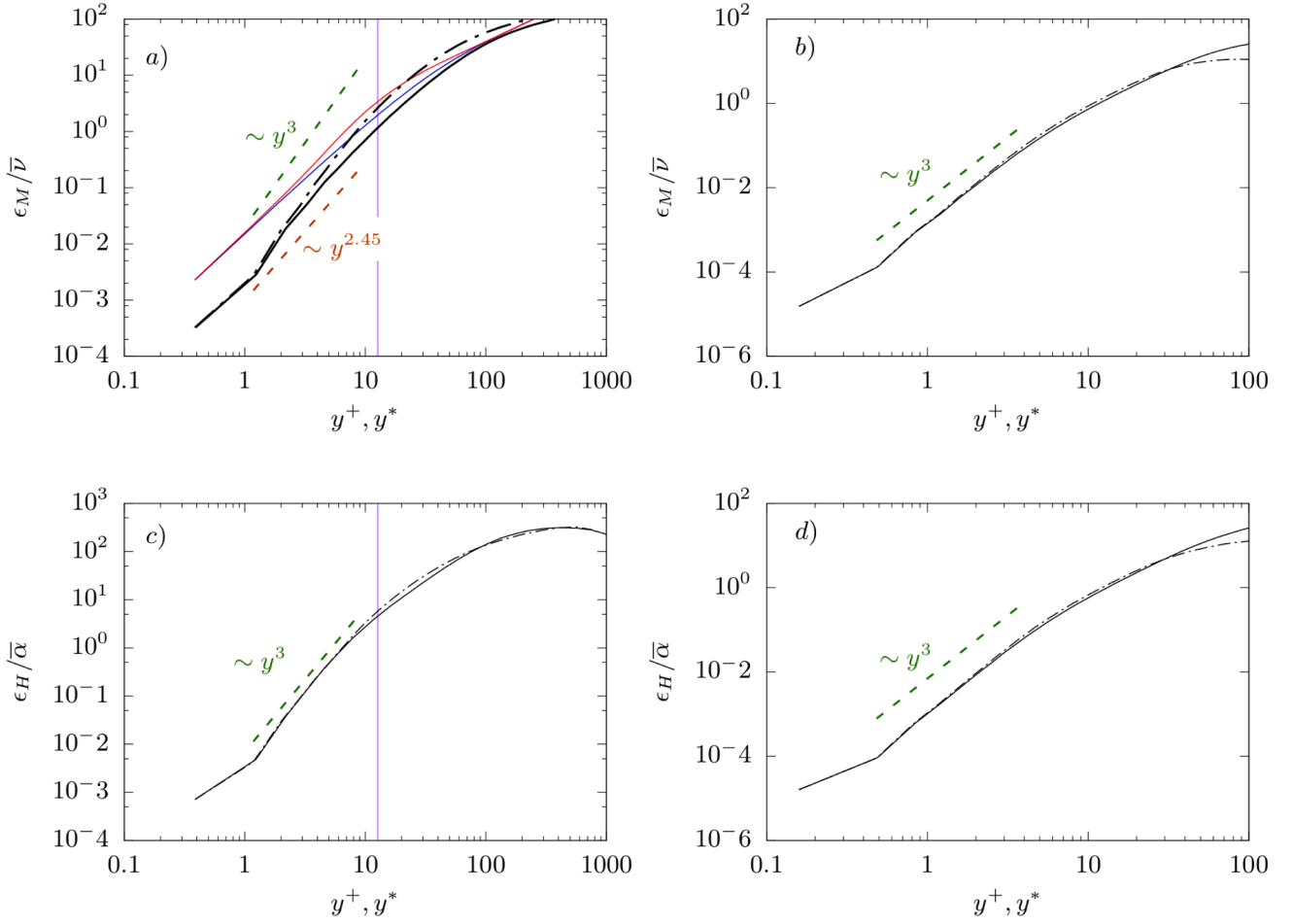


Fig. 9. Turbulent eddy viscosity ϵ_M and eddy thermal diffusivity ϵ_H are scaled with the mean kinematic viscosity $\bar{\nu}$ and thermal diffusivity $\bar{\alpha}$, respectively. Only case TCF47 is shown using a semi-local scaling ($\bar{\nu}, \bar{\alpha}$) — and values at the walls ($\bar{\nu}_w, \bar{\alpha}_w$) - - - over y^+ and y^* , respectively. The cold wall is shown in (a,c) and the hot wall in (b,d). The pink line indicates the pseudo-boiling position for TCF47. The blue line represents $l^+ = \kappa y [1 - \exp(-y^+/A^+)]$ with $A^+ = 26$ and the red line adds the viscosity μ/μ_{w_c} within the damping function.

eddy diffusivity is presented in Fig. 9. It has been shown that both turbulence quantities are proportional to $\sim y^{+3}$ (Kays, 1994; Kim et al., 1987). This proportionality can be derived by Taylor series expansion about y^+ (Antonia and Kim, 1991; Grifoll and Giralt, 2000). In order to see the influence of property variations, we scaled both quantities with the kinematic viscosity $\bar{\nu}$ and thermal diffusivity $\bar{\alpha}$ profiles and with the respective values at the wall. In regard to this scaling y^* and y^+ have

been used, respectively. The profiles of the turbulent eddy viscosity and the thermal eddy diffusivity are only shown for case TCF47, since they are representative for both cases. The comparison between the two scalings shows only minor differences except for the eddy viscosity at the cold wall. Thus, the pseudo-boiling has a higher impact on the eddy viscosity than on the eddy diffusivity, which leads to the linear decrease of the turbulent Prandtl number in region I in Fig. 6(a). In contrast, the

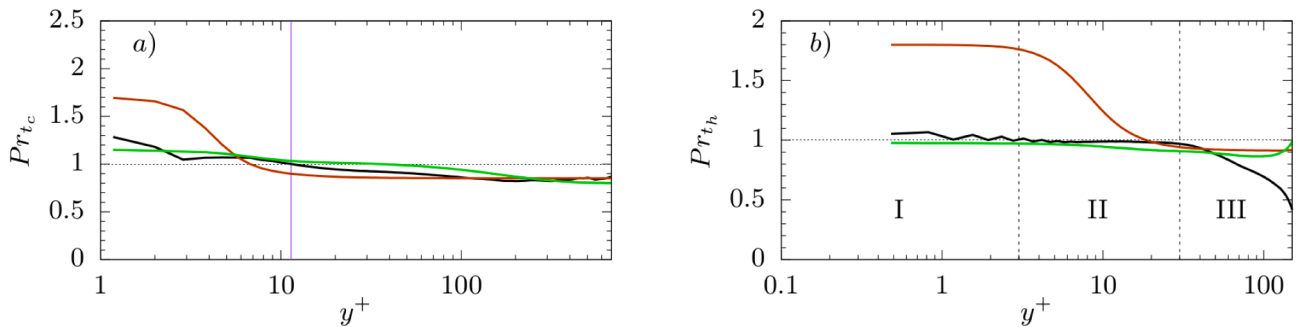


Fig. 10. Turbulent Prandtl number at the cold wall (a) and at the hot wall (b) over wall units y^+ for case TCF47 —. Included are the turbulent Prandtl number formulation by Kays (1994) — and the modified formulation by Bae (2016) —. The pseudo boiling position at the cold wall is indicated by a vertical purple line.

hot wall features nearly identical profiles for the eddy viscosity and the eddy diffusivity, which result in a constant turbulent Prandtl number distribution in Fig. 6(b).

In order to capture the near wall effects using Prandtl's mixing length hypothesis, van Driest added a damping function

$$l^+ = \kappa y [1 - \exp(-y^+/A^+)]. \quad (16)$$

Griffoll and Giralt (2000) showed that the damping function results in a proportionality with \tilde{y}^{+4} . They modified the van Driest constant A^+ in order to obtain \tilde{y}^{+3} . The new constant does not have the correct dependence on y^+ , but it introduces two additional constants, which have to be adjusted at each wall. Steiner and Irrenfried (2019) included a viscosity ratio within the damping function, which does account for property variations. This leads to an adjustment of the mixing length for $y^+ > 5$ at the cold wall, but still no generally applicable constant A^+ was provided.

After the analysis of the mixing length and near wall behavior of the turbulent eddy viscosity and eddy thermal diffusivity, the enthalpy based turbulent Prandtl number is compared to the formulation by Kays and Crawford (1993) and Bae (2016) in Fig. 10. We modified the original formulation by Bae by replacing $c_p T$ with the enthalpy, which results in a new $Pr_{t,0}$ definition. Furthermore, the damping function was removed, since the turbulent Prandtl number in TCF47 and TCF57 increases towards the wall:

$$Pr_{t,Bae} = C + f_2 Pr_{t,0}, \quad (17)$$

with

$$f_2 = 0.5 \left[1 + \tanh\left(\frac{10 - y^+}{200}\right) \right],$$

and

$$Pr_{t,0} = 1 + \frac{\tilde{h}}{\tilde{\rho}} \left| \left(\frac{\partial \tilde{p}}{\partial y} / \frac{\partial \tilde{u}}{\partial y} \right) \right| + \frac{l}{\tilde{\rho}} \left| \frac{\partial \tilde{p}}{\partial y} \right|$$

$$1 + \frac{\tilde{h}}{\tilde{\rho}} \left| \left(\frac{\partial \tilde{p}}{\partial y} / \frac{\partial \tilde{h}}{\partial y} \right) \right| + \frac{l}{\tilde{\rho}} \left| \frac{\partial \tilde{p}}{\partial y} \right|$$

The formulation by Kays taken from Eq. (13-7) in Kays and Crawford (1993) is in good agreement at the cold wall for $y^+ > 6$, but in the viscous sublayer it tends to overpredict Pr_t at both walls. The constant C_{Kays} is set to 0.3 and $Pr_{t,\infty}$ to 0.85 at the cold wall and 0.9 at the hot wall. The adjusted Eq. 17 originally by Bae (2016) is in good agreement with Pr_t at both walls after adjusting C to 0.8 at the cold wall and to 0.5 at the hot wall.

5. Conclusion

We investigated a turbulent transcritical channel flow imposing different wall temperatures, thus, enclosing the pseudo-boiling

Appendix A. Validation

We additionally performed LES simulations of a channel flow with a bulk Reynolds number of $Re_b = 2HU_b/\nu = 21950$ and a friction Reynolds number of $Re_\tau = 590$ (Moser et al., 1999) in order to assess the used LES methodology. The Reynolds numbers are in the range of the performed transcritical LES. Three grid levels are investigated in order to show a grid convergence towards the DNS results. Grid parameters and the obtained resolution are presented in Table A.3. The working fluid is air at a bulk pressure of 1 bar and isothermal no-slip walls at 293 K. No gravity or roughness effects are included. Fig. A.11(a) shows the van Driest transformed mean velocity profiles over the wall normal distance y^+ . With increasing grid resolution the velocity profile approaches the DNS result. A good agreement between the LES and the DNS is observed for TCF_2. The Reynolds stresses

temperature using a well-resolved LES. The fully compressible Navier–Stokes equations have been solved and an adaptive look-up table method has been used for thermodynamic and transport properties. The mean velocity distribution is shifted towards the hot wall leading to different boundary layer thicknesses. Strong property variations in the vicinity of the pseudo-boiling position are observed by means of the molecular Prandtl number, which showed a peak value close to the cold wall. The peak correlates with minimum heat diffusivity leading to a flattening of the mean temperature. As a consequence, the resolution requirements are governed by the thermal scales at the cold wall and by the viscous scales at the hot wall. A grid convergence study for transcritical flows is challenging due to the non-linearity of the thermodynamics. The bulk pressure at each grid level varies due to the adjustment of the wall shear stress and the heat flux. Thus, the bulk density has to be adjusted by trial and error to obtain comparable results at each grid level.

The turbulent Prandtl number is relatively constant and does not depend on the turbulent eddy thermal diffusivity definition at the hot wall, which was ascribed to mild changes of thermodynamic properties. Only the enthalpy based turbulent Prandtl number was unaffected by the pseudo-boiling at the cold wall, whereas the temperature based ones show strong variations. The analysis of the three terms, which form the Favre averaged turbulent shear stress and heat flux shows an increased contribution of the triple correlation.

The turbulent Prandtl number models by Kays and Crawford (1993) and Bae (2016) are able to reproduce the LES distribution by adjusting the model parameters, which are different for each wall. Since these models are based on a mixing length, a better knowledge of the momentum and heat exchange in variable molecular Prandtl number flows has to be deduced in order to improve turbulent Prandtl number models, instead of adjusting model parameters, which are not universal.

Declaration of Competing Interest

The authors declare that they have no known competing financial interests or personal relationships that could have appeared to influence the work reported in this paper.

Acknowledgments

The authors gratefully acknowledge the financial support provided by the German Research Foundation (Deutsche Forschungsgemeinschaft-DFG) within the framework of the Sonderforschungsbereich Transregio 40, SFB-TRR40 (Technological foundations for the design of thermally and mechanically highly loaded components of future space transportation systems). Computational resources have been provided by the Leibniz Supercomputing Centre Munich (LRZ). Furthermore, we would like to thank Christian Stemmer for the discussions during the review process.

Table A.3
Summary of grid parameters for TTCF.

	TCF_0	TCF_1	TCF_2
$N_x \times N_y \times N_z$	$48 \times 48 \times 48$	$96 \times 96 \times 96$	$192 \times 192 \times 192$
$L_x \times L_y \times L_z$	$2\pi H \times 2H \times \pi H$	$2\pi H \times 2H \times \pi H$	$2\pi H \times 2H \times \pi H$
Δx^+	65.5	38.2	20.3
Δz^+	32.7	19.1	10.1
$\Delta y^+_{\min} \times \Delta y^+_{\max}$	3.31×43.1	1.85×25.2	0.96×13.4

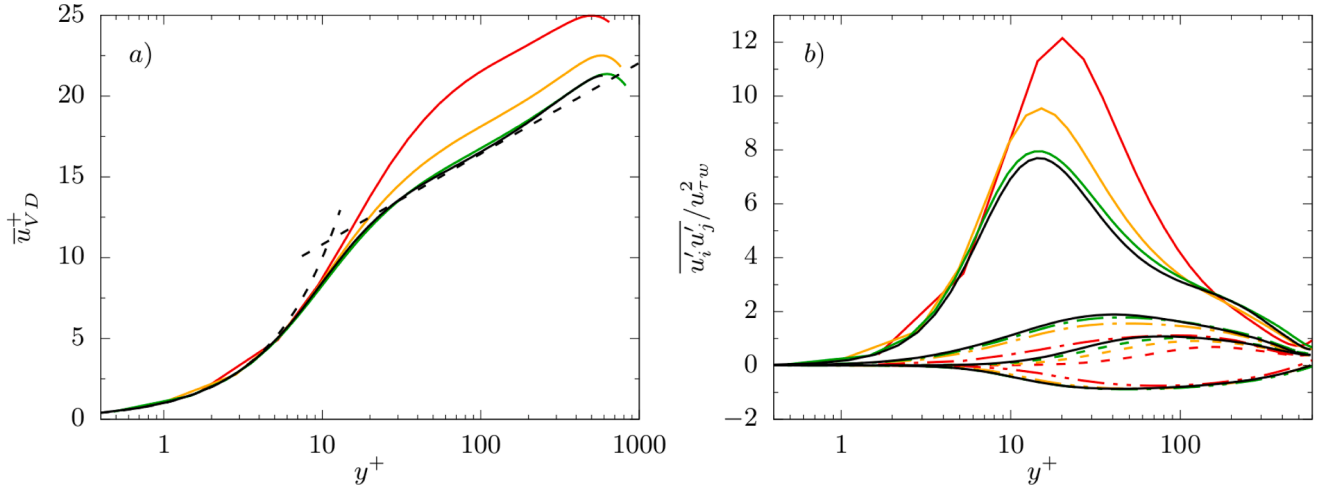


Fig. A.11. Mean velocity profiles using van Driest scaling and Reynolds stresses scaled with the friction velocity are plotted over wall units. The results for the respective grid level are indicated with red for TCF_0, orange for TCF_1 and green for TCF_2 including black for the DNS (Moser et al., 1999). Reynolds stresses $u' u' \text{---}$, $v' v' \text{- - - -}$, $w' w' \text{- - - -}$ and $u' v' \text{- - - -}$.

are presented in Fig. A.11(b) following the same trend as the mean velocity. With increasing grid resolution the peak of the streamwise Reynolds stress $u' u'$ is decreasing and moving towards the wall. A minor overprediction is observed in the buffer and logarithmic layer. The other stresses $v' v'$, $w' w'$ and $u' v'$ converge towards the DNS data with increasing resolution.

Appendix B. Semi-local scaling

In Fig. 7 the Favre average turbulent shear stress and turbulent heat flux from Eqs. 10 and 11 are scaled with semi-local values. The comparison between a scaling using semi-local values and wall properties is presented in Fig. B.12. The advantage of the semi-local scaling is observed especially at the cold where the pseudo-boiling is present. The Favre averaged turbulent shear stress collapses for TCF47 and TCF57 up to $y^* \approx 100$ whereas using wall properties leads to diverse profiles for the two simulations. At the hot wall both scaling laws achieve a good agreement between the two cases. Noticeable is the difference in magnitude obtained by the scaling laws at both wall. Regarding this, the semi-local adjusts the magnitude between both walls.

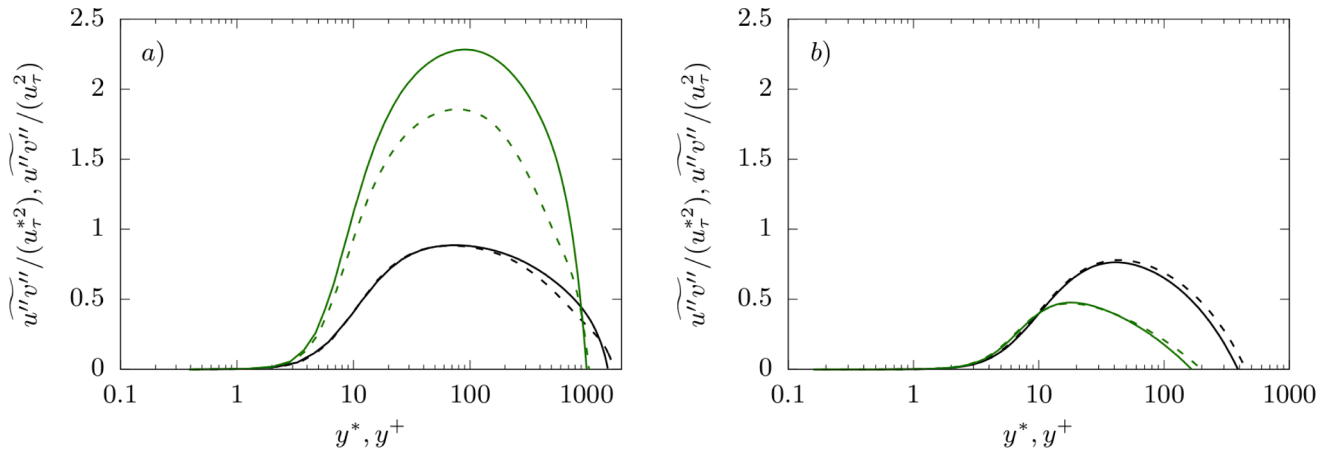


Fig. B.12. Favre averaged turbulent shear stress $\widetilde{u''v''}$ is shown at the cold wall (a) and the hot wall (b). Black lines indicate normalized profiles with semi-local values over semi-local wall units and green lines indicate normalized profiles using wall properties for Case TCF47 --- and TCF57 - - - .

Appendix C. Grid sensitivity study

A grid sensitivity study has been performed for case TCF47, since the bulk pressure is closer to the critical point resulting in stronger gradients. The domain extensions have not been changed and the bulk pressure of each level is between 4.75 bar and 4.81 bar. LvL3 is the resolution which has been used in the main text, see Table 1. The main parameters for the considered grids included in the sensitivity study are summarized in Table C.4.

In Fig. C.13 the van Driest transformed velocity profile is shown. It can be observed, that the velocity profile at both walls approaches the analytical logarithmic law. The velocity profile at the hot wall shows no difference between LvL2 and LvL3 indicating a converged solution. In contrast, no converged solution is not observed at the cold wall.

The Reynolds stresses normalized with the semi-local friction velocity are presented in Fig. C.14. At both walls the wall normal and spanwise velocity show minor differences between grid level LvL2 and LvL3 indicating a sufficient resolution for LvL3. For the streamwise direction the peak value is still adjusting for the finest grid level at the cold wall, whereas no difference is observed for the Reynolds stress profile uu at the hot wall.

The near wall temperature profile over the wall normal distance y^+ is depicted in Fig. C.15. A fitted linear function is included in blue and red for the cold and hot wall, respectively. Although, the thermal scales at the cold wall are slightly under-resolved still the temperature profile features a

Table C.4
Summary of grid parameters for the sensitivity study related to case TCF47.

	LvL0	LvL1	LvL2	LvL3
$N_x \times N_y \times N_z$	$48 \times 48 \times 48$	$96 \times 96 \times 96$	$128 \times 128 \times 128$	$192 \times 192 \times 192$
$L_x \times L_y \times L_z$			$2\pi H \times 2H \times \pi H$	
$\Delta x_{\text{cold}}^+ \times \Delta x_{\text{hot}}^+$	69×31	39×18	32×14	23×10
$\Delta z_{\text{cold}}^+ \times \Delta z_{\text{hot}}^+$	35×16	20×9	16×7	12×5
$\Delta y_{\text{min,cold}}^+ \times \Delta y_{\text{min,hot}}^+$	2.50×1.11	1.35×0.62	1.09×0.48	0.77×0.32
$\Delta y_{\text{max,cold}}^+ \times \Delta y_{\text{max,hot}}^+$	50.0×22.5	28.4×13.1	23.2×10.2	16.8×6.9

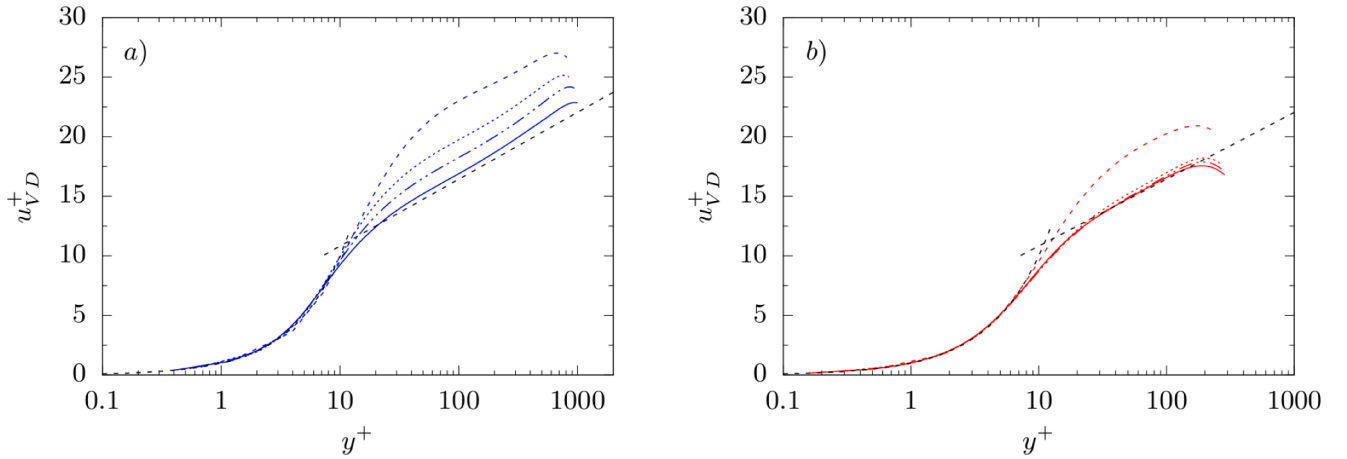


Fig. C.13. Van Driest normalized velocity profiles for case TCF47 at different grid levels: LvL0 ---, LvL1 ·····, LvL2 -·-·-, LvL3 ———. The viscous sublayer and the logarithmic law are indicated with black dashed lines based on the constants $B = 5.2$ and $\kappa = 0.41$. The cold and hot wall are presented in subfigure a) and b), respectively.

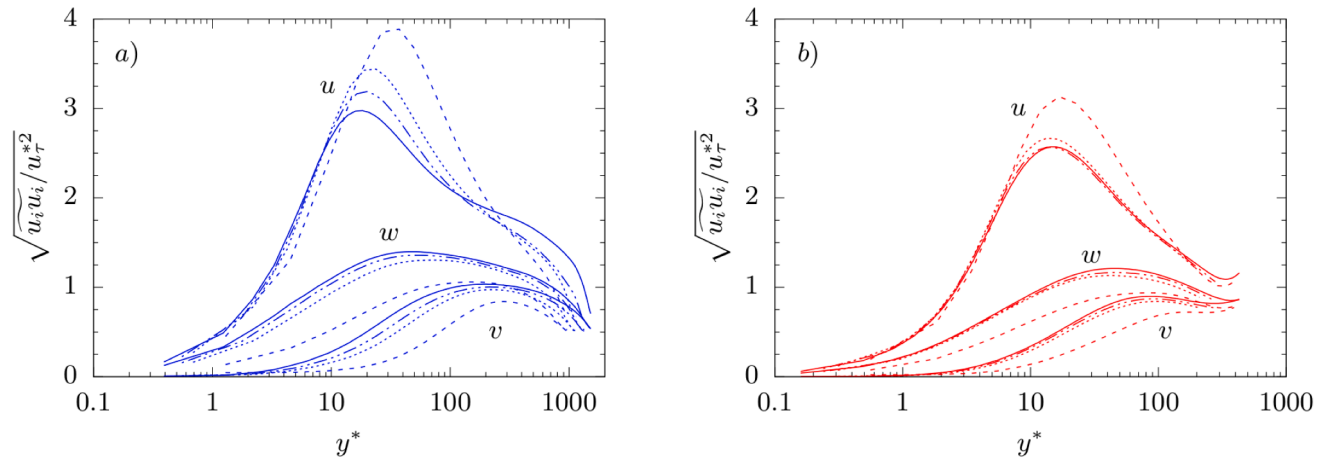


Fig. C.14. Reynolds stresses normalized with the semi-local friction velocity $u^* = \sqrt{\tau_w/\rho}$ for case TCF47 at different grid levels: LvL0 ---, LvL1 ·····, LvL2 -·-·-, LvL3 ———. The cold and hot wall are presented in subfigure a) and b), respectively.

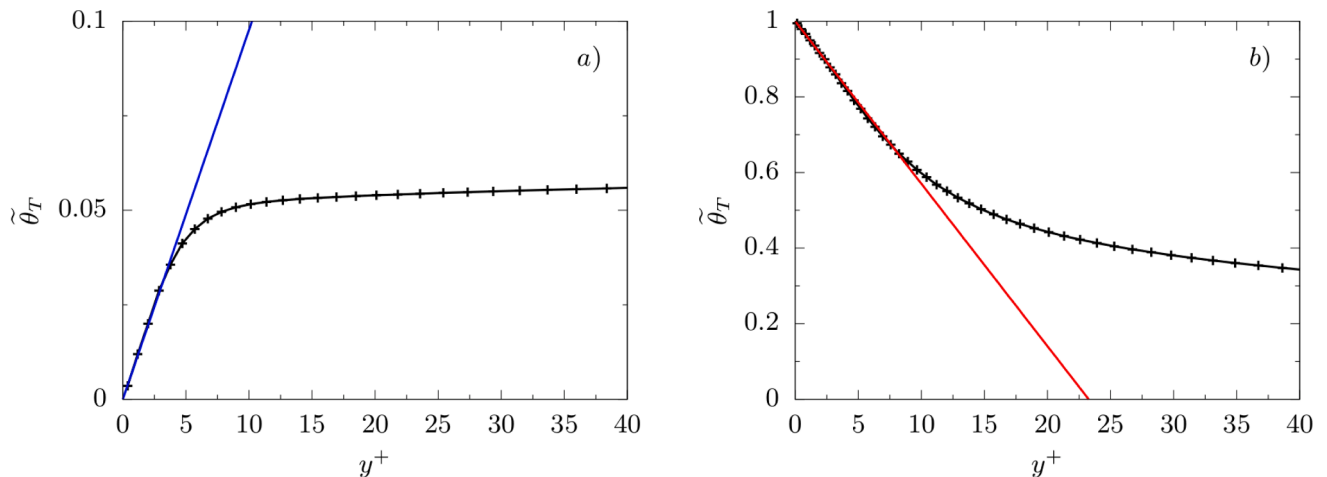


Fig. C.15. Scaled temperature profile $\tilde{\theta}_T$ at the cold wall (a) and hot wall (b) over the scaled wall normal distance y^+ . The blue and red line indicate a fitted linear function. The symbols in the temperature profile correspond to the cell center values.

linear distribution at the walls (viscous sublayer). From this, we conclude that the proposed ratio in Eq. 3 provides a reasonable estimation of the thermal scales.

References

- Antonia, R.A., Kim, J., 1991. Turbulent Prandtl number in the near-wall region of a turbulent channel flow. *International Journal of Heat and Mass Transfer* 34, 1905–1908.
- Bae, Y.Y., 2016. A new formulation of variable turbulent Prandtl number for heat transfer to supercritical fluids. *International Journal of Heat and Mass Transfer* 92, 792–806.
- Brun, C., Boiarciuc, M.P., Haberkorn, M., Comte, P., 2008. Large eddy simulation of compressible channel flow. *Theoretical and Computational Fluid Dynamics* 22, 189–212.
- Doehring, A., Schmidt, S.J., Adams, N.A., 2018. Numerical Investigation of Transcritical Turbulent Channel Flow, in: 2018 Joint Propulsion Conference.
- Egerer, C.P., Schmidt, S.J., Hickel, S., Adams, N.A., 2016. Efficient implicit LES method for the simulation of turbulent cavitating flows. *Journal of Computational Physics* 316, 453–469.
- Grifoll, J., Giralt, F., 2000. The near wall mixing length formulation revisited. *International Journal of Heat and Mass Transfer* 43, 3743–3746.
- Hickel, S., Adams, N.A., Domaradzki, J.A., 2006. An adaptive local deconvolution method for implicit LES. *Journal of Computational Physics* 213, 413–436.
- Hickel, S., Egerer, C.P., Larsson, J., 2014. Subgrid-scale modeling for implicit large eddy simulation of compressible flows and shock-turbulence interaction. *Physics of Fluids* 26.
- Huang, P.G., Coleman, G.N., Bradshaw, P., 1995. Compressible turbulent channel flows: DNS results and modelling. *Journal of Fluid Mechanics* 305, 185–218.
- Kaller, T., Pasquariello, V., Hickel, S., Adams, N.A., 2019. Turbulent flow through a high aspect ratio cooling duct with asymmetric wall heating. *Journal of Fluid Mechanics* 860, 258–299.
- Kawai, S., 2019. Heated transcritical and unheated non-transcritical turbulent boundary layers at supercritical pressures. *Journal of Fluid Mechanics* 865, 563–601.
- Kays, W.M., 1994. Turbulent Prandtl Number-Where Are We? *Journal of Heat Transfer* 116, 284–295.
- Kays, W.M., Crawford, M.E., 1993. *Convective Heat and Mass Transfer*, 3rd ed. McGraw-Hill Inc.
- Kim, J., Moin, P., Moser, R., 1987. Turbulence statistics in fully developed channel flow at low Reynolds number. *Journal of Fluid Mechanics* 177, 133–166.
- Kim, K., Hickey, J.P., Scalo, C., 2019. Pseudophase change effects in turbulent channel flow under transcritical temperature conditions. *Journal of Fluid Mechanics* 871, 52–91.
- Lee, J., Jung, S.Y., Sung, H.J., Zaki, T.A., 2013. Effect of wall heating on turbulent boundary layers with temperature-dependent viscosity. *Journal of Fluid Mechanics* 726, 196–225.
- Lemmon, E.W., Huber, M.L., McLinden, M.O., 2013. NIST Standard Reference Database 23: Reference Fluid Thermodynamic and Transport Properties-REFPROP, Version 9.1. National Institute of Standards and Technology.
- Ma, P.C., Yang, X.I.A., Ihme, M., 2018. Structure of wall-bounded flows at transcritical conditions. *Physical Review Fluids* 3 (3).
- Matheis, J., Hickel, S., 2018. Multi-component vapor-liquid equilibrium model for LES of high-pressure fuel injection and application to ECN Spray A. *International Journal of Multiphase Flow* 99, 294–311.
- Mayer, W., Tamura, H., 1996. Propellant Injection in a Liquid Oxygen/Gaseous Hydrogen Rocket Engine. *Journal of Propulsion and Power* 12, 1137–1147.
- Monin, A.S., Yaglom, A.M., 1975. *Statistical Fluid Mechanics: Mechanics of Turbulence*, vol. 2. MIT Press.
- Moser, R.D., Kim, J., Mansour, N.N., 1999. Direct numerical simulation of turbulent channel flow up to $Re_\tau = 590$. *Physics of Fluids* 11, 943–945.
- Patel, A., Boersma, B.J., Pecnik, R., 2016. The influence of near-wall density and viscosity gradients on turbulence in channel flows. *Journal of Fluid Mechanics* 809, 793–820.
- Pirozzoli, S., 2014. Revisiting the mixing-length hypothesis in the outer part of turbulent wall layers: mean flow and wall friction. *Journal of Fluid Mechanics* 745, 378–397.
- Prandtl, L., 1925. 7. Bericht über Untersuchungen zur ausgebildeten Turbulenz. *ZAMM - Journal of Applied Mathematics and Mechanics/Zeitschrift für Angewandte Mathematik und Mechanik* 5, 136–139.
- Schmidt, S.J., Sezal, I.H., Schnerr, G.H., 2006. Compressible simulation of high-speed hydrodynamics with phase change. In: *European Conference on Computational Fluid Dynamics*.
- Simeoni, G.G., Bryk, T., Gorelli, F.A., Krisch, M., Ruocco, G., M., S., T., S., 2010. The Widom line as the crossover between liquid-like and gas-like behaviour in supercritical fluids. *Nature Physics* 6, 503–507.
- Smits, A.J., Dussauge, J.P., 2006. *Turbulent Shear Layers in Supersonic Flow*, 2nd ed. Springer Science & Business Media Inc.
- Steiner, H., Irrenfried, C., 2019. Modelling of thermal wall boundary conditions with temperature-dependent material properties for use in RANS. *International Journal of Heat and Fluid Flow* 80, 108495.
- Trettel, A., Larsson, J., 2016. Mean velocity scaling for compressible wall turbulence with heat transfer. *Physics of Fluids* 28, 026102.
- Yoo, J.Y., 2013. *The Turbulent Flows of Supercritical Fluids with Heat Transfer*. Annual Review of Fluid Mechanics 45, 495–525.
- Zonta, F., Marchioli, C., Soldati, A., 2012. Modulation of turbulence in forced convection by temperature-dependent viscosity. *Journal of Fluid Mechanics* 697, 150–174.

**A.3. MOMENTUM BOUNDARY LAYERS IN
TRANSCRITICAL CHANNEL FLOWS**

A.3.1. RIGHTS AND PERMISSIONS:

Dear Alexander Doehring

We hereby grant you permission to reprint the material below at no charge in your thesis subject to the following conditions:

RE:

- **Large-eddy simulation of turbulent channel flow at transcritical states, International Journal of Heat and Fluid Flow, Volume 89, 2021, Doehring et al.**
- **Momentum boundary layers in transcritical channel flows, International Journal of Heat and Fluid Flow, Volume 103, 2023, Doehring et al.**

1. If any part of the material to be used (for example, figures) has appeared in our publication with credit or acknowledgment to another source, permission must also be sought from that source. If such permission is not obtained then that material may not be included in your publication/copies.

2. Suitable acknowledgment to the source must be made, either as a footnote or in a reference list at the end of your publication, as follows:

“This article was published in Publication title, Vol number, Author(s), Title of article, Page Nos, Copyright Elsevier (or appropriate Society name) (Year).”

3. Your thesis may be submitted to your institution in either print or electronic form.

4. Reproduction of this material is confined to the purpose for which permission is hereby given.

5. This permission is granted for non-exclusive world English rights only. For other languages please reapply separately for each one required. Permission excludes use in an electronic form other than submission. Should you have a specific electronic project in mind please reapply for permission.

6. As long as the article is embedded in your thesis, you can post/share your thesis in the University repository.

7. Should your thesis be published commercially, please reapply for permission.

8. Posting of the full article/ chapter online is not permitted. You may post an abstract with a link to the Elsevier website www.elsevier.com, or to the article on ScienceDirect if it is available on that platform.

Kind regards,

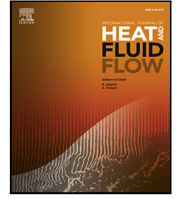
Roopa Lingayath

Senior Copyrights Specialist

ELSEVIER | HCM - Health Content Management

A. SELECTED PUBLICATIONS

A.3.2. MANUSCRIPT



Momentum boundary layers in transcritical channel flows

Alexander Doehring^{a,*}, Steffen J. Schmidt^a, Nikolaus A. Adams^{a,b}

^a Institute of Aerodynamics and Fluid Mechanics, Department Engineering Physics and Computation, Technical University of Munich, Boltzmannstr. 15, 85748 Garching, Germany

^b Munich Institute of Integrated Materials, Energy and Process Engineering, Technical University of Munich, Lichtenbergstr. 4a, 85748 Garching, Germany

ARTICLE INFO

Keywords:

LES
Channel flow
Transcritical
Turbulent mass flux
Anisotropy

ABSTRACT

We present well-resolved large-eddy simulations (LES) of a channel flow solving the fully compressible Navier–Stokes equations in conservative form. An adaptive look-up table method is used for thermodynamic and transport properties. We apply a physically consistent subgrid-scale turbulence model, that is based on the Adaptive Local Deconvolution Method (ALDM) for implicit LES. The wall temperatures are set to enclose the pseudo-boiling temperature at a supercritical pressure, leading to strong property variations within the channel geometry. In total seven cases are computed covering different Reynolds numbers, pseudo-boiling positions and pressure values. The hot wall at the top and the cold wall at the bottom produce asymmetric mean velocity and temperature profiles which result in different momentum layer thicknesses. All cases feature a turbulent mass flux which is essential in turbulence modelling. Furthermore, we analyse the turbulent kinetic energy budgets, perform a quadrant and octant analysis of the Reynolds shear stress and employ an invariant map to study the anisotropy in transcritical turbulent channel flows.

1. Introduction

Transcritical fluids, where the pressure is above the critical values, but the temperature ranges from sub- to supercritical, are widely used in many engineering applications. As for example in diesel engines (Wensing et al., 2016; Crua et al., 2017), gas turbines (Kim et al., 2017; Hosseinpour et al., 2022), supercritical water-cooled reactors (SCWRs) (Cheng et al., 2007) and liquid rocket engines (LRE) (Müller et al., 2016; Matheis and Hickel, 2018). These fluids are characterized by a gas-like diffusivity, a liquid-like density and a surface tension approaching zero, leading to a diffuse mixing. The latter can be observed in the experimental study with cryogenic jets of Mayer and Tamura (1996). At supercritical pressure the fluid in the experiments forms finger-like entities with a continuous phase transition instead of droplet formation. Studies performed by Simeoni et al. (2010) disagree with a continuous phase transition, but have shown a supercritical liquid-like (LL) and gas-like (GL) region with a pseudo-boiling line (PBL), which extends the classical liquid–vapour-coexistence line. In the vicinity of the PBL, strong non-linear property variations are observed, due to intermolecular repulsive forces.

Reynolds-averaged Navier–Stokes simulations (RANS) based on established turbulence models fail to predict the correct heat transfer and shear forces (Yoo, 2013; Kaller et al., 2020). Effects like heat transfer enhancement as well as the onset of heat transfer deterioration in

transcritical and supercritical flows cannot be captured correctly (Pizzarelli, 2018). In a review paper by Yoo (2013) various experimental and numerical studies are summarized. Only few experimental studies have been carried out due to technical difficulties which are present at high pressure conditions. As a result, experimental data on turbulent statistics and heat transfer, suitable for the development of reliable turbulence models, are scarce. For this reason, high fidelity numerical data is required to understand the effect of non-linear thermodynamics on turbulent flows in order to improve computationally efficient turbulence models.

In this context multiple numerical studies have been performed. Ma et al. (2018) has investigated a Direct numerical simulation (DNS) of a transcritical channel flow using an entropy-stable double-flux model in order to avoid spurious pressure oscillations (Terashima and Koshi, 2012). Since the flux calculation is non-conservative, they provided a comparison of the thermodynamic properties with a fully conservative formulation. Differences are visible at the hot wall, where the temperature is above the pseudo-boiling temperature. This discrepancy is attributed to the energy conservation which is not satisfied. In addition, they observed the presence of a logarithmic scaling of the structure function and a k^{-1} scaling of the energy spectra, which supports the attached-eddy hypothesis in transcritical flows. Matheis and Hickel (2018) included a comparison between a fully conservative (FC) and a

* Corresponding author.

E-mail address: alex.doehring@tum.de (A. Doehring).

quasi conservative (QC) formulation by replacing the energy equation with a pressure evolution equation (Terashima and Koshi, 2012). The numerical 1-D advection-diffusion test case of a contact discontinuity has shown, that for a coarse grid the QC formulation omits pressure fluctuations, but introduces an error in the temperature distribution. With increasing grid resolution, spurious oscillations of the FC method are decreasing and the error in the temperature profile of the QC method reduces towards the FC solution. A heated transcritical turbulent boundary layer over a flat plate has been investigated by Kawai (2019) using DNS. His study shows large density fluctuations which are induced by strong changes of thermodynamic properties in the vicinity of the pseudo-boiling. Furthermore, these fluctuations evoke non-negligible Favre-averaged velocity fluctuations, which are associated with a turbulent mass flux. In addition, velocity transformations such as the van Driest transformation, the semi-local scaling by Huang et al. (1995) and the transformation by Trettel and Larsson (2016) have failed in transcritical boundary layers. This has also been ascertained by Ma et al. (2018). Kim et al. (2019) controlled the pseudo-boiling position by changing the temperature difference between the walls in a DNS of a turbulent channel flow. Large streamwise turbulent structures based on Q-criterion isosurfaces have been identified close to the walls. This leads to the necessity of larger computational domains, thus, higher numerical costs for the study of transcritical channel flows. Despite the reduction of turbulent intensity at the hot wall, they observed intensified thermodynamic fluctuations and strong ejections of dense fluids into the channel core. A DNS study by Chen et al. (2021) of a turbulent channel has been performed using a dense gas in the framework of ORC systems. They identified an increase of the wall normal and spanwise Reynolds shear stress component compared to a turbulent channel flow with an ideal gas. The turbulent energy transport and scaling laws in transcritical channel flows using DNS have been investigated by Li et al. (2023). They observed local equilibrium of turbulent kinetic energy transport in transcritical flows in the logarithmic layer.

Despite the various studies mentioned above, it is still not entirely clear how the variable thermophysical properties of a heated or cooled fluid at supercritical pressure affect turbulent motions. This is due to the fact that we are dealing with a multiphysics problem in which non-linear thermodynamics, turbulent flow and heat transfer interact with each other. The lack of understanding of such systems can be demonstrated by the poor turbulence models in RANS (see Yoo (2013)) and the large number of proposed mean velocity transformations to fit the incompressible mean velocity profiles (see Trettel and Larsson (2016), Volpiani et al. (2020), Griffin et al. (2021), Bai et al. (2022).)

In this study, we investigate a momentum boundary layer affected by strong property variations in transcritical channel flows. The first prominent feature of this study is the location of pseudo-boiling. The temperature of the channel walls is adjusted so that pseudo-boiling will occur. By adjusting the wall temperature, the pseudo-boiling is located either at the cold wall, in the centre of the channel, or at the hot wall. Second, unlike the aforementioned studies, we use well-resolved large-eddy simulations (LES). This allows us to qualitatively compare the results with DNS results and thus, implicitly evaluate the modelling at the subgrid scale. In addition, LES allows us to investigate higher Reynolds numbers compared to the aforementioned DNS studies. Finally, two different bulk pressure levels are used to vary the distance to the critical point and thus, the intensity of non-linear effects.

The goal of this study is to provide statistical data that will contribute to the understanding of turbulence and to use the data to develop low-cost CFD models, such as wall-modelled LES. The study comprises obtained mean distributions, law of the wall for the velocity, Reynolds stresses, turbulent mass flux, turbulent kinetic energy budgets, a quadrant and an octant analysis of the Reynolds shear stresses and an invariant map to visualize the anisotropy distribution.

2. Numerical model

The three-dimensional compressible Navier–Stokes equations are solved for the performed LES.

$$\frac{\partial \rho}{\partial t} + \frac{\partial \rho u_j}{\partial x_j} = 0 \quad (1)$$

$$\frac{\partial \rho u_i}{\partial t} + \frac{\partial \rho u_i u_j}{\partial x_j} = -\frac{\partial p}{\partial x_i} + \frac{\partial \tau_{ij}}{\partial x_j} + f_i \quad (2)$$

$$\frac{\partial \rho E}{\partial t} + \frac{\partial (\rho E u_j + p u_j)}{\partial x_j} = \frac{\partial (u_i \tau_{ij} - q_i)}{\partial x_j} + u_i f_i \quad (3)$$

The density is denoted by ρ , the pressure by p , the velocity in the i -th direction by u_i . In order to maintain a constant mass flux in the streamwise direction, a body force $f_i = f \delta_{i1}$ is introduced in the momentum and energy equations based on Brun et al. (2008). The total energy E consists of the internal energy e and the kinetic energy,

$$\rho E = \rho e + 1/2 \rho u_i u_i. \quad (4)$$

The viscous stress tensor τ_{ij} and the strain rate tensor S_{ij} for a Newtonian fluid are defined according to Stoke's hypothesis

$$\tau_{ij} = \mu \left(2 S_{ij} - \frac{2}{3} \delta_{ij} S_{kk} \right), \quad (5)$$

$$S_{ij} = \frac{1}{2} \left(\frac{\partial u_i}{\partial x_j} + \frac{\partial u_j}{\partial x_i} \right), \quad (6)$$

with the dynamic viscosity μ . The Kronecker-Delta function δ_{ij} is unity if $i = j$ and zero otherwise. The heat flux q_i is defined using Fourier's law of thermal conductivity

$$q_i = -\lambda \partial T / \partial x_i, \quad (7)$$

where λ is the thermal conductivity and T is the temperature. A finite-volume method is applied in order to spatially discretize the conservative form of the governing equations on a block structured, curvilinear grid. An explicit second-order low-storage four-stage Runge–Kutta method with enhanced stability region is applied for time advancement developed by Schmidt et al. (2006). The compact four cell stencil approach by Egerer et al. (2016) is used to compute the convective fluxes. Thermodynamic and transport properties are extracted from the tabulated look-up database via trilinear interpolation. Additional information about the tabulated database are provided in Appendix C. A discontinuity detecting sensor functional switches the flux calculation between a linear fourth-order reconstruction for high accuracy and a more stable upwind-biased scheme. The discontinuity-detector sensor used is based on Ducros et al. (1999)

$$\Phi = \frac{|\nabla \cdot \mathbf{u}|}{|\nabla \cdot \mathbf{u}| + \|\nabla \times \mathbf{u}\| + \epsilon}, \quad (8)$$

with $\epsilon = 10^{-15}$. The sensor is switched on, if the threshold value of 0.95 is exceeded,

$$s = \begin{cases} 1, & \Phi \geq 0.95 \\ 0, & \Phi < 0.95. \end{cases} \quad (9)$$

In the simulations the sensor is active on 0.002% of the total volume. A physically consistent subgrid-scale turbulence model based on the Adaptive Local Deconvolution Method (ALDM) (Hickel et al., 2006, 2014) is included in the convective flux calculation. Viscous fluxes are determined by a linear second-order centred scheme. The ALDM subgrid-scale model has been previously investigated in the context of trans- and supercritical flows by Matheis and Hickel (2018).

Thermodynamic and transport properties are obtained using an adaptive look-up table method based on the REFPROP database (Lemmon et al., 2013). One table is generated for the fluid domain imposing density and internal energy constraints and a second table is used for the boundary conditions imposing pressure and temperature constraints.

Table 1
Summary of considered cases.








	TCF55B	TCF65B	TCF55BR	TCF55M	TCF65M	TCF55MR	TCF60TR
	()	()	()	()	()	()	()
p_b	54.2 bar	66.2 bar	52.2 bar	54.1 bar	64.8 bar	54.0 bar	60.8 bar
Re	10040	10000	20120	10020	10005	20040	20006
T_c	185 K	185 K	185 K	180 K	180 K	180 K	155 K
T_h	285 K	285 K	285 K	280 K	280 K	280 K	255 K

Table 2
Grid resolution based on viscous and thermal scales.

Cold Wall	TCF55B	TCF65B	TCF55BR	TCF55M	TCF65M	TCF55MR	TCF60TR
Δx_c^+	21.02	21.04	38.24	20.07	20.10	36.50	32.04
Δz_c^+	7.00	7.01	12.75	6.69	6.70	12.17	10.68
$\Delta y_{\min,c}^+$	0.35	0.35	0.64	0.34	0.34	0.61	0.54
$\Delta y_{\max,c}^+$	7.64	7.64	13.89	7.29	7.30	13.25	11.64
$\Delta y_{T,\min,c}^+$	0.51	0.49	0.96	0.47	0.46	0.85	0.70
$\Delta y_{T,\max,c}^+$	11.21	10.70	20.86	10.12	9.86	18.37	15.08
Hot Wall	TCF55B	TCF65B	TCF55BR	TCF55M	TCF65M	TCF55MR	TCF60TR
Δx_h^+	14.72	16.77	26.80	15.08	17.32	27.96	42.52
Δz_h^+	4.91	5.59	8.93	5.03	5.77	9.32	14.17
$\Delta y_{\min,h}^+$	0.25	0.28	0.45	0.25	0.29	0.47	0.71
$\Delta y_{\max,h}^+$	5.35	6.09	9.73	5.47	6.29	10.16	15.44
$\Delta y_{T,\min,h}^+$	0.23	0.26	0.42	0.23	0.27	0.44	0.68
$\Delta y_{T,\max,h}^+$	4.96	5.67	9.02	5.13	5.92	9.52	14.85

3. Setup

A generic channel flow configuration is used to focus on the impact of non-linear thermodynamic effects on turbulent flows and the momentum boundary layer. The channel geometry is presented in Fig. 1. The size of the domain is $4\pi H \times 2H \times 4/3\pi H$ in the streamwise, wall-normal and spanwise direction, respectively. H refers to the channel half-height. The domain in this study is larger than in the previous study (Doehring et al., 2021) in order to ensure a decorrelated flow in the streamwise direction, since Kim et al. (2019) identified larger streamwise structures. The chosen size of the channel is supported by the autocorrelation function in Appendix D.

Periodic boundary conditions are imposed in stream- and spanwise direction x and z . Isothermal no slip boundary conditions are applied at the top and bottom wall. The wall temperatures are set to include pseudo-boiling.

Methane is used as working fluid with its critical pressure of $p_{cr} = 4.5992$ MPa at a critical temperature of $T_{cr} = 190.564$ K. The subscript w refers to values at the wall, b to bulk parameters, cr to critical values, pb to values obtained at the pseudo-boiling position, c to values at the cold wall and h to values at the hot wall.

Seven LES simulations have been performed with different bulk pressure levels, Reynolds numbers and wall temperatures. A desired bulk pressure p_b is obtained by adjusting the bulk density, which is similar to the method by Kim et al. (2019). The intention of various p_b is to create cases with a certain distance to the critical point in order to capture different intensities of non-linear thermodynamic behaviour.

In total two pressure levels are considered. The first $p_b \approx 55$ bar with a reduced pressure of $p_b/p_{cr} \approx 1.2$ and the second $p_b \approx 65$ bar with a reduced pressure of $p_b/p_{cr} \approx 1.4$. For most cases a bulk Reynolds number of $Re_b = u_b \rho_b H / \mu_b \approx 10000$ is set. In order to observe potential Reynolds number effects some cases have been performed with an increased Reynolds number of $Re_b \approx 20000$. In our previous study (Doehring et al., 2021) the heat capacity peak was located very close to the cold wall. Now, we adjusted the temperatures to alter the position, which includes an altered c_p located approximately at the cold wall, the hot wall and the channel centre. The temperature difference between the walls is kept constant at $T_{w,h} - T_{w,c} = 100$ K. The naming convention for the performed turbulent channel flow simulations (TCF) are based on the obtained bulk pressure, the position of the heat capacity peak (bottom \rightarrow B, middle \rightarrow M, top \rightarrow T) and the bulk

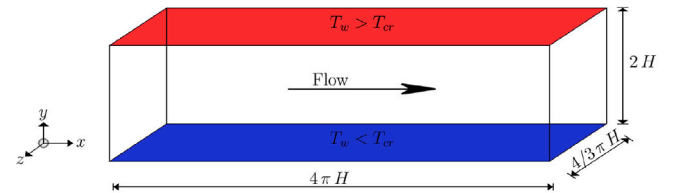


Fig. 1. Computational domain with a hot wall above and a cold wall below the critical temperature at supercritical pressure. H refers to the channel half height.

Reynolds number (increased $Re \rightarrow R$). For instance, TCF55BR refers to a bulk pressure of approximately 55 bar with a heat capacity peak located at the bottom wall and an increased Reynolds number of $Re \approx 20000$. All seven LES simulations are summarized in Table 1 including the name, bulk pressure, Reynolds number, wall temperatures and line styles for the upcoming figures.

We use a hyperbolically stretched grid in the wall-normal direction y and a uniform grid spacing in the stream- and spanwise direction. The domain is discretized with 256 cells in each direction, which is finer than in the previous study (Doehring et al., 2021). The same grid has been used for all performed LES simulations. A grid study is included in Appendix A.

Table 2 includes the resolution for all simulations. The resolution with respect to wall units $\Delta x^+ = \Delta x \rho_w u_\tau / \mu_w$ is based on the friction velocity $u_\tau^2 = (\tau_w / \rho_w)$ and the wall shear stress $\tau_w = (\mu \partial u / \partial y)|_w$. Note, that the resolution is based on the whole cell size, but the flow variables are evaluated at the cell centre. In order to estimate the mesh resolution in terms of thermal scales we employ the ratio between the Batchelor scales η_B and the Kolmogorov scales η introduced by Monin and Yaglom (1975). This ratio has been used in context of heated transcritical and ideal gas boundary layers by Zonta et al. (2012a), Lee et al. (2013), Ma et al. (2018), Kaller et al. (2019), Kawai (2019). This relation was adopted for LES by assuming proportionality between the thermal and viscous scales including the molecular Prandtl number, cf. Doehring et al. (2021). Since the molecular Prandtl number is partly greater than one in our LES simulations, implies, that the thermal scales are also smaller than the viscous scales. In this context, Ma et al. (2018) reported that the grid resolution is governed by the thermal scales and not the viscous scales due to a varying molecular Prandtl number,

Table 3

Summary of friction Reynolds numbers for all cases. The percentage relates to the TCF55 cases, respectively.

Re_τ	TCF55B	TCF65B	TCF55BR	TCF55M	TCF65M	TCF55MR	TCF60TR
cold wall	428.27	428.67 (+0.1%)	779.10 (+82%)	408.95	409.56 (+0.15%)	743.48 (+82%)	652.80
hot wall	299.92	341.66 (+14%)	545.93 (+82%)	307.26	352.84 (+15%)	569.64 (+85%)	866.28
$Re_{\tau,c}/Re_{\tau,h}$	1.43	1.25	1.43	1.33	1.16	1.30	0.75

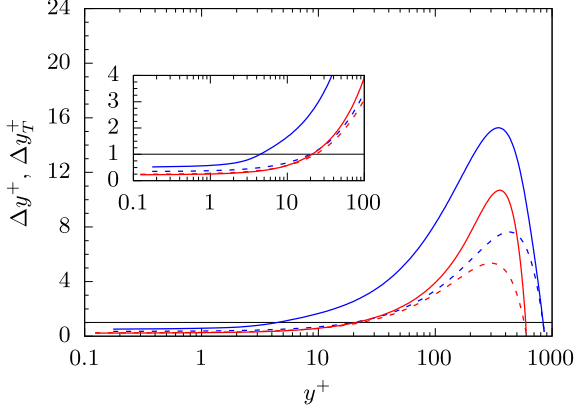


Fig. 2. Wall-normal cell sizes based on the viscous length scale l^+ (---) and thermal length scale $l_T^+ = l^+ / \sqrt{Pr}$ (—) for case TCF55B over the dimensionless wall distance y^+ . The cold wall resolution is shown in blue and the hot wall resolution in red. A zoomed in figure is included showing the vicinity of the wall. The thin solid black line indicates $\Delta y^+ = 1$ and $\Delta y_T^+ = 1$, respectively.

shown in Fig. 2. The thermal scales are relevant at the cold wall and the viscous scales at the hot wall regarding the resolution requirements. Roughness and gravity are not considered in the simulations in order to focus on non-linear thermodynamics. But, both are able to modify the momentum and heat transfer, thus, influencing the pressure drop and heat transfer, see for instance (Zonta et al., 2012b; Zonta and Soldati, 2018; Nemati et al., 2015; Peeters et al., 2016; Peeters and Sandham, 2019).

The obtained local Mach number is below 0.3 for all cases. From the mean turbulent Mach number

$$\overline{Ma}_t = \sqrt{\overline{u_i' u_i'}} / \bar{c}, \quad (10)$$

presented in Fig. 3(a), we do not expect compressible effects due to mean density variations, since $\overline{Ma}_t < 0.3$.

The semi-local Reynolds number Re_τ^* distribution is similar for all cases increasing with wall distance, see Fig. 3(b). This corresponds to the liquid-like profiles in the study by Patel et al. (2016). The values at the wall are summarized in Table 3. Except for case TCF60TR, all cases have a higher friction Reynolds number at the cold wall. Doubling the Reynolds number increases Re_τ by about 82% at both walls. Despite the non-linearity of the thermodynamics, the friction Reynolds number ratio between the cold and hot wall is kept approximately the same, when the Reynolds number is increased. Compare $Re_{\tau,c}/Re_{\tau,h}$ of case TCF55B and TCF55BR, and case TCF55M and TCF55MR. A change in the pressure affects only the hot wall leading to an increase of about 15%.

The deviation from the ideal gas law is demonstrated by the compressibility factor $Z = p/(\rho T R_{CH_4})$ in Fig. 3(c). In the vicinity of the cold wall the compressibility factor ranges from 0.19 to 0.24 which is far from an ideal gas behaviour. With increasing temperature also Z increases to values between 0.8 and 0.9. Thus, we obtain also a non-ideal gas behaviour at the hot wall. In contrast, the previous study (Doehring et al., 2021) exhibited nearly ideal gas behaviour with $Z = 0.98$ at the hot wall due to a higher temperature $T_{w,h}$. TCF60TR has a nearly constant compressibility factor at the lower channel half with a steep increase at the hot wall, which stands out in contrast to the other cases.

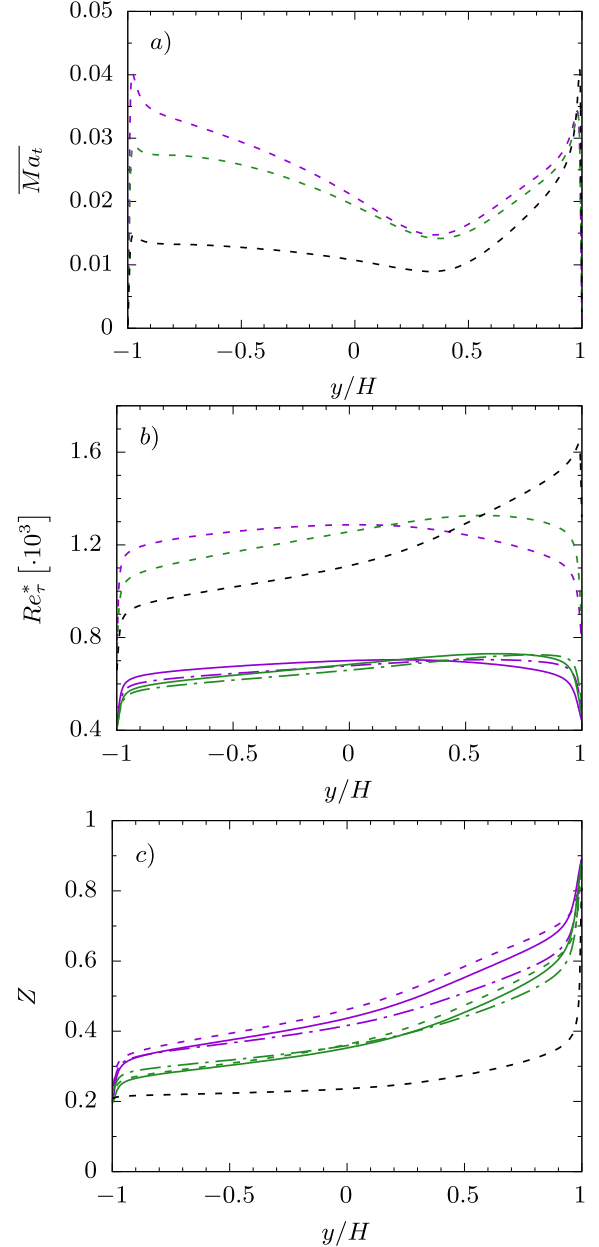


Fig. 3. Turbulent Mach number \overline{Ma}_t for cases with an increased Reynolds number (a). Semi-local friction Reynolds number in (b) and compressibility factor in (c). All profiles are shown over the normalized channel height, where the cold wall is located at $y/H = -1$ and the hot wall at $y/H = 1$. Cases: TCF55B (—), TCF65B (---), TCF55BR (---), TCF55M (—), TCF65M (· · · · ·), TCF55MR (---), TCF60TR (---). (For interpretation of the references to colour in this figure legend, the reader is referred to the web version of this article.)

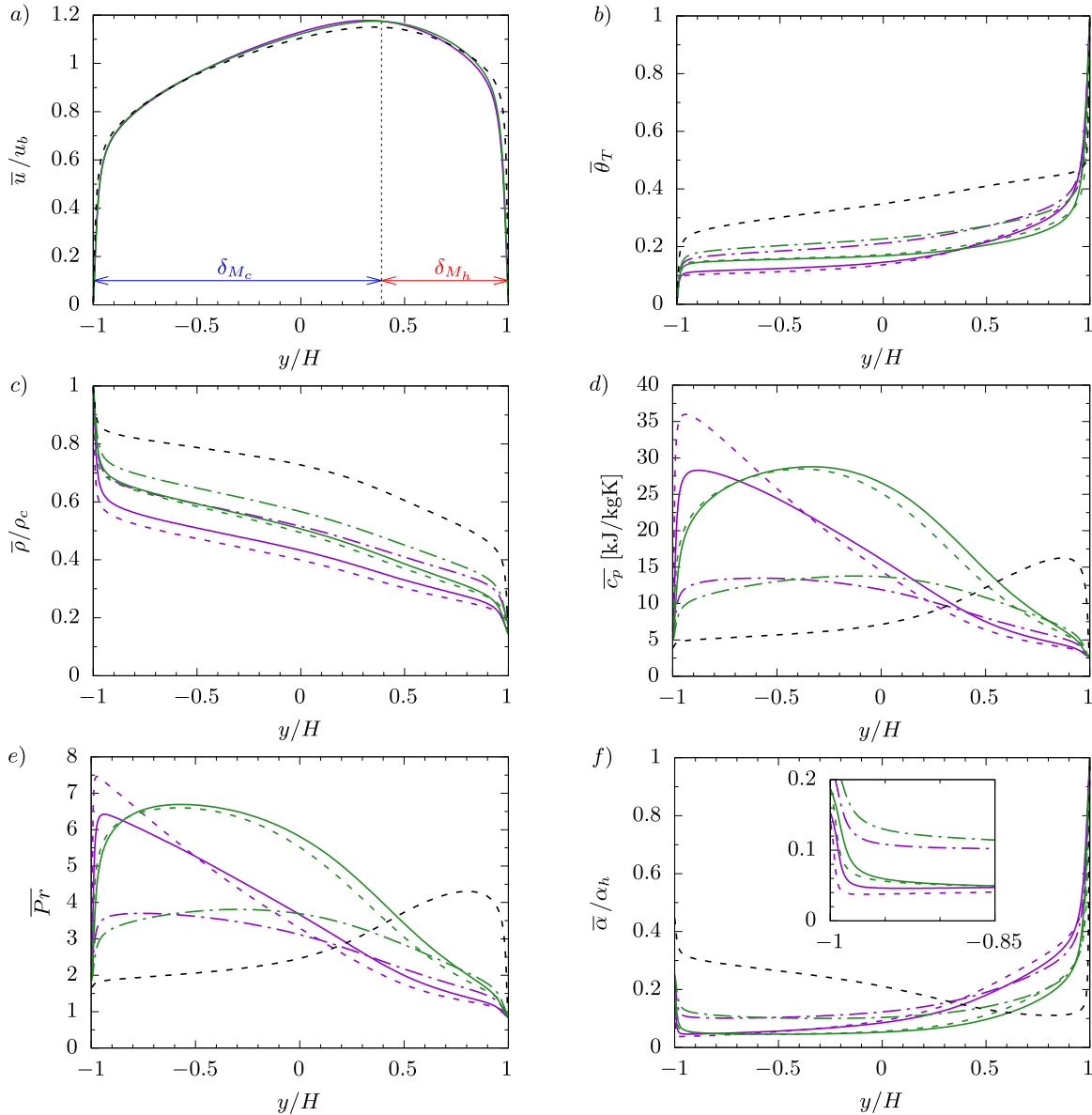


Fig. 4. Mean profiles are depicted over the channel height. The velocity (a) is normalized with the bulk value and the temperature profiles with the wall values $\theta_T = (T - T_{w,c})/(T_{w,h} - T_{w,c})$. The density (c) is scaled with the cold wall value ρ_c and the specific heat capacity is shown in (d). Mean Prandtl number $\bar{Pr} = \bar{\mu}c_p/\bar{\lambda}$ (e) and thermal diffusivity $\bar{\alpha} = \bar{\lambda}/(\bar{\rho}c_p)$ (f). Cases: TCF55B (—), TCF65B (---), TCF55BR (···), TCF55M (—), TCF65M (---), TCF55MR (···), TCF60TR (-·-·-).

4. Results

In the following, the mean flow properties are analysed by averaging in time and subsequently in streamwise and spanwise direction after reaching a quasi-stationary state. The Favre average is defined using a tilde as $\tilde{\phi} = \overline{\rho\phi}/\bar{\rho}$ and the Reynolds average is an ensemble average denoted with an overline $\bar{\phi}$. The fluctuations are represented as double prime ϕ'' or single prime ϕ' with respect to Favre and Reynolds averages, respectively. The least amount of samples used for the averaging process are 17,000 over a period of at least 13 flow-through times. For further information about averaging techniques in the context of strongly correlated fluid variables we refer to Huang et al. (1995) and Smits and Dussauge (2006).

4.1. Mean distribution

The Reynolds averaged velocity and temperature profiles are shown in Fig. 4(a) and (b). The velocity is normalized with the bulk velocity u_b

and shows a shift towards the hot wall due to thermal expansion (Ma et al., 2018; Kim et al., 2019; Doehring et al., 2021). Only marginal effects of the pseudo-boiling and the Reynolds number variation are observed for the mean velocity. For this reason only three cases are depicted. The momentum boundary layer is determined by the locus of zero total shear stress $\tau_T = 0$, resulting in a thicker boundary layer at the cold wall than at the hot wall $\delta_{M_c} > \delta_{M_h}$. The momentum thicknesses in Fig. 4(a) correspond to case TCF60TR.

The temperature is scaled using the wall temperatures $\theta_T = (T - T_{w,c})/(T_{w,h} - T_{w,c})$. High gradients are located in the vicinity of the walls. In general, a higher bulk density or equally a higher bulk pressure results in a higher bulk temperature, thus, an increased temperature level. No effect of the Reynolds number can be observed using the outer scale. The slight difference between case TCF55B and TCF55BR comes from the bulk pressure difference of approximately 2 bar. The pressure difference between case TCF55M with TCF55MR is smaller resulting in nearly overlapping temperature profiles. A flattening is present for all

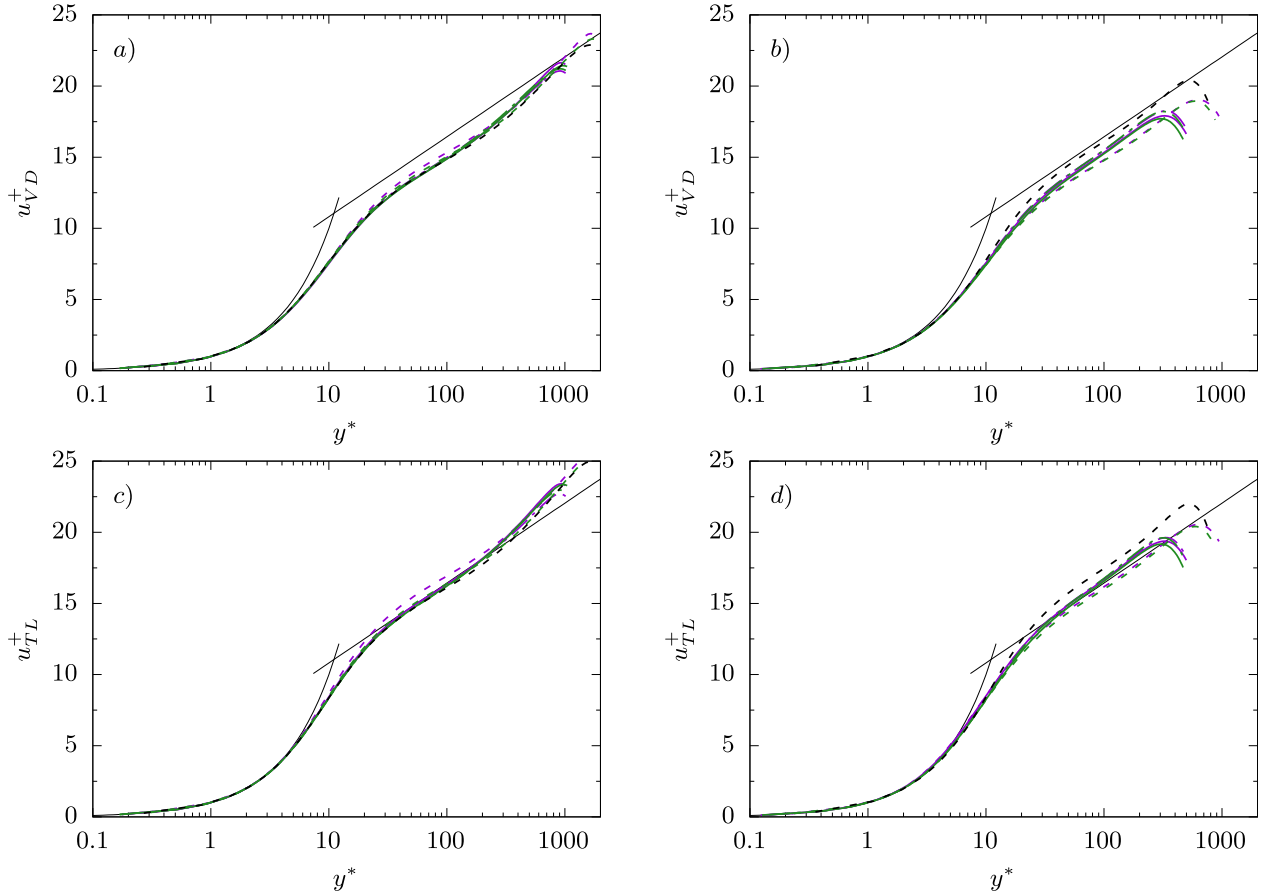


Fig. 5. Mean velocity profiles using the van Driest scaling (van Driest, 1956) (a,b) and the Trettel and Larsson transformation (Trettel and Larsson, 2016) (c,d) over the semi-local channel height. The cold wall is shown on the left and the hot wall on the right. The linear viscous sublayer is included together with the logarithmic layer based on the Kármán constant $\kappa = 0.41$ and the intercept $B = 5.2$ with a thin black line. Cases: TCF55B (—), TCF65B (---), TCF55BR (---), TCF55M (—), TCF65M (---), TCF55MR (---), TCF60TR (---). (For interpretation of the references to colour in this figure legend, the reader is referred to the web version of this article.)

cases except for TCF60TR, where the profile exhibit a linear increase for most of the channel with a sudden rise close to the hot wall.

Fig. 4(c) and (d) show the mean density scaled with the wall values and the specific heat capacity at constant pressure. Focusing on the configurations ‘bottom’ (pink) and ‘middle’ (green), a higher pressure results in an elevated density distribution, thus, a higher bulk density. A smaller density drop is obtained for TCF60TR at the cold wall compared to the other cases. The opposite appears at the hot wall. A heat capacity peak is present for case TCF55B, TCF55BR, TCF60TR. All three TCFM (green) cases do not have a distinct peak, but rather an increased c_p value for the most part of the channel. With an increased pressure and a larger distance from the critical point the c_p distribution flattens. The difference between TCF55B and TCF55BR is again not a Reynolds number effect, but rather arises due to the pressure difference of 2 bar. This conclusion follows from the observation of TCF55M and TCF55MR, where the pressure is nearly the same, which can be also observed in the mean profiles. Since the heat capacity acts like a heat sink, it explains the flattening of the temperature in Fig. 4(b). Cases TCFB flatten the temperature close to the cold wall. The c_p increase for cases TCFM spreads over a bigger distance in the channel, leading to a delayed rise of the temperature moving from the cold to the hot wall. For latter analysis we determine the pseudo-boiling position by means of the maximum heat capacity value $y_{pb} = c_{p,max}$.

Due to strong property variations the mean Prandtl number $\overline{Pr} = \overline{\mu c_p} / \overline{\lambda}$ varies over the channel height from 0.85 to 7.5. The Prandtl number distribution follows the c_p distribution and the highest values are observed at the pseudo-boiling position, where the momentum

diffusivity is dominating and thermal diffusivity $\overline{\alpha} = \overline{\lambda} / (\overline{\rho c_p})$ reaches a minimum, see Fig. 4(e) and (f).

The conventional log-law for the velocity holds for incompressible flows without heating. Several velocity transformations have been proposed, which consider compressibility effects in order to match the incompressible profiles. One transformation was introduced by van Driest (1956), taking mean density variations into account (VD). Trettel and Larsson (2016) deduced a transformation for non-adiabatic flows by including the local density and viscosity gradient (TL). In Fig. 5 the van Driest, and Larsson and Trettel scaling laws are applied including the linear viscous sublayer and the logarithmic layer with the Kármán constant $\kappa = 0.41$ and the intercept $B = 5.2$. These scaling laws are able to collapse the velocity profiles fairly well at the cold wall. It can be seen, that the intercept is underestimated by the velocity profiles using VD, whereas TL moves the profiles on the incompressible law of the wall.

Patel et al. (2016) observed that a positive gradient of the semi-local Reynolds number leads to a downwards shift using the VD transformation. The opposite is the case for a negative gradient. As it can be seen in Fig. 3(b) the gradient is positive for all simulations regarding the cold wall, which leads to the mentioned downward shift in Fig. 5(a). At the hot wall the spreading of the velocity profiles is wider using VD, and the TL transformation does not reduce the spread. We attribute this to the slope change of the semi-local Reynolds number at different wall normal distances from the hot wall. The van Driest transformed velocity profile is presented using the indicator function $\Xi_{VD} = y^* du_{VD}^+ / dy^*$ in Fig. 6. This function is used to identify the logarithmic layer through the development of a plateau. A variety of numerical and experimental

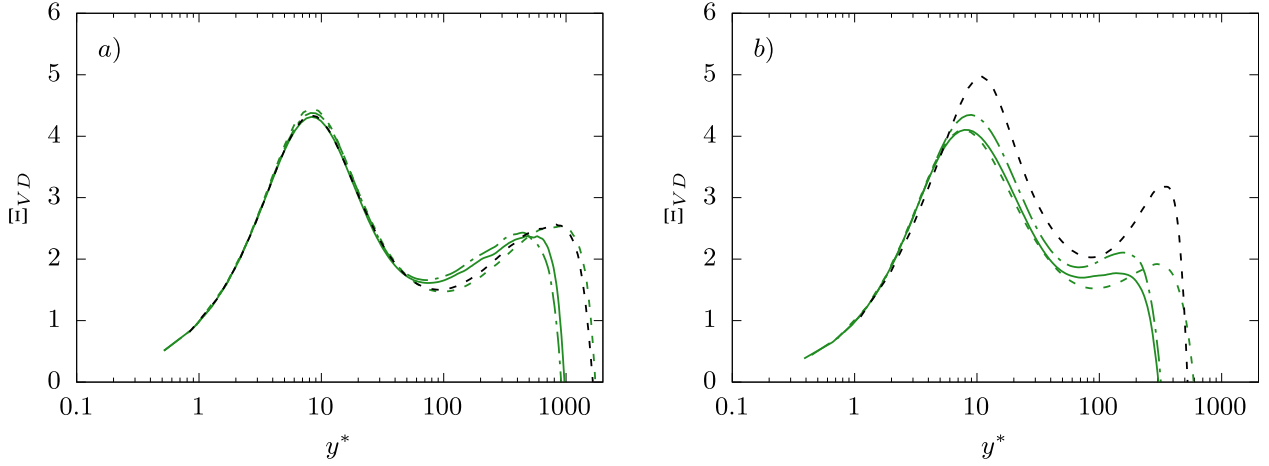


Fig. 6. Indicator function $\Xi_{VD} = y^* du_{VD}^+ / dy^*$ of the van Driest transformed mean velocity profile is presented for the cold wall on the left and for the hot wall on the right. The wall normal distance is based on the semi-local scaling y^* . Cases: TCF55M (—), TCF65M (- · - · -), TCF55MR (- - -), TCF60TR (- - -). (For interpretation of the references to colour in this figure legend, the reader is referred to the web version of this article.)

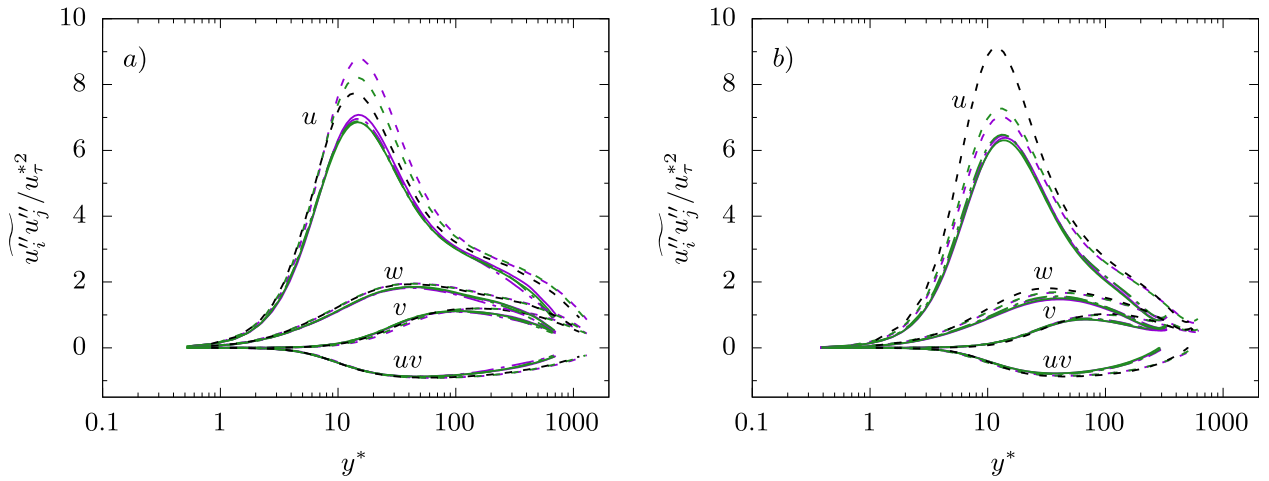


Fig. 7. Reynolds stress profiles at the cold wall (a) and hot wall (b). The profiles are normalized with the semi local friction velocity which is transferable to Morkovin's scaling. Cases: TCF55B (—), TCF65B (- · - · -), TCF55BR (- · - · -), TCF55M (—), TCF65M (- · - · -), TCF55MR (- - -), TCF60TR (- - -). (For interpretation of the references to colour in this figure legend, the reader is referred to the web version of this article.)

studies have been used to determine the constants κ and B . Here, we only perform a qualitative analysis to elaborate the differences between the cases. For all cases the indicator functions overlap in the viscous sublayer, thus, only subtle changes of the velocity profiles in vicinity of the walls can be noted. In the buffer layer around $y^+ = 10$ the indicator functions feature a peak, with minor differences between the cases at the cold wall and larger differences at the hot wall. The next minimum is located approximately at the beginning of the logarithmic layer (Pope and Pope, 2000). Due to the low Reynolds number no plateau is observed for any of the seven cases and the profiles do not collapse for $y^+ > 70$. Applying the indicator function to the Trettel and Larsson transformed mean velocity profiles (not shown) does not provide a better conformance between the data.

4.2. Fluctuations

In this section we analyse the influence of real gas and Reynolds number effects on the Reynolds stresses and on RMS thermodynamic fluctuations. Fig. 7 shows the Favre averaged Reynolds stresses including Morkovin's scaling. The Reynolds stresses exhibit a noticeable Reynolds dependence. For the cases without bulk Reynolds number increase (TCF55B, TCF55M, TCF65b, TCF65M) the semi-local Reynolds numbers Re_τ are close to each other over the entire channel height (see

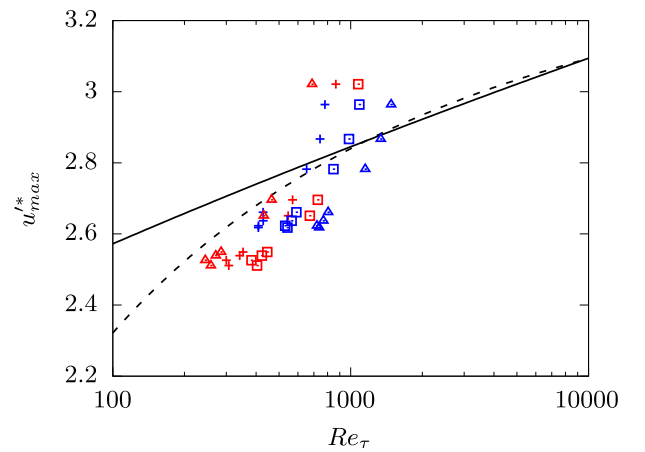


Fig. 8. Streamwise velocity fluctuation maxima shown vs. the corresponding friction Reynolds number Re_τ^* . Lee and Moser (2015) $u_{max}^{'+} \approx 3.66 + 0.642 * \log(Re_\tau)$ (—) and Chen and Sreenivasan (2021) $u_{max}^{'+} \approx 46 * (0.25 - 0.42 / Re_\tau^{0.25})$ (- - -). Blue symbols for the cold and red symbols for the hot wall. (+) represent maxima with their respective Re_τ^* obtained at the wall, (□) with their respective local Re_τ^* obtained at the position of the peak, (△) with their respective local Re_τ^* obtained at the position of the peak including an adjustment of the characteristic length scale.

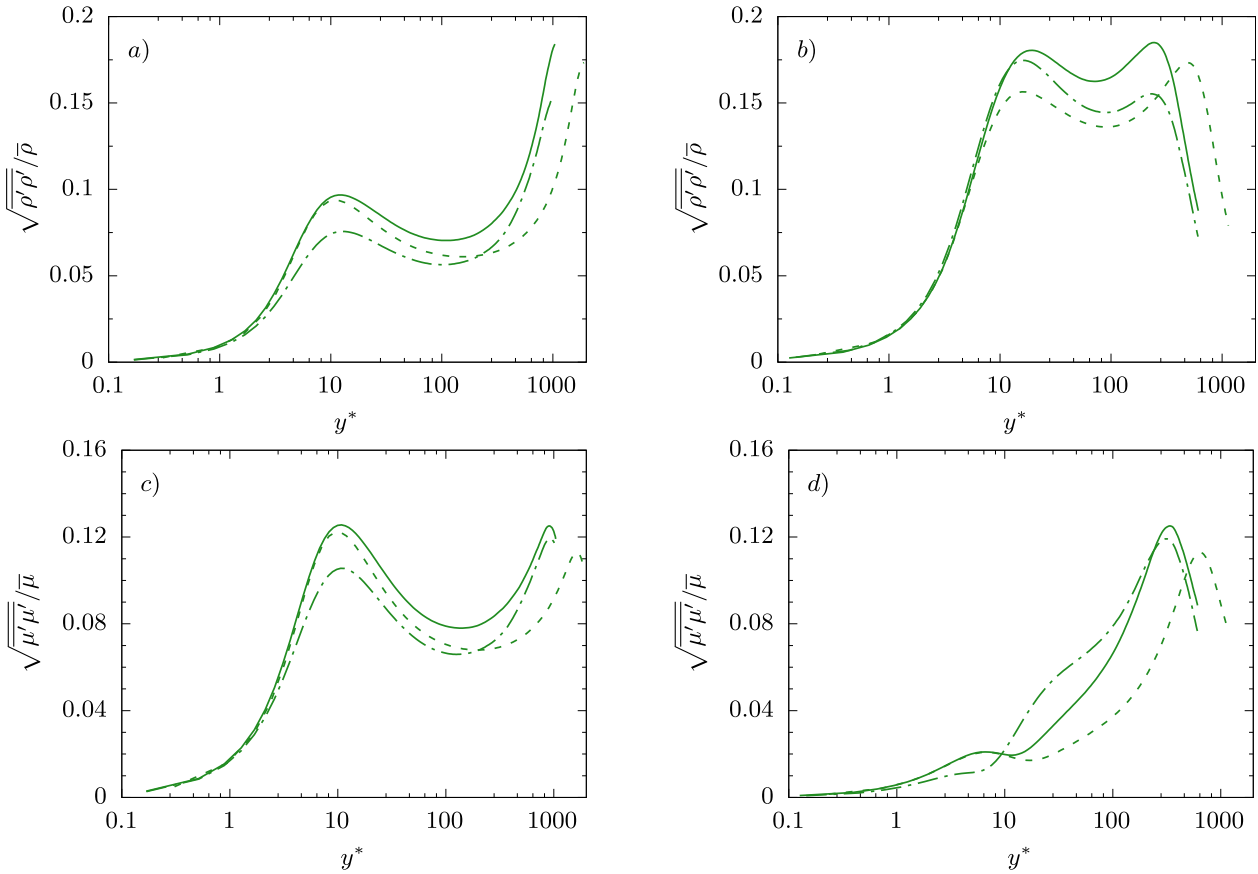


Fig. 9. Root mean square profiles of density (a,b), temperature (c,d), viscosity (e,f) and thermal conductivity (g,h) are depicted over the semi-local channel height. The profiles are normalized with the mean profiles. The left column refers to the cold and the right column to hot wall. Shown are case TCF55M (—), TCF65M (- - -) and TCF55MR (- · - ·).

Fig. 3), resulting in overlapping Reynolds stress profiles at both walls. The Re_τ values of the cases with an increased bulk Reynolds number strongly differ depending on their wall distance. As a consequence, TCF55BR possesses the highest Re_τ^* value with respect to the cold wall, which becomes apparent by the highest $\overline{u' u'}$ peak value. As a result the semi-local scaling u_τ^* and y^* achieves a collapse of the Reynolds stress profiles for similar Re_τ^* , and for varying semi-local Reynolds number the scaling corrects the peak positions such that the peaks are approximately at the same wall normal distance (Foysi et al., 2004; Patel et al., 2015). The advantage of applying the semi-local scaling to Reynolds stresses has also been reported by other studies (Morinishi et al., 2004; Foysi et al., 2004; Patel et al., 2015; Kim et al., 2019). The maximum values of the streamwise fluctuations depending on the friction Reynolds number are displayed in Fig. 8. Recent correlations by Lee and Moser (2015) $u_{max}^* \approx 3.66 + 0.642 * \log(Re_\tau)$ and by Chen and Sreenivasan (2021) $u_{max}^* \approx 46 * (0.25 - 0.42/x^{0.25})$ are included. Using the friction Reynolds numbers at the respective walls, represented by (+), results in a reasonable agreement with the correlation by Chen and Sreenivasan (2021) up to $Re_\tau < 700$. But, Re_τ^* values obtained at the walls do not represent the flow correctly around the locus of streamwise velocity fluctuation maxima, since all cases show varying friction Reynolds number profiles. Thus, we include Re_τ values at the location of u_{max}^* , represented by (□). This leads to a shift along the x-axis because all Re_τ profiles increase with wall distance, see Fig. 3. The next adjustment includes the aforementioned local friction Reynolds number and the momentum boundary layer thickness as a new characteristic length scale instead of the channel half height H , see Fig. 4(a). Since all cases feature a shifted mean velocity peak towards the hot wall at approximately $y/H = 0.36$, we updated the length scale with this peak position, represented by (Δ). As a consequence, the

hot wall peak values are shifted closer to the correlation by Chen and Sreenivasan (2021) ($\delta_{M_h} < H$) and the cold walls values are shifted further away ($\delta_{M_c} > H$). The performed adjustments improve the hot wall peaks regarding the correlation by Chen and Sreenivasan (2021), but worsen them at the cold wall. Furthermore, the peaks which belong to the high Reynolds number cases, stick out with high peak values not following any correlation.

The root-mean-square fluctuating values of the density and viscosity are presented in Fig. 9 normalized by their mean profiles, respectively. For a better illustration only the TCFM profiles are shown. As observed for the mean distributions in Fig. 4, also the fluctuations have a pronounced asymmetry. Both fluctuating quantities show a hump at the cold wall, see Fig. 9 (a), (c). Since TCF55M and TCF55MR have the same reduced pressure, resulting in overlapping mean profiles, also their fluctuations overlap. The density and viscosity fluctuations are smaller with increasing distance to the critical point. A Reynolds number effect starts to be visible in the buffer layer ($y^+ > 10$) for ρ' and μ' .

The intensities of the density fluctuations are higher at the hot wall, but not the viscosity fluctuations, see Fig. 9 (b), (d). Two distinct peaks are observed at $y^+ \approx 10$ and $y^+ \approx 200$ for the density fluctuations. The fluctuation magnitudes exceed 10% for a temperature difference of only 100 K. Regarding real applications, as for instance rocket engines, much higher temperature gradients are expected, thus, leading to fluctuations which cannot be neglected. Similar observations have been made by Guo et al. (2022) and Kawai (2019) with fluctuations partly higher than 20%.

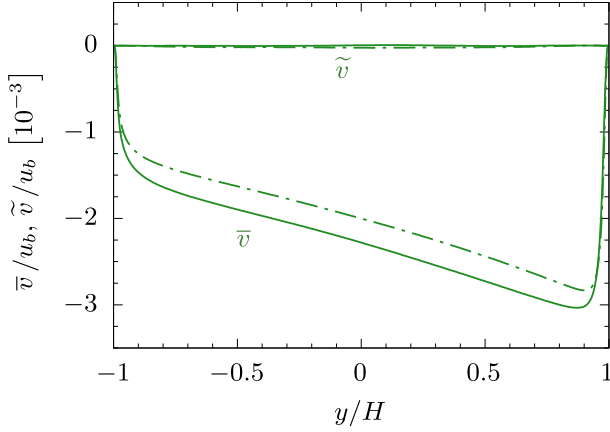


Fig. 10. Mean wall normal velocity profiles are depicted over the channel height for case TCF55M and TCF65M. The velocity v is Reynolds (overline) and Favre (tilde) averaged. Cases: TCF55M (—), TCF65M (- - -).

4.3. Turbulent mass flux

In highly variable Prandtl number flows pseudo-boiling affects the boundary momentum and the thermal boundary layer. Consequently, RANS turbulence models which do not account for variable Prandtl number fail to predict the correct wall shear stress and heat transfer (Kaller et al., 2020; Yoo, 2013). Kawai (2019) reported an induced turbulent mass flux in the boundary layer due to density fluctuations. Also Liu et al. (2020) showed the importance of the turbulent mass flux in spatially-developing turbulent boundary layer under supercritical pressure. In Fig. 10 the Reynolds averaged and Favre averaged wall normal velocity v are presented for cases TCF55M and TCF65M. We omitted the distributions for the streamwise velocity u , since we could not observe a significant difference between both averaging methods. The Reynolds averaged velocity v indicates a flow from the hot to the cold wall with a peak close to the hot wall. An increased pressure TCF65M results in a reduced flow between the walls. By applying the Favre average nearly no wall normal flow can be observed anymore. This difference indicates a turbulent mass flux $\overline{\rho'v'}$ based on a non-vanishing Favre averaged fluctuation

$$\bar{v} - \tilde{v} = \overline{v''} = -\overline{\rho'v'}/\bar{\rho}. \quad (11)$$

Reynolds averaging of the streamwise momentum equation (Smits and Dussauge, 2006) results in additional terms introducing further unknowns. This forms the basis for the RANS turbulence modelling by providing closure models for the additional new terms. In total four new terms are generated shown here for the right hand side.

$$\dots = \frac{-d\bar{p}}{dx} + \frac{\partial}{\partial y} \left[\underbrace{\overline{\mu \frac{\partial \bar{u}}{\partial y}}}_{1} - \underbrace{\overline{\rho u'v'}}_{2} - \underbrace{\overline{u\rho'v'}}_{3} - \underbrace{\overline{v\rho'u'}}_{4} - \underbrace{\overline{\rho'u'v'}}_{4} \right]. \quad (12)$$

We use the simplification

$$\overline{\mu \frac{\partial u}{\partial y}} \approx \bar{\mu} \frac{\partial \bar{u}}{\partial y}. \quad (13)$$

This is justified, since the arising fluctuating part is below 10% of the mean shear, $\mu' \frac{\partial u'}{\partial y} / \bar{\mu} \frac{\partial \bar{u}}{\partial y} < 0.1$. The wall normal mass flux can be found in term number two. In incompressible or weakly compressible flows all terms are neglected except for the Reynolds shear stress (term number one). Especially in highly compressible flows, e.g. hypersonic flows (Dussauge et al., 1996) and transcritical flows this simplification is not valid. In Fig. 11 all four terms are plotted over the semi-local

distance y^* and normalized with the respective wall shear stress. As already indicated by comparison of the Reynolds and Favre averaged wall normal velocity distribution, it is observed that the wall normal mass flux $-\overline{\rho'v'}$ is of the same order as the Reynolds shear stress $\overline{\rho'u'v'}$. It has to be noted that the sign of the shear stress was changed at the hot wall for clarity. The mass flux $-\overline{\rho'v'}$ is negative across the channel, thus, it counteracts the Reynolds shear stress at the cold wall and amplifies the stresses at the hot wall independent of the case. It can even exceed the shear stress at the hot wall where the density fluctuations are high (see Fig. 9b) and also the mean wall normal velocity has its maximum value (see Fig. 10). For this reason, the mass flux has to be considered in RANS turbulence models, see Kawai and Oikawa (2020). The streamwise mass flux $\overline{v\rho'u'}$ and the triple correlation $\overline{\rho'u'v'}$ are two orders of magnitude smaller. Consequently, the contribution of both terms can be neglected at least for the considered cases. In real applications with substantially higher temperature gradients, this may have to be reconsidered.

In Fig. 12 the shear stress and total stress (see Eqs. (12) and (13)) are shown normalized with the wall shear stress. The shear stress $\bar{\mu} \partial \bar{u} / \partial y$ is constant in the viscous sublayer and no difference is observed between the cases. With increasing wall distance the shear stress decreases approaching zero and changes the sign moving towards the hot wall. The total stress is also constant in the viscous sublayer which can be ascribed to the dominance of the shear stress. The two big turbulent stress contributors, the Reynolds shear stress and the turbulent mass flux, counteract each other at the cold wall and unite at the hot wall. This is the result of the sign change of the Reynolds shear stress, whereas the turbulent mass flux is one directional and negative over the whole channel height. As a consequence, the total stress exceeds the wall shear stress at the hot wall.

4.4. Turbulent kinetic energy

In the following, we analyse the cases according to their turbulence dynamics by means of the transport equation for the mean turbulent kinetic energy (TKE) $k = 1/2 u'_i u'_i$. The TKE transport equation is written as

$$\frac{\partial \bar{\rho} k}{\partial t} = C + T + P + D + \Pi + M - \epsilon, \quad (14)$$

where right hand side budgets are the contributions due to convection C , production by mean velocity gradient P , turbulent transport T , pressure dilatation Π , viscous diffusion D , mass flux contribution associated to density fluctuations M and dissipation due to molecular effect ϵ . The individual terms are presented as

$$C = -\frac{\partial \bar{\rho} \bar{u}_j k}{\partial x_j}, \quad (15)$$

$$P = -\bar{\rho} \overline{u'_i u'_j} \frac{\partial \bar{u}_i}{\partial x_j}, \quad (16)$$

$$T = -\frac{\partial}{\partial x_j} \left[\bar{\rho} \frac{u'_i u'_j u'_i}{2} + \overline{p' u'_i} \delta_{ij} \right], \quad (17)$$

$$\Pi = p' \frac{\partial u'_i}{\partial x_i}, \quad (18)$$

$$D = \frac{\partial}{\partial x_j} \left(\tau'_{ij} u'_i \right), \quad (19)$$

$$M = u'_i \left[\frac{\partial \bar{\tau}_{ij}}{\partial x_j} - \frac{\partial \bar{p}}{\partial x_i} \right], \quad (20)$$

$$\epsilon = \tau'_{ij} \frac{\partial u'_i}{\partial x_j}, \quad (21)$$

with the viscous stress tensor τ_{ij} and the Kronecker-Delta function δ_{ij} . The dissipation is expressed as the sum of solenoidal dissipation, dilatational dissipation and contributions due to inhomogeneous effects.

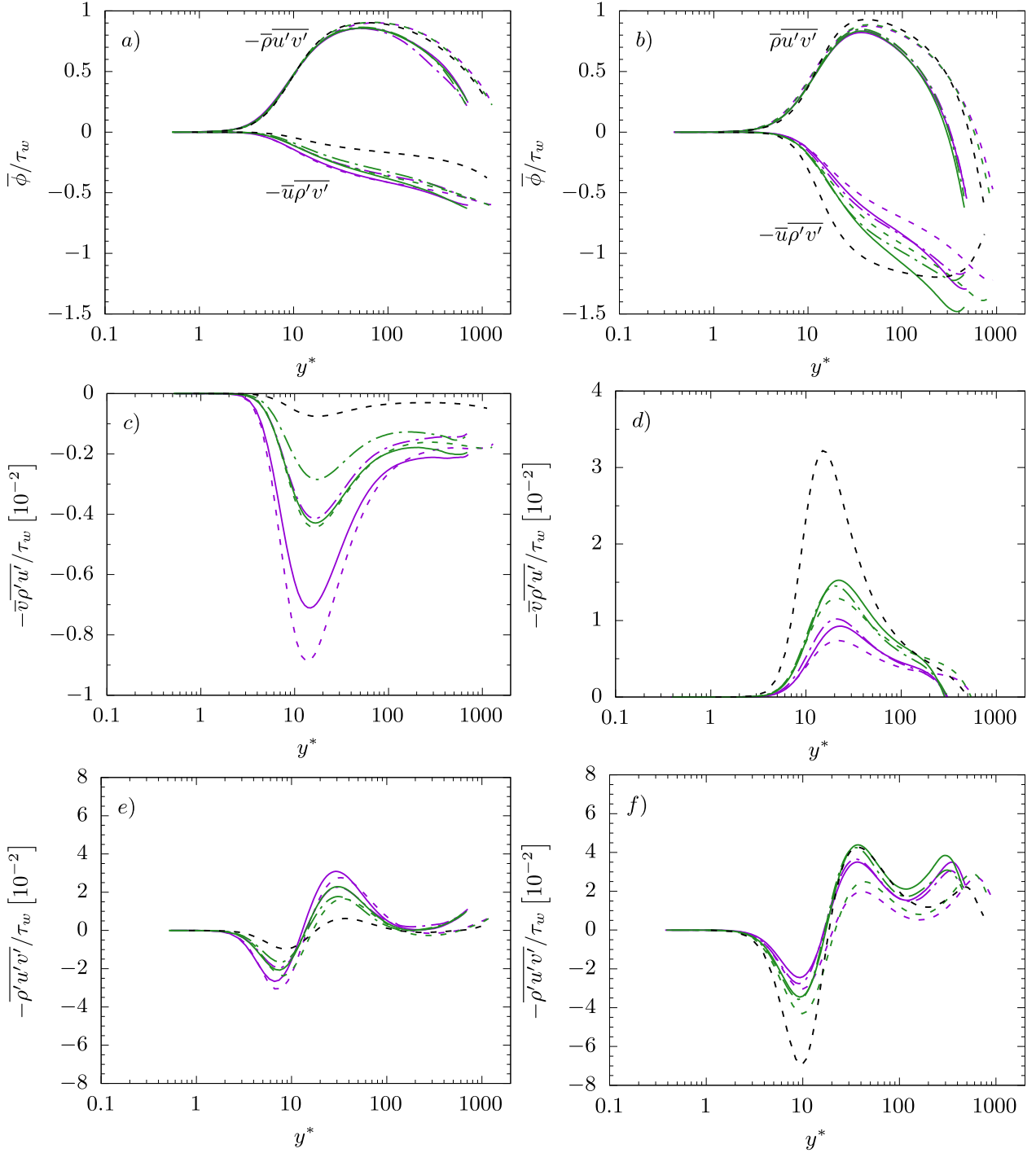


Fig. 11. Unclosed terms obtained by applying the Reynolds averaging to the streamwise momentum equation. The left column refers to the cold and the right column to the hot wall. According to Eq. (12) the Reynolds shear stress and the mass flux in wall normal direction are shown in (a,b), the mass flux in streamwise direction in (c,d) and the triple correlation in (e,f). Cases: TCF55B (—), TCF65B (---), TCF55BR (···), TCF55M (—), TCF65M (---), TCF55MR (···), TCF60TR (— · —). (For interpretation of the references to colour in this figure legend, the reader is referred to the web version of this article.)

Since the later two are negligibly small (not shown), only the solenoidal contribution is considered, see also Pirozzoli et al. (2004) and Shahab et al. (2011). The budgets are scaled over the entire wall-normal distance with respect to $\bar{\rho}_w u_\tau^4 / \bar{\nu}_w$ adopted from Pirozzoli et al. (2004). Instead of wall-normal quantities, local properties $\bar{\rho}_w u_\tau^4 / \bar{\nu}$ are used, in regard to the semi-local scaling. The semi-local scaling repositions the profiles, thus, provides a better collapse between the performed cases and between the cold and hot wall, cf. Duan and Martín (2010).

Semi-local scaling recovers the traditional observations, that the production peaks are located in the buffer layer ($5 < y^+ < 30$), at

the position where the viscous mean stress is equal to the Reynolds shear stress, see Fig. 13(a) and (b). At the cold wall the TKE production, viscous diffusion and dissipation overlap for the low Reynolds number and high Reynolds number cases, respectively. At the hot wall this is only the case for the low Reynolds number simulations, since the budgets for the high Reynolds number cases show a higher variance. This can especially be seen in the viscous diffusion at around $y^* = 7$, reaching lower negative values. Cases with an increased Reynolds number show a higher dissipation close to the wall $y^* < 6$ compared to the other simulations. Although, the production and diffusion overlap

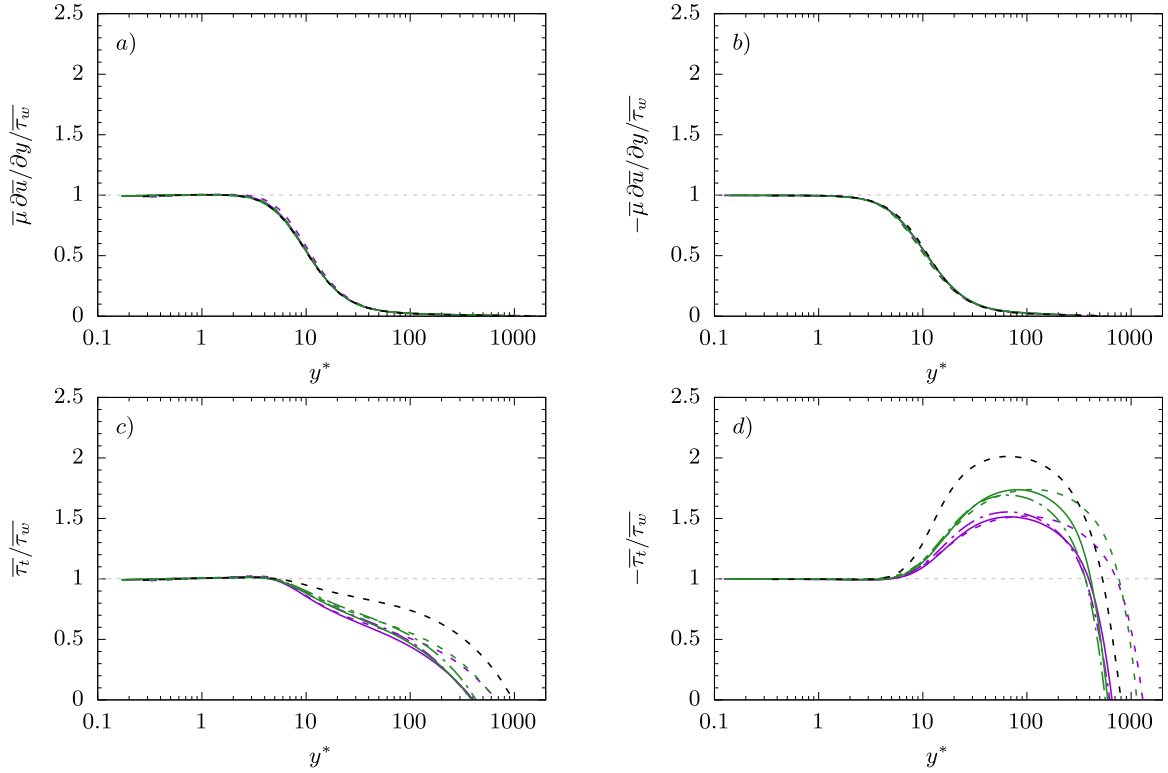


Fig. 12. The shear stress $\bar{\mu} \partial \bar{u} / \partial y$ and the total stress $\bar{\tau}_t$ from Eq. (12) are normalized with the wall shear stress. The cold wall is presented at the left column and the hot wall at the right column.

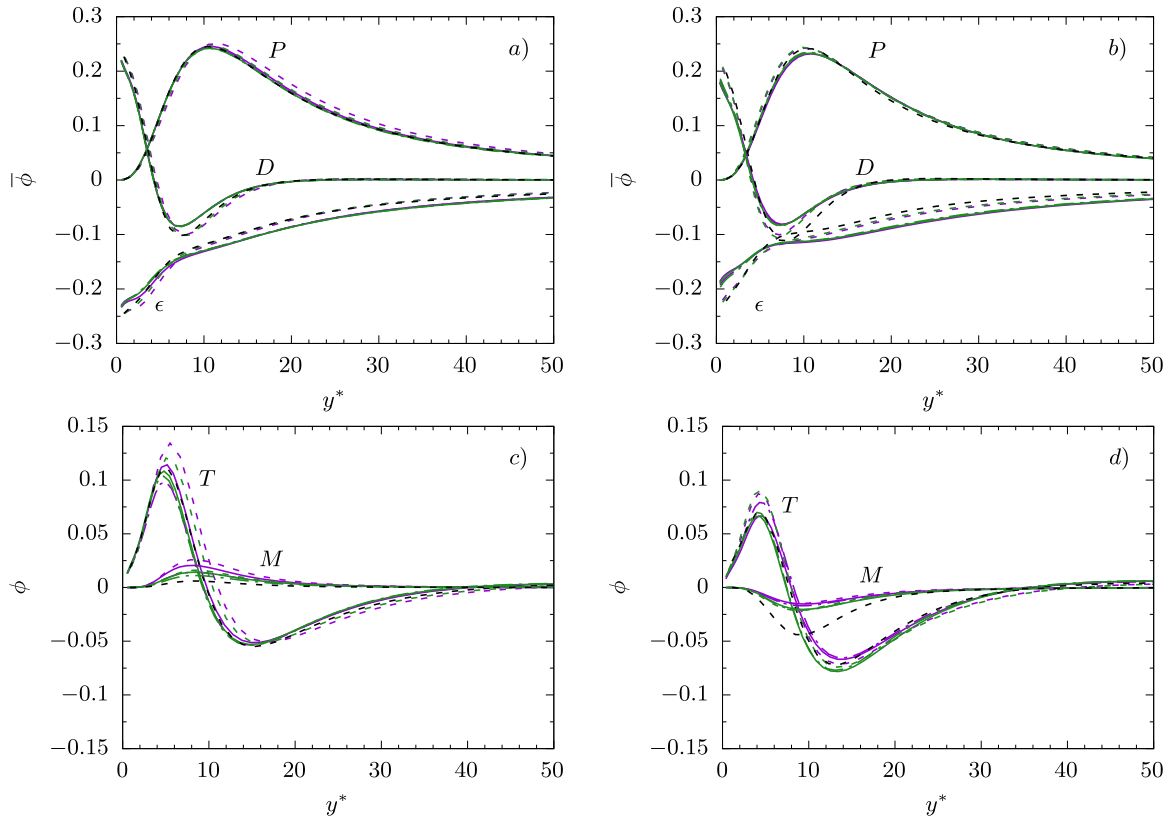


Fig. 13. Turbulent kinetic budgets normalized with $\bar{\rho} u_{\tau}^{*4} / \bar{\nu}$ over the semi-local wall distance y^* . The production P , viscous diffusion D and dissipation ϵ in (a,b), and turbulent transport T and mass flux M in (c,d). The cold wall is presented on the left (a,c) and the hot wall on the right (b,d). Cases: TCF55B (—), TCF65B (---), TCF55BR (---), TCF55M (—), TCF65M (---), TCF55MR (---), TCF60TR (---). (For interpretation of the references to colour in this figure legend, the reader is referred to the web version of this article.)

in the logarithmic region ($y^+ > 30$) is independent of the case, a Reynolds dependence of the dissipation can be observed. In summary, all three budgets P , D , and ϵ are marginally sensitive to pressure changes and consequently, to changes of the heat capacity distribution. In contrast, turbulent transport and mass flux are sensitive to both, Reynolds number and pressure level (real gas intensity) shown in Fig. 13(c) and (d). Case TCF60TR exhibits a high mass flux shown in Fig. 11(b), which also stands out in the budgets. The mass flux reaches up to 14% (TCF55BR) at the cold and up to 20% (TCF60TR) at the hot wall of the local TKE production. Thus, it has to be considered in the turbulence modelling for transcritical flows, cf. Kawai (2019), Kawai and Oikawa (2020). Duan and Martín (2010) also observed a slight variance in the profile using a semi-local scaling for the budgets, which they ascribe to variations in mean fluid properties. This is supported for instance by the DNS study of a channel flow with varying viscosity by Zonta et al. (2012a) and a duct flow by Kaller et al. (2019). They observed a promotion of turbulence for increased viscosity levels and a decrease with lower viscosity levels using water. The viscosity profiles obtained in our cases are shown in Appendix B.

4.5. Quadrant and octant analysis

In the following we analyse the influence of the Reynolds number and the real gas effects on the ejection and sweeping motion in the boundary layer, which was firstly discussed by Wallace et al. (1972). At first, applying the quadrant analysis allows us to identify the main contribution to turbulence and how they are affected (Wallace, 2016). The Reynolds shear stress $u'v'$ is split into four quadrants depending on the signs of the streamwise u' and wall normal v' fluctuations. The first quadrant $Q1$ $u' > 0$, $v' > 0$ refers to an outward motion of high-velocity fluid, the second quadrant $Q2$ $u' < 0$, $v' > 0$ to an outward motion of low-velocity fluid, the third quadrant $Q3$ $u' < 0$, $v' < 0$ to an inward motion of low-velocity fluid and the fourth quadrant $Q4$ $u' > 0$, $v' < 0$ to an inward motion of high-velocity fluid.

In turbulent boundary layer flows $Q2$ is connected to turbulent ejections and $Q4$ to turbulent sweeping motions shown by Willmarth and Lu (1972). The definitions of the quadrants is shown in Table 4. Note, that an outward motion at the hot wall is indicated by a negative wall normal fluctuation. Thus, the sign of v' is reversed at the hot wall compared to the cold. This is indicated in Table 4 in blue and red colour for the cold and hot wall, respectively. Fig. 14 shows the quadrant analysis for the Reynolds shear stress $u'v'$ at the cold wall and hot wall. Firstly, we focus on the quadrants $Q2$ and $Q4$ in Fig. 14. Both quadrants feature a peak in the vicinity of the wall. The intensity represented by the maximum value is slightly higher for the ejections ($Q2$) than for the sweeps ($Q4$). On the other hand the size of the sweeping motion is larger with $l^+ \approx 285$ than the ejection size motion with $l^+ \approx 168$ exemplarily for TCF55BR at the cold wall. The size is defined as the distance from the wall where the maximum intensity drops to 90%. A vertical line in Fig. 14 is used to indicate the size of the sweeping motion. The comparison between $Q2$ and $Q4$ at the hot wall features the same trends. Heating reduces the size of sweeps and ejections, cf. Figs. 14(e) and (f), and 14(g) and (h). Apart from this, the intensity of $Q4$ at the hot wall is smaller than at the cold wall. Kaller et al. (2019) and Lee et al. (2013) showed that a reduction of viscosity acts stabilizing by reducing the intensity of turbulent ejections and sweeps. This holds for our study only for $Q4$, but we have to mention, that we use the semi local friction velocity for normalization. Our scaling accounts for viscosity changes, which is not the case in the studies mentioned above. The present temperature distribution and the resulting viscosity reduction from the cold to the hot wall leads to a reduction of the turbulent sweeps by approximately 20%. The intensity of $Q1$ and $Q3$ is four to six times smaller compared to $Q2$ and $Q4$. Similar to the observations made with sweeps and ejections, also here the intensity of $Q1$ and $Q3$ at the cold wall is higher than at the hot wall. Additionally, the size of the motion is larger at the cold side than

Table 4

Definition of the quadrants and octants for the Reynolds stress quadrant and octant analysis. The red and blue colour refer to the hot and cold wall, respectively.

$u'v'$	Q1		Q2		Q3		Q4	
	O1	O4	O2	O3	O6	O7	O5	O8
u'		+		-		-		+
v'		+		+		-		-
v'		-		-		+		+
T'	+	-	+	-	+	-	+	-
μ'	+	-	+	-	+	-	+	-

at the hot side. The shape of $Q1$ and $Q3$ at the cold wall has a hump at approximately $y^* = 200 - 500$, which cannot be observed at the hot wall.

In Fig. 15 the analysis of the crossing position between $Q2$ (ejections) and $Q4$ (sweeps) is shown exemplarily for TCF55B and TCF560TR. The intensity of the sweeps starts to flatten at $y^+ = 10$, where that of ejections is still rising, leading to a change of the dominant mechanism. The position where the “sweep dominance” changes to “ejection dominance” is shown for all cases in Table 5. The change in pressure has only a marginal effect on the location, whereas a higher Reynolds number lifts the point away from the wall. The change in dominance for all cases is located in the buffer layer and is similar to $y^+ = 14$, which was observed in the DNS study by Zonta et al. (2012a). Heating moves the location of change in dominance closer to the wall, compared to a cooling.

Further, we split the sweeps ($Q4$) and ejections ($Q2$) based on the signs of the temperature and viscosity fluctuations. This method is referred to as octant analysis, which is based on Wallace (2016). The definition is given in Table 4. We will focus on octant $O2$ and $O3$ since these are related to the second quadrant (ejections) and octant $O5$ and $O8$ since these are related to the fourth quadrant (sweeps) in the analysis above. The Reynolds stress distributions are shown in Fig. 16 based on the temperature splitting. As expected, ejections are an outward movement away from the wall mostly consist of negative temperature fluctuations, thus, bringing cold fluid away from the wall. Hot fluid is brought by sweeping motion towards the cool wall. The other contributions, as hot fluid away from the wall and cold fluid towards the wall are infrequent, thus, their contribution to the sweeps and ejections is small. These observations apply to the cold wall, whereas the opposite is the case at the hot wall. The semi-local scaling achieves for the most part to collapse the profiles, only a Reynolds number effect is visible.

Applying the same method in conjunction with the viscosity fluctuations results in similar observations at the cool side, see Fig. 17. Positive viscosity fluctuations, which are related to cooler fluid are transported away from the wall, and negative viscosity fluctuations related to hotter fluid are moved towards the cool wall. At the hot wall this strict splitting does not hold anymore. Due to the change of sign in the mean viscosity distribution (see Fig. B.22 in Appendix B) and a resulting viscosity minimum close to the hot wall, both octants contribute to $Q2$ and $Q4$, respectively. $O2$ is dominating the ejections until a certain wall distance, where then $O3$ takes over and is the main contributor. Furthermore, no collapse of the profiles using the semi-local scaling is achieved.

4.6. Anisotropy

In turbulence modelling the knowledge of anisotropy effects is crucial. For this reason, we further analyse the influence of real gas effects on turbulence anisotropy using an invariant map. The anisotropy tensor is defined as

$$a_{ij} = \frac{\overline{u'_i u'_j}}{2k} - \frac{\delta_{ij}}{3}, \quad (22)$$

with the kinetic energy k and the Kronecker delta δ_{ij} . The invariant map that we use is the Lumley triangle formed by three limiting states

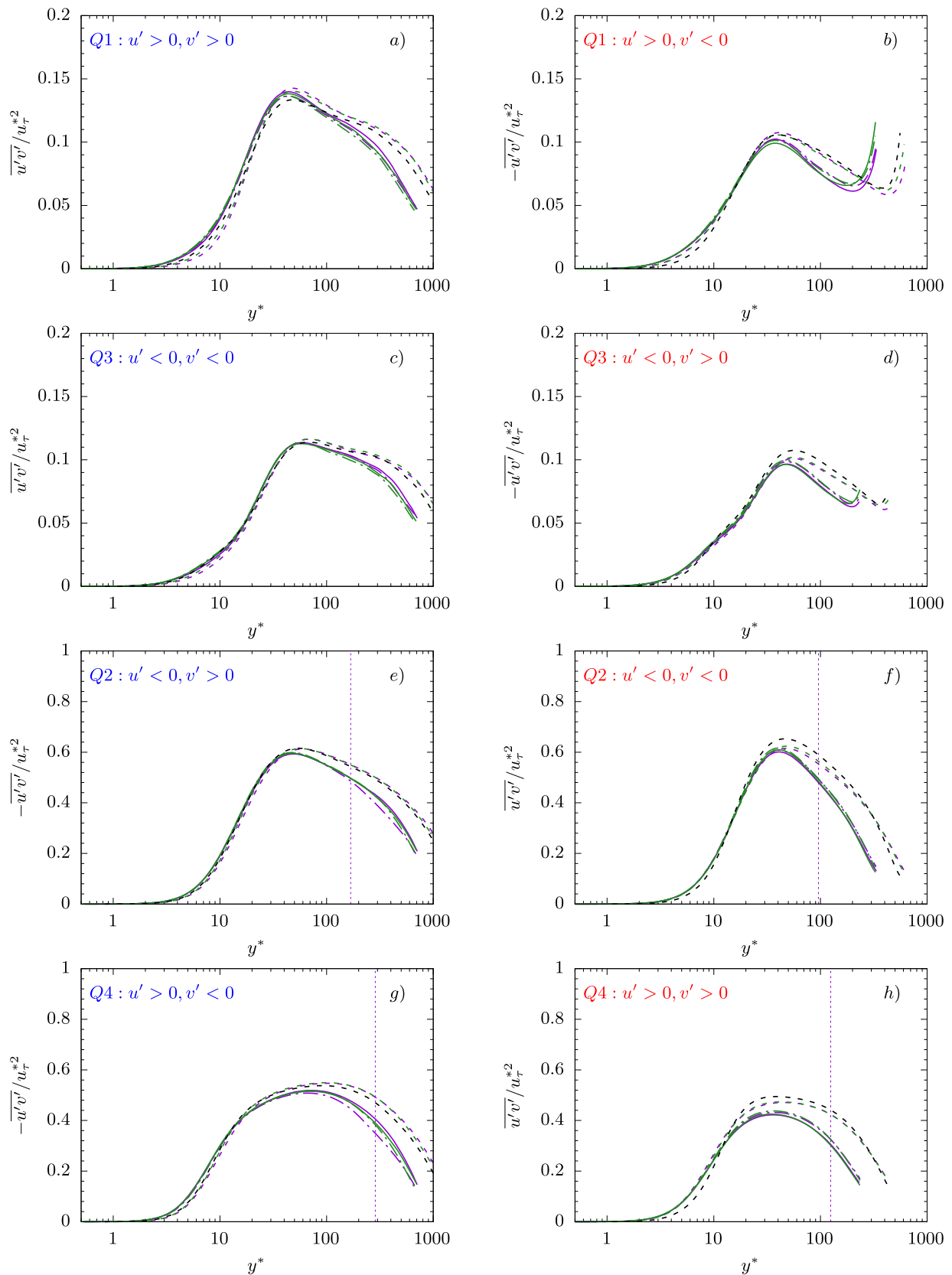


Fig. 14. Quadrant analysis of the Reynolds shear stress $\overline{u'v'}$ over the normalized wall distance y^+ . The cold wall in (a,c,e,g) and the hot wall in (b,d,f,h). The size of the ejections and sweeps is indicated for case TCF55BR by a vertical line (- - - -). Cases: TCF55B (———), TCF65B (- - - -), TCF55BR (- - - -), TCF55M (———), TCF65M (- - - -), TCF55MR (- - - -), TCF60TR (- - - -). (For interpretation of the references to colour in this figure legend, the reader is referred to the web version of this article.)

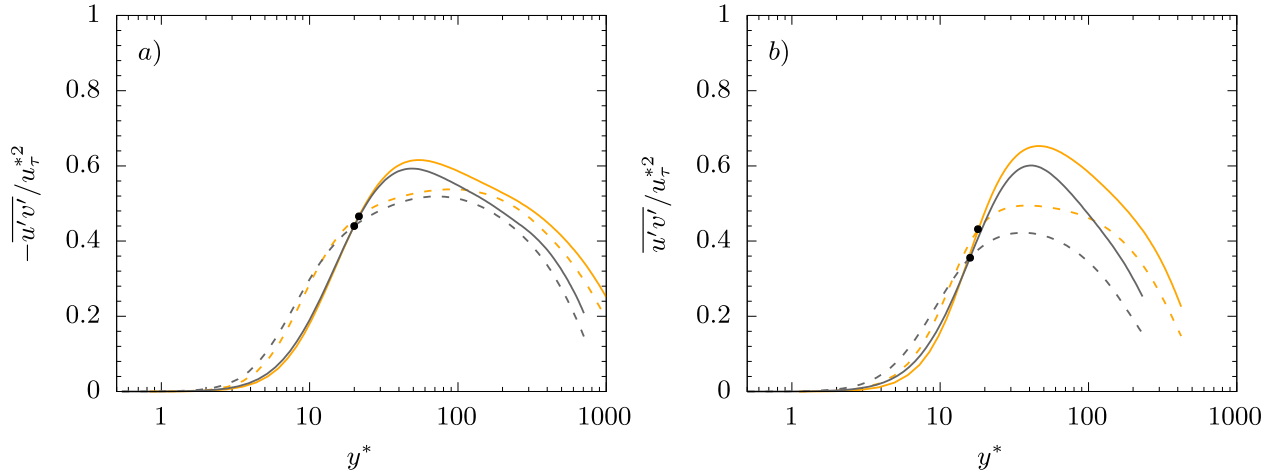


Fig. 15. Location of the sweep dominance to ejection dominance change indicated by black dots. Cold wall in (a) and hot wall in (b). (—) ejections (Q2) and (- - -) sweeps (Q4) of TCF55B, (—) ejections (Q2) and (- - -) sweeps (Q4) of TCF60TR. (For interpretation of the references to colour in this figure legend, the reader is referred to the web version of this article.)

Table 5
Location of dominance change between ejections and sweeps.

y^*	TCF55B	TCF65B	TCF55BR	TCF55M	TCF65M	TCF55MR	TCF60TR
cold wall	20.0	19.1	23.2	19.3	19.3	22.4	21.5
hot wall	15.9	16	18.6	16.0	16.2	18.9	18.0

- (a) 1-component turbulence: turbulent fluctuations in one direction are dominant
- (b) 2-component turbulence: turbulent fluctuations in two directions are dominant
- (c) 3-component turbulence: isotropic turbulence.

Any anisotropy state is a convex combination of these three limiting states lying within the Lumley triangle. The Lumley triangle encloses all states by the 2-component limit edge, which extends from the 2-component axisymmetric to the 1-component limit, by the axisymmetric expansion edge, which extends from the 1-component limit to the isotropic state limit, and by the axisymmetric compression from the isotropic state limit to the 2-component axisymmetric limit. As coordinate system the second and third invariant of the anisotropy tensor are employed

$$I_2 = \frac{a_{ij}a_{ji}}{2} = \lambda_1^2 + \lambda_1\lambda_2 + \lambda_2^2, \quad (23)$$

$$I_3 = \frac{a_{ij}a_{jn}a_{ni}}{3} = -\lambda_1\lambda_2(\lambda_1 + \lambda_2). \quad (24)$$

In Fig. 18 the anisotropy-invariant map is shown, analysing the effect of pressure by comparing TCF55B with TCF65B, the effect of the Reynolds number by comparing TCF55B with TCF55BR and the effect of the c_p distribution comparing TCF55BR, TCF55MR and TCF60TR. The figure shows the turbulence anisotropy along the y -direction starting at the wall and ending close to the point of isotropic turbulence.

All profiles start at the 2-component limit edge and move to the 1-component state limit with increasing wall distance. The highest amount of anisotropy is reached in the buffer layer at approximately $y^* = 8$. Afterwards, the profiles make a turn and move in parallel with the edge of the axisymmetric expansion in the direction of isotropic turbulence until the kink, which is located approximately in the logarithmic layer (see zoom at the bottom of each subfigure in Fig. 18). After this kink the profiles follow the edge of the axisymmetric expansion in the direction of isotropic turbulence until the position of \bar{u}_{max} . This distribution is in agreement with boundary layer flows without real gas effects, cf. Kaller et al. (2019) and Pasquariello et al. (2014). The comparison of the anisotropy-invariant maps for different effects within the channel results in the following observations:

- Pressure difference: The profiles overlap for the most part. Higher pressure, thus, larger distance from the critical point results in a slight decrease of anisotropy maximum (1-component) at the hot wall and a slight increase at the cold wall. The differences in the kink cannot be attributed to the pressure change since for cases TCF55M and TCF65M (not shown) the opposite behaviour is observed.
- Reynolds number: A higher Reynolds number amplifies the anisotropy maximum at the 1-component limit. Again, differences in the kink cannot be attributed to a Reynolds number effect.
- Thermodynamic property variation: At the cold wall the TCF55B has the highest c_p values, followed by TCF55M and TCF60T. This results in higher anisotropy values at the 1-component limit with increasing specific heat capacity.

In addition to the observed effects, it can be seen, that the kink in the logarithmic layer is smoother at the hot wall compared to the cold wall for all simulations. Compare the kink in the bottom zoom between the top row (cold wall) and the bottom row (hot wall) in Fig. 18.

Complementary to the invariant analysis the anisotropy stress tensor components are shown in Fig. 19. The streamwise anisotropy a_{11} is higher at the hot wall then at the cold wall, compare Fig. 19(a) with 19(e). This is in agreement with the observations by Patel et al. (2016) and Kaller et al. (2019) where a lower viscosity leads to higher a_{11} and lower a_{33} values. Patel et al. (2016) also reported that there is no influence of the thermodynamic properties on the wall normal anisotropy, which holds to a certain extend for our cases. In Fig. 19(b), (f) the wall normal component a_{22} features a small spreading of the profiles in the buffer layer. At the cold wall there is a clear distinction between the high and low Reynolds number cases, and at the hot wall the cases do not overlap nicely for $y^+ > 10$. Especially, case TCF60TR stands out at the hot wall. As already observed using the Lumley triangle, a higher Reynolds number leads to higher anisotropy, especially at the hot wall, see Figs. 19(a,c) and 18(b). The component a_{12} is the ratio of turbulent shear stress to the turbulent kinetic energy, referring to the amount of momentum transfer, presented in Fig. 19(d) and (h). At the cold wall a Reynolds number increase reduces a_{12} leading to a smaller momentum transfer. This observation holds only for TCF60TR at the hot wall. The other off-diagonal components a_{13} and a_{23} are negligible and therefore not shown.

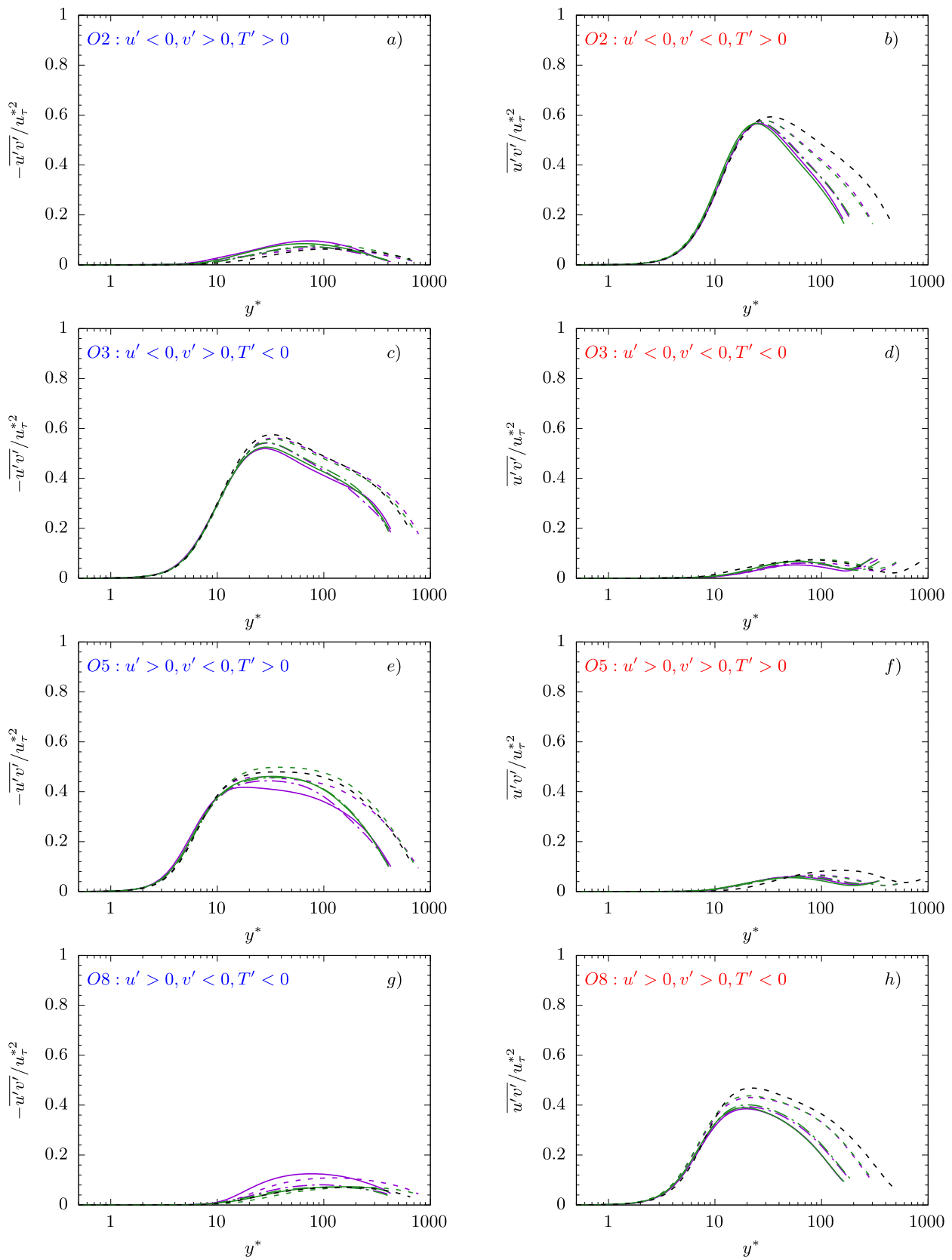


Fig. 16. Octant analysis of the Reynolds shear stress $\overline{u'v'}$ over the normalized wall distance y^* . The quadrants Q2 and Q4 are split based on the temperature fluctuation T' . The cold wall in (a,c,e,g) and the hot wall in (b,d,f,h). Cases: TCF55B (—), TCF65B (- - -), TCF55BR (- - -), TCF55M (—), TCF65M (- - -), TCF55MR (- - -), TCF60TR (- - -). (For interpretation of the references to colour in this figure legend, the reader is referred to the web version of this article.)

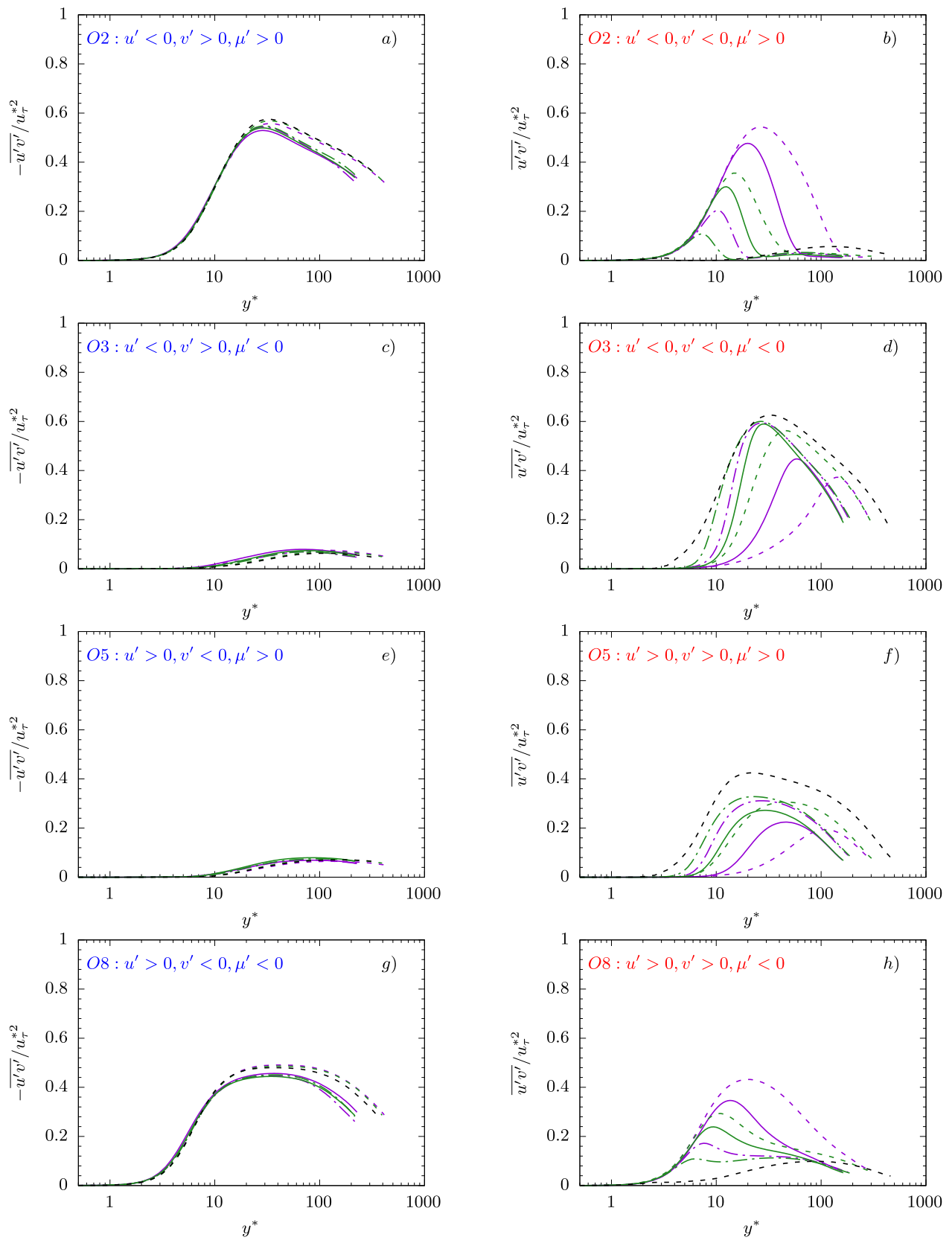


Fig. 17. Octant analysis of the Reynolds shear stress $\overline{u'v'}$ over the normalized wall distance y^* . The quadrants Q2 and Q4 are split based on the viscosity fluctuation μ' . The cold wall in (a,c,e,g) and the hot wall in (b,d,f,h). Cases: TCF55B (—), TCF65B (- - -), TCF55BR (····), TCF55M (—), TCF65M (- - -), TCF55MR (····), TCF60TR (- - -). (For interpretation of the references to colour in this figure legend, the reader is referred to the web version of this article.)

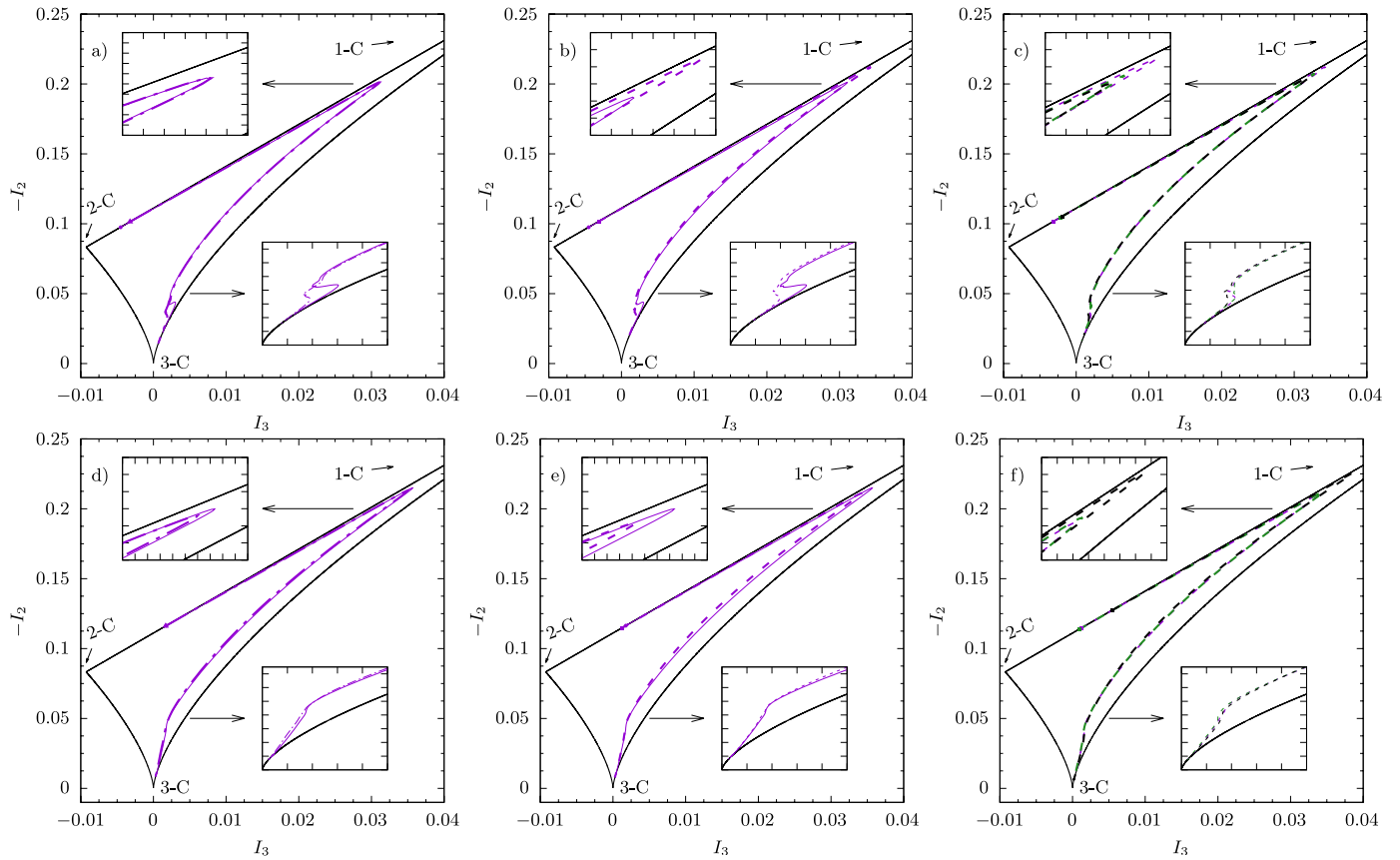


Fig. 18. Reynolds stress anisotropy-invariant map with increasing wall normal distance at the cold (top row) and hot (bottom row) wall. The limiting states are defined by the Lumley triangle. Two close-up views are included for the one-component maximum (top zoom) and the kink in the logarithmic layer (bottom zoom). The effect of pressure is shown by means of TCF55B and TCF65B in (a,d), the effect of the Reynolds number by means of TCF55B and TCF55BR in (b,e) and the effect of the c_p distribution by means of TCF55BR, TCF55MR and TCF60TR in (c,f).

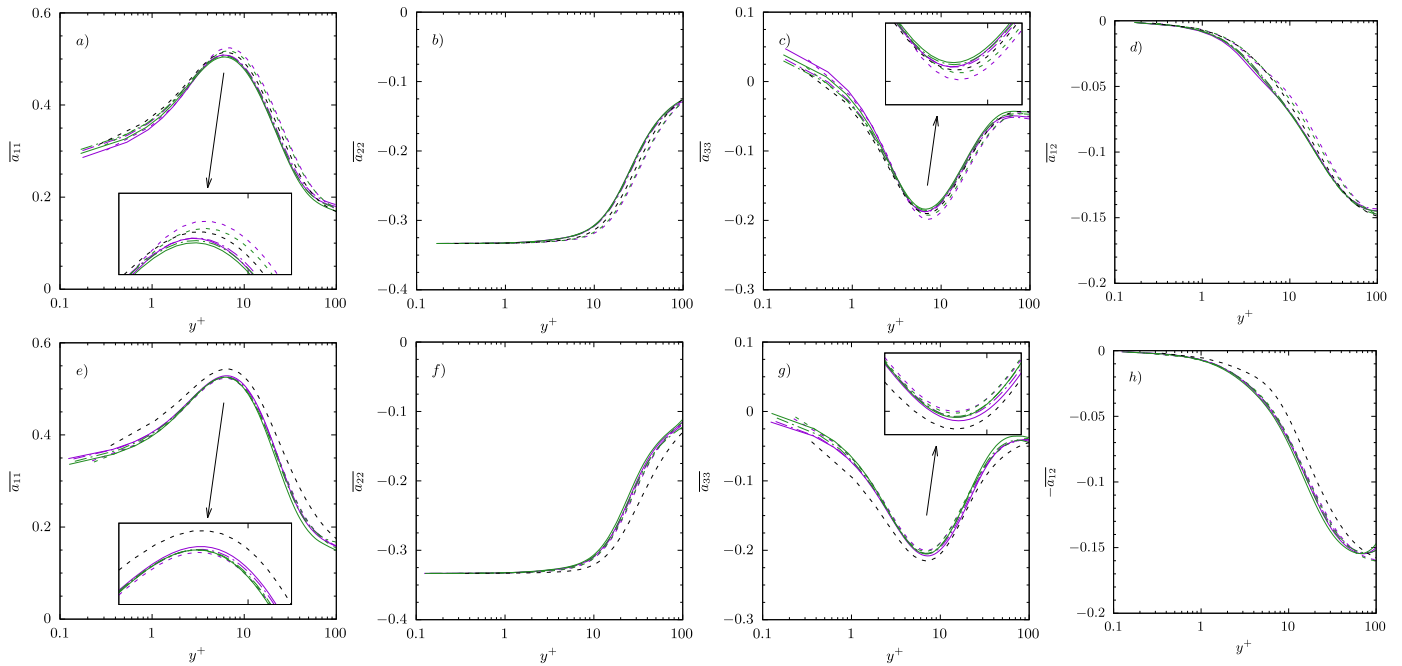


Fig. 19. Anisotropy tensor components for the streamwise component in (a,e), wall normal component in (b,f), spanwise component (c,g) and of diagonal component a_{12} in (d,h). The cold wall is shown in the top row and the hot wall in the bottom row. Cases: TCF55B (—), TCF65B (- - -), TCF55BR (···), TCF55M (—), TCF65M (- - -), TCF55MR (···), TCF60TR (- - -). (For interpretation of the references to colour in this figure legend, the reader is referred to the web version of this article.)

Table A.6
Summary of grid parameters for the sensitivity study related to case TCF55B.

	LvLO	LvL1	LvL2	LvL3	LvL4
$N_x \times N_y \times N_z$	48 × 48 × 48	64 × 64 × 64	96 × 96 × 96	128 × 128 × 128	256 × 256 × 256
$L_x \times L_y \times L_z$			$4\pi H \times 2H \times 4/3\pi H$		
$\Delta x_{\text{cold}}^+ \times \Delta x_{\text{hot}}^+$	93.8 × 71.9	75.5 × 56.6	54.0 × 39.6	41.6 × 30.0	21.0 × 14.7
$\Delta z_{\text{cold}}^+ \times \Delta z_{\text{hot}}^+$	31.3 × 24.0	25.2 × 18.9	18.0 × 13.2	13.9 × 10.0	7.00 × 4.90
$\Delta y_{\text{min.cold}}^+ \times \Delta y_{\text{min.hot}}^+$	1.70 × 1.30	1.30 × 1.00	0.92 × 0.68	0.70 × 0.51	0.35 × 0.25
$\Delta y_{\text{max.cold}}^+ \times \Delta y_{\text{max.hot}}^+$	34.0 × 26.0	27.4 × 20.5	19.6 × 14.4	13.9 × 10.0	7.60 × 5.30

5. Conclusion

We have investigated a turbulent transcritical channel flow configuration imposing different wall temperatures, bulk pressures and Reynolds numbers by well-resolved LES. In total seven cases have been analysed to identify an influence of the thermodynamic non-linear behaviour by rearranging the position of the specific heat capacity peak, an influence of the non-linear intensity by adjusting the distance to the critical pressure and an influence of the Reynolds number. The fully compressible Navier–Stokes equations have been solved and an adaptive look-up table method has been used for thermodynamic and transport properties.

The mean profiles of all quantities show an asymmetric distribution due to the presence of a cold and a hot wall. Only marginal changes are observed in the mean velocity distribution, whereas for instance the mean Prandtl number highly varies depending on the boundary conditions of the case. The velocity scaling by Trettel and Larsson improved the intercept in the logarithmic layer compared to the van Driest scaling, but the hot wall was showing some small spreading. Especially case TCF60TR did not follow the incompressible law of the wall. The spreading and behaviour of case TCF60TR at the hot wall was supported by indicator function.

Performing an averaging of the streamwise momentum equation result in four unclosed terms. The turbulent mass flux is one of the unclosed terms, which has to be accounted for in RANS modelling, since it is at the same order as the Reynolds shear stress. The remaining other two terms increase, with stronger real gas effects and a higher Reynolds number. But they are still one order of magnitude smaller than the turbulent mass flux and the Reynolds shear stress.

The analysis of the turbulent kinetic energy budgets shows overlapping profiles for the production, diffusion and dissipation using a semi-local scaling. Only an influence of the Reynolds number is observed for these terms. On the other hand the semi-local scaling failed for the turbulent transport and mass flux. Here, a spreading for all cases was observed.

A quadrant analysis of the Reynolds shear stress $\overline{u'v'}$ has been performed, showing that intensity of ejections is higher compared to the sweeping motion. Although, sweeps are less intense they are larger in size. The size of the sweeping and ejection motion is reduced by heating. The intensity of quadrant 1 and quadrant 3 is four to six times smaller compared to Q2 and Q4.

The anisotropy by means of the Lumley triangle reveal an increase with increasing Reynold number and with increasing heat capacity.

Overall, case TCF60TR for the most part of the study is not in accordance with the other results. Thus, this case featuring a heat capacity peak at the hot wall is interesting for further analysis.

Moreover, the obtained statistical data and the observed phenomenon are based on the non-ideal thermodynamic and transport properties of methane. We expect that other working fluids with similar thermodynamic properties will lead to the same observations. This can be seen, for example, from the turbulent mass flow that has also been observed for supercritical CO₂ (Kawai, 2019).

CRedit authorship contribution statement

Alexander Doehring: Conceptualization, Methodology, Validation, Formal analysis, Writing – original draft, Visualization, Writing – review & editing. **Steffen J. Schmidt:** Software, Writing – review & editing, Supervision, Project administration. **Nikolaus A. Adams:** Software, Writing – review & editing, Supervision, Project administration, Funding acquisition.

Declaration of competing interest

The authors declare that they have no known competing financial interests or personal relationships that could have appeared to influence the work reported in this paper.

Data availability

Data will be made available on request.

Acknowledgements

The authors gratefully acknowledge the financial support provided by the German Research Foundation (Deutsche Forschungsgemeinschaft-DFG) within the framework of the Sonderforschungsbereich Transregio 40, SFB-TRR40 (Technological foundations for the design of thermally and mechanically highly loaded components of future space transportation systems). Computational resources have been provided by the Leibniz Supercomputing Centre Munich (LRZ).

Furthermore, we would like to thank Rainer Friedrich for providing some literature regarding the turbulent mass flux and Jean-Pierre Hickey for the discussion on unclosed terms during the research stay in Waterloo.

Appendix A. Grid sensitivity study

A grid sensitivity study has been performed for case TCF55B. The domain extensions have not been changed and the bulk pressure of each level is between 55.5 bar and 54.0 bar. LvL4 is the resolution which has been used in the main part of the manuscript, see Table 2. The main parameters for the used grids included in the sensitivity study are summarized in Table A.6.

It has to be mentioned that in transcritical turbulent channel flows every grid level is a slightly different case with a different bulk pressure, bulk temperature and bulk heat capacity distribution due to the non-linear thermodynamics.

In Fig. A.20 the Trettel and Larsson transformed velocity profiles are shown. It can be observed, that the velocity profile at both walls reduces in the logarithmic layer. The velocity profiles approach each other with increasing resolution.

The Reynolds stresses normalized with the semi-local friction velocity are presented in Fig. A.21. At both walls the wall normal and spanwise velocity show minor differences between grid level LvL3 and LvL4 indicating a sufficient resolution for LvL4. For the streamwise direction the peak value is still adjusting for the finest grid level at the cold wall, whereas no difference is observed for the Reynolds stress profile uuu at the hot wall.

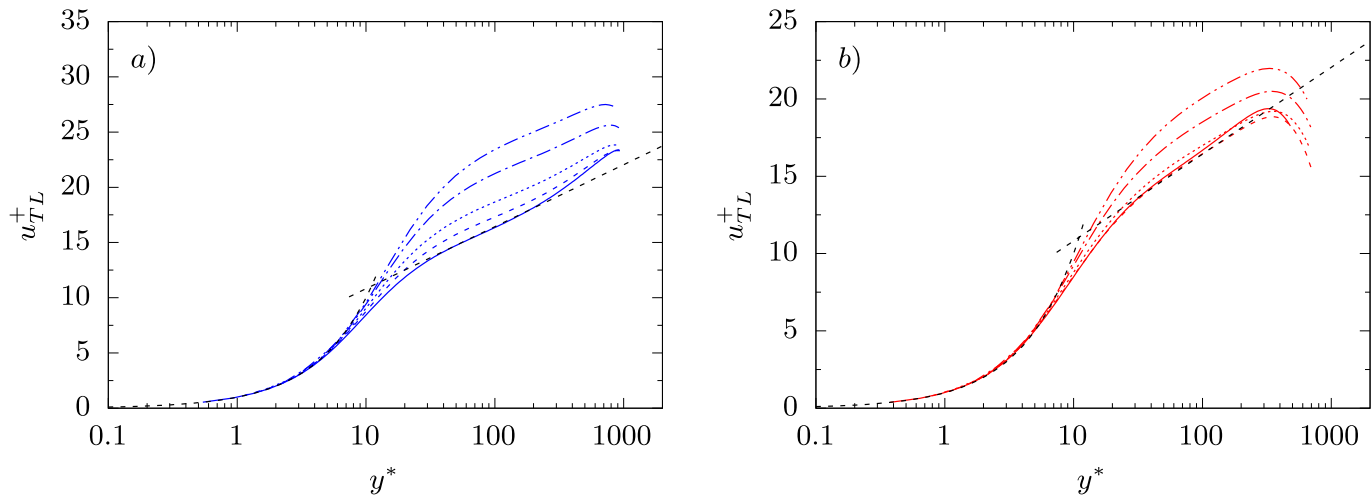


Fig. A.20. Trettel and Larsson scaled velocity profiles for case TCF55B at different grid levels: LvL0 (- · · · · ·), LvL1 (- · · · ·), LvL2 (· · · · ·), LvL3 (- - - -) and LvL4 (———). The viscous sublayer and the logarithmic law are indicated with black dashed lines based on the constants $B = 5.2$ and $\kappa = 0.41$. The cold and hot wall are presented in subfigure (a) and (b), respectively.

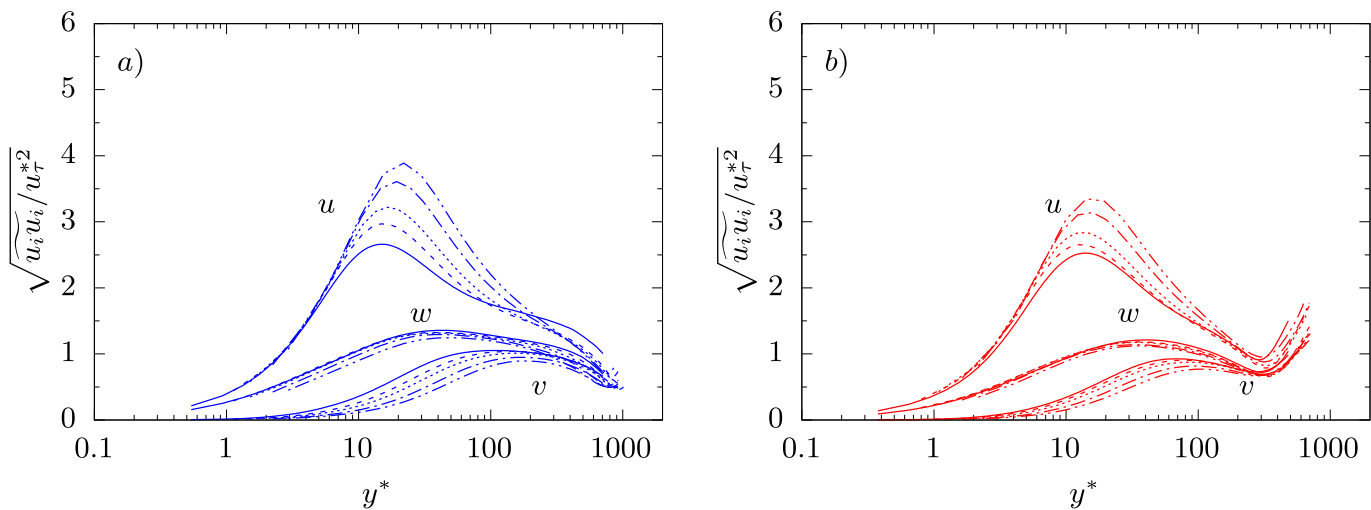


Fig. A.21. Reynolds stresses normalized with the semi-local friction velocity u_τ^* for case TCF55B at different grid levels: LvL0 (- · · · · ·), LvL1 (- · · · ·), LvL2 (· · · · ·), LvL3 (- - - -) and LvL4 (———). The cold and hot wall are presented in subfigure (a) and (b), respectively.

Appendix B. Additional thermodynamic properties

Mean viscosity distributions are presented in Fig. B.22 for the performed cases. The profiles are scaled with the values at the cold wall, respectively. The mean viscosity profiles have a strong decrease at the cold wall for all cases using the outer scaling in Fig. B.22(c). The viscosity drops by approximately 40% in the vicinity of the cold wall for all cases. In the channel centre these distributions feature a rather linear decrease towards the hot wall. This changes in the vicinity of the hot wall, where the profiles start to rise again, which leads to a viscosity minimum close to the wall. The viscosity distribution is also shown using the semi-local wall distance, in order to illustrate the behaviour close to the walls in Fig. B.22(a,b).

Appendix C. Look up tables

Thermodynamic and transport properties are extracted from the tabulated look-up database via trilinear interpolation. The look-up tables were created by using the block-structured adaptive mesh refinement method similar to Liu et al. (2014). A binary tree data structure is created to speed up the search within the tables, see Xia et al. (2007). The tables are refined until the error is below 1% or a maximum

refinement depth of 7 is reached. The temperature dependence of the density ρ , specific heat capacity at constant pressure c_p , dynamic viscosity μ and internal energy e of methane using the look-up table approach is depicted in Fig. C.23. The chosen pressure is 54.02 bar, which is close to the pressure of case TCF55B. As it can be observed, the tables are in good agreement with the NIST data base (Lemmon et al., 2013), that is used to evaluate the accuracy.

Appendix D. Autocorrelation

Kim et al. (2019) identified larger streamwise structures in their transcritical channel flow. The autocorrelation function (O'Neill et al., 2004) is used in order to identify if the channel size is sufficiently large in this study. The function is evaluated for all three velocity components, and in the stream- and spanwise direction at a wall distance of approximately at $y^+ = 20$ at the cold wall, see Fig. D.24. It can be observed, that all autocorrelations reach the vicinity of zero, indicating a decorrelated flow, thus, a channel size, which is suitable for this analysis.

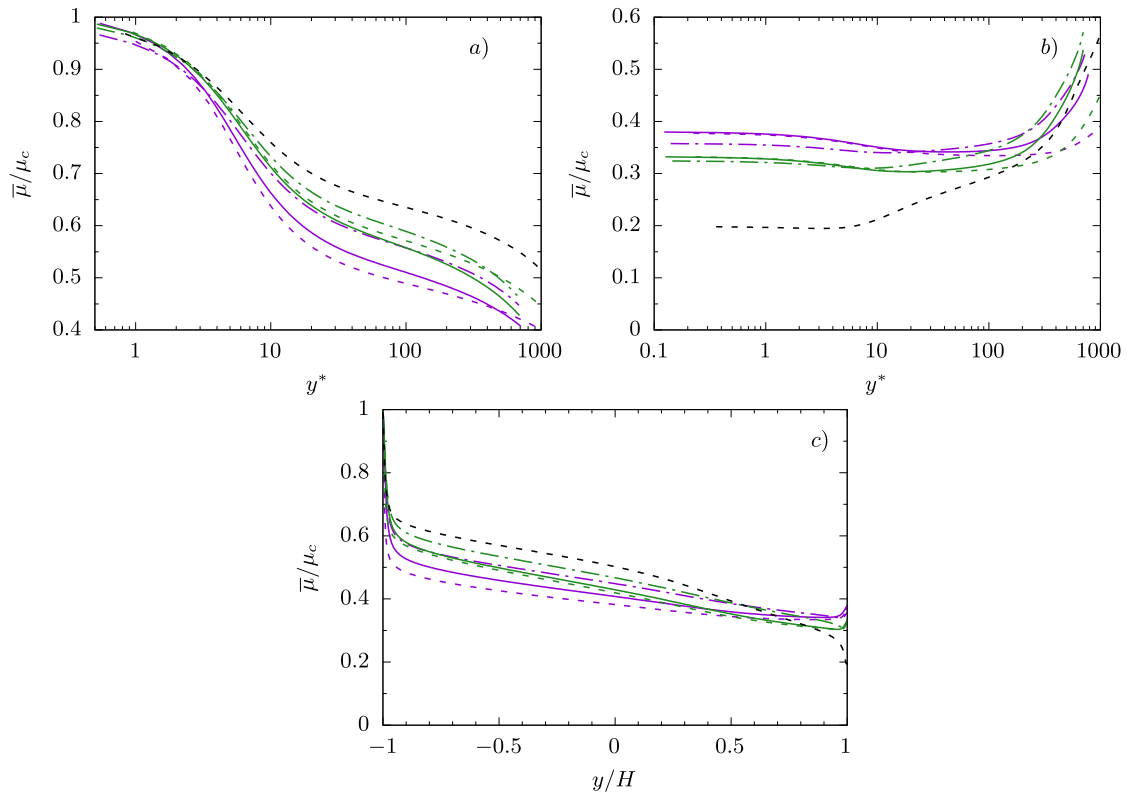


Fig. B.22. Mean viscosity distribution normalized with the viscosity at the cold wall. Overall distribution using the outer scale in (c). The viscosity profiles in the vicinity of the walls over semi-local wall units are presented for the cold wall (a) and hot wall (b).

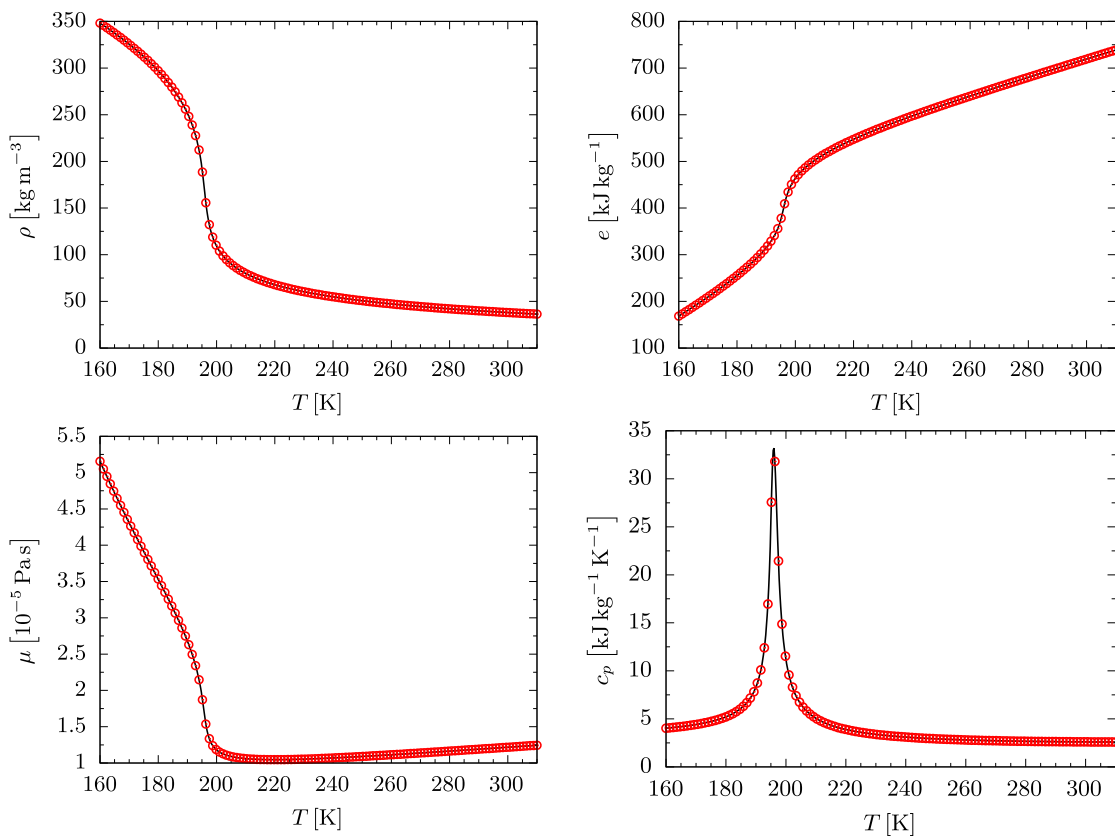


Fig. C.23. Thermodynamic properties of methane are calculated with the look-up table (\odot) and compared to the NIST reference data (—) at a pressure of $p = 54.02$ bar.

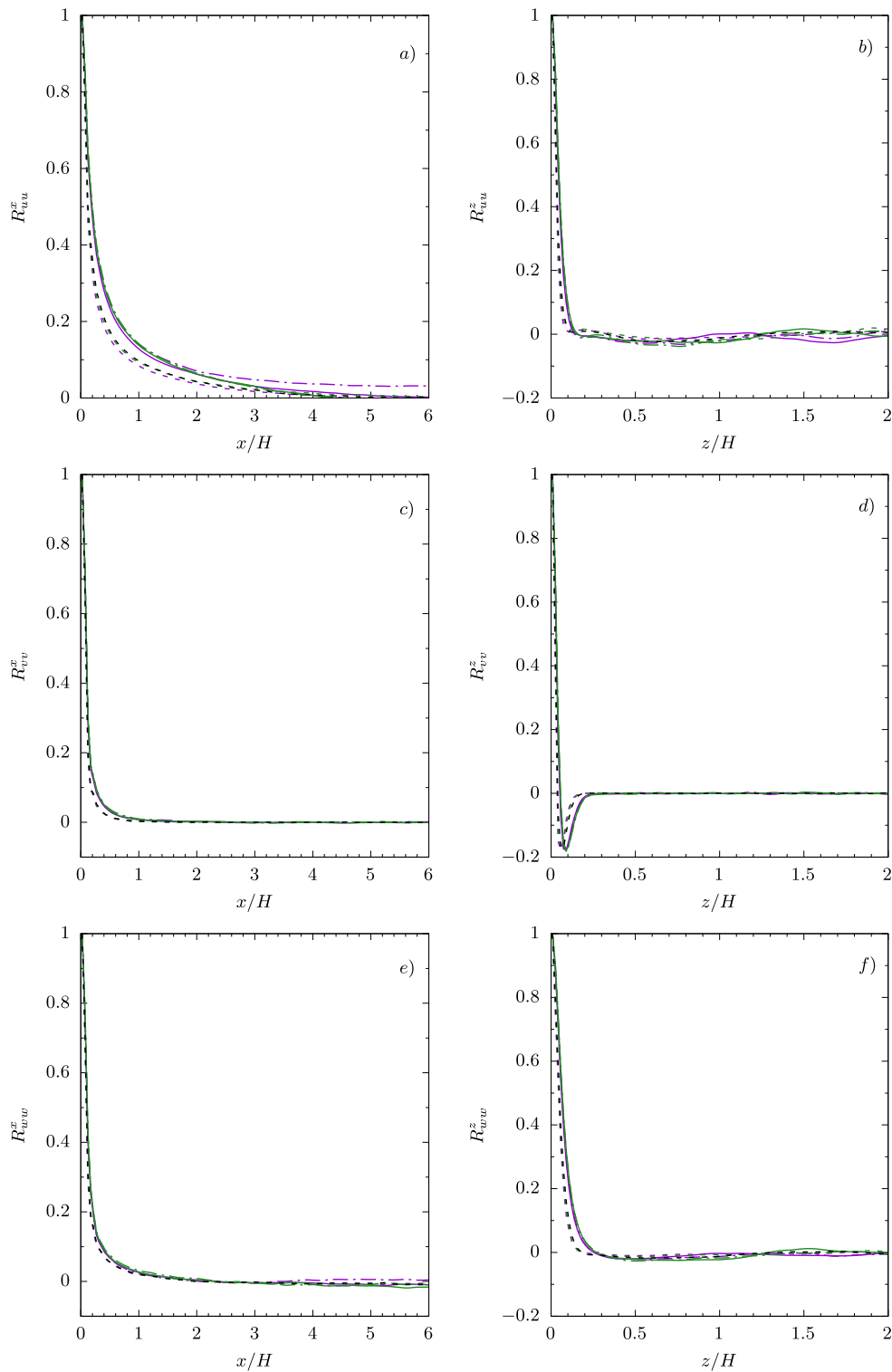


Fig. D.24. The autocorrelation function for all three velocity components u, v, w are presented in the streamwise and spanwise direction x and z , respectively. The position is $y^+ \approx 20$ at the cold wall.

References

Bai, T., Griffin, K.P., Fu, L., 2022. Compressible velocity transformations for various noncanonical wall-bounded turbulent flows. *AIAA J.* 60 (7), 4325–4337.

Brun, C., Boiarciuc, M.P., Haberkorn, M., Comte, P., 2008. Large eddy simulation of compressible channel flow. *Theor. Comput. Fluid Dyn.* 22, 189–212.

Chen, X., Sreenivasan, K.R., 2021. Reynolds number scaling of the peak turbulence intensity in wall flows. *J. Fluid Mech.* 908.

Chen, T., Yang, B., Robertson, M.C., Martinez-Botas, R.F., 2021. Direct numerical simulation of real-gas effects within turbulent boundary layers for fully-developed channel flows. *J. Glob. Power Propuls. Soc.* 5, 216–232.

Cheng, X., Kuang, B., Yang, Y., 2007. Numerical analysis of heat transfer in supercritical water cooled flow channels. *Nucl. Eng. Des.* 237 (3), 240–252.

Crua, C., Manin, J., Pickett, L.M., 2017. On the transcritical mixing of fuels at diesel engine conditions. *Fuel* 208, 535–548.

Doehring, A., Kaller, T., Schmidt, S.J., Adams, N.A., 2021. Large-eddy simulation of turbulent channel flow at transcritical states. *Int. J. Heat Fluid Flow* 89, 108781.

- Duan, L., Martín, M.P., 2010. Direct numerical simulation of hypersonic turbulent boundary layers. part 2. Effect of wall temperature. *J. Fluid Mech.* 655, 419–445.
- Ducros, F., Ferrand, V., Nicoud, F.C., Weber, C., Darracq, D., Gacherieu, C., Poinso, T., 1999. Large-Eddy simulation of the shock/turbulence interaction. *J. Comput. Phys.* 152 (2), 517–549.
- Dussauge, J.P., Fernholz, H., Smith, R., Saric, W.S., 1996. *Turbulent Boundary Layers in Subsonic and Supersonic Flow*. Citeseer.
- Egerer, C.P., Schmidt, S.J., Hickel, S., Adams, N.A., 2016. Efficient implicit LES method for the simulation of turbulent cavitating flows. *J. Comput. Phys.* 316, 453–469.
- Foysi, H., Sarkar, S., Friedrich, R., 2004. Compressibility effects and turbulence scalings in supersonic channel flow. *J. Fluid Mech.* 509, 207–216.
- Griffin, K.P., Fu, L., Moin, P., 2021. Velocity transformation for compressible wall-bounded turbulent flows with and without heat transfer. *Proc. Natl. Acad. Sci.* 118 (34), e2111144118.
- Guo, J., Yang, X., Ihme, M., 2022. Structure of the thermal boundary layer in turbulent channel flows at transcritical conditions. *J. Fluid Mech.* 934.
- Hickel, S., Adams, N.A., Domaradzki, J.A., 2006. An adaptive local deconvolution method for implicit LES. *J. Comput. Phys.* 213, 413–436.
- Hickel, S., Egerer, C.P., Larsson, J., 2014. Subgrid-scale modeling for implicit large eddy simulation of compressible flows and shock-turbulence interaction. *Phys. Fluids* 26.
- Hosseinpour, J., Howard, J., Chen, J., Engeda, A., 2022. Challenges for developing and marketing a brayton-cycle-based power genset gas turbine using supercritical CO₂ and a compressor design for simple recuperated cycle. *J. Energy Resour. Technol.* 144 (3).
- Huang, P.G., Coleman, G.N., Bradshaw, P., 1995. Compressible turbulent channel flows: DNS results and modelling. *J. Fluid Mech.* 185–218.
- Kaller, T., Doehring, A., Hickel, S., Schmidt, S.J., Adams, N.A., 2020. Assessment of RANS turbulence models for straight cooling ducts: Secondary flow and strong property variation effects. In: *Future Space-Transport-System Components under High Thermal and Mechanical Loads: Results from the DFG Collaborative Research Center TRR40*. Springer International Publishing Cham, pp. 309–321.
- Kaller, T., Pasquariello, V., Hickel, S., Adams, N.A., 2019. Turbulent flow through a high aspect ratio cooling duct with asymmetric wall heating. *J. Fluid Mech.* 860, 258–299.
- Kawai, S., 2019. Heated transcritical and unheated non-transcritical turbulent boundary layers at supercritical pressures. *J. Fluid Mech.* 865, 563–601.
- Kawai, S., Oikawa, Y., 2020. Turbulence modeling for turbulent boundary layers at supercritical pressure: A model for turbulent mass flux. *Flow Turbul. Combust.* 104 (2), 625–641.
- Kim, K., Hickey, J.P., Scalco, C., 2019. Pseudophase change effects in turbulent channel flow under transcritical temperature conditions. *J. Fluid Mech.* 871, 52–91.
- Kim, Y.M., Sohn, J.L., Yoon, E.S., 2017. Supercritical CO₂ rankine cycles for waste heat recovery from gas turbine. *Energy* 118, 893–905.
- Lee, J., Jung, S.Y., Sung, H.J., Tamer, A.Z., 2013. Effect of wall heating on turbulent boundary layers with temperature-dependent viscosity. *J. Fluid Mech.* 726, 196–225.
- Lee, M., Moser, R.D., 2015. Direct numerical simulation of turbulent channel flow up to. *J. Fluid Mech.* 774, 395–415.
- Lemmon, E.W., Huber, M.L., McLinden, M.O., 2013. NIST standard reference database 23: Reference fluid thermodynamic and transport properties-REFPROP, version 9.1. *Natl. Inst. Stand. Technol.*
- Li, F., Guo, J., Bai, B., Ihme, M., 2023. Analysis of real-fluid thermodynamic effects on turbulent statistics in transcritical channel flows. *Phys. Rev. Fluids* 8 (2), 024605.
- Liu, Z., Liang, J., Pan, Y., 2014. Construction of thermodynamic properties look-up table with block-structured adaptive mesh refinement method. *J. Thermophys. Heat Transfer* 28 (1), 50–58.
- Liu, J., Zhao, P., Lei, M., Yang, S., Nemat, H., 2020. Numerical investigation of spatial-developing turbulent heat transfer in forced convections at different supercritical pressures. *Int. J. Heat Mass Transfer* 159, 120128.
- Ma, P.C., Yang, X.I.A., Ihme, M., 2018. Structure of wall-bounded flows at transcritical conditions. *Phys. Rev. Fluids* 3 (3), 1–24.
- Matheis, J., Hickel, S., 2018. Multi-component vapor-liquid equilibrium model for LES of high-pressure fuel injection and application to ECN spray A. *Int. J. Multiph. Flow*. 99, 294–311.
- Mayer, W., Tamura, H., 1996. Propellant injection in a liquid oxygen/gaseous hydrogen rocket engine. *J. Propuls. Power* 12 (6), 1137–1147.
- Monin, A.S., Yaglom, A.M., 1975. *Statistical Fluid Mechanics: Mechanics of Turbulence*, Vol. 2. MIT Press.
- Morinishi, Y., Tamano, S., Nakabayashi, K., 2004. Direct numerical simulation of compressible turbulent channel flow between adiabatic and isothermal walls. *J. Fluid Mech.* 502, 273–308.
- Müller, H., Pfitzner, M., Matheis, J., Hickel, S., 2016. Large-eddy simulation of coaxial LN₂/GH₂ injection at trans-and supercritical conditions. *J. Propuls. Power* 32 (1), 46–56.
- Nemati, H., Patel, A., Boersma, B.J., Pecnik, R., 2015. Mean statistics of a heated turbulent pipe flow at supercritical pressure. *Int. J. Heat Mass Transfer* 83, 741–752.
- O'Neill, P.L., Nicolaides, D., Honnery, D., Soria, J., et al., 2004. Autocorrelation functions and the determination of integral length with reference to experimental and numerical data. In: *15th Australasian Fluid Mechanics Conference*, Vol. 1. University of Sydney, Sydney, NSW, Australia, pp. 1–4.
- Pasquariello, V., Grilli, M., Hickel, S., Adams, N.A., 2014. Large-eddy simulation of passive shock-wave/boundary-layer interaction control. *Int. J. Heat Fluid Flow* 49, 116–127.
- Patel, A., Boersma, B.J., Pecnik, R., 2016. The influence of near-wall density and viscosity gradients on turbulence in channel flows. *J. Fluid Mech.* 809, 793–820.
- Patel, A., Peeters, J.W.R., Boersma, B.J., Pecnik, R., 2015. Semi-local scaling and turbulence modulation in variable property turbulent channel flows. *Phys. Fluids* 27.
- Peeters, J.W., Pecnik, R., Rohde, M., Van Der Hagen, T., Boersma, B.J., 2016. Turbulence attenuation in simultaneously heated and cooled annular flows at supercritical pressure. *J. Fluid Mech.* 799, 505–540.
- Peeters, J., Sandham, N., 2019. Turbulent heat transfer in channels with irregular roughness. *Int. J. Heat Mass Transfer* 138, 454–467.
- Pirozzoli, S., Grasso, F., Gatski, T.B., 2004. Direct numerical simulation and analysis of a spatially evolving supersonic turbulent boundary layer at M=2.25. *Phys. Fluids* 16 (3), 530–545.
- Pizzarelli, M., 2018. The status of the research on the heat transfer deterioration in supercritical fluids: A review. *Int. Commun. Heat Mass Transfer* 95, 132–138.
- Pope, S.B., Pope, S.B., 2000. *Turbulent Flows*. Cambridge University Press.
- Schmidt, S.J., Sezal, I.H., Schnerr, G.H., 2006. Compressible simulation of high-speed hydrodynamics with phase change. In: *European Conference on Computational Fluid Dynamics*.
- Shahab, M.F., Lehnasch, G., Gatski, T.B., Comte, P., 2011. Statistical characteristics of an isothermal, supersonic developing boundary layer flow from DNS data. *Flow Turbul. Combust.* 86, 369–397.
- Simeoni, G.G., Bryk, T., Gorelli, F.A., Krisch, M., Ruocco, G., M., S., T., S., 2010. The Widom line as the crossover between liquid-like and gas-like behaviour in supercritical fluids. *Nat. Phys.* 6, 503–507.
- Smits, A.J., Dussauge, J.P., 2006. *Turbulent Shear Layers in Supersonic Flow*, second ed. Springer Science & Business Media, Inc.
- Terashima, H., Koshi, M., 2012. Approach for simulating gas-liquid-like flows under supercritical pressures using a high-order central differencing scheme. *J. Comput. Phys.* 231 (20), 6907–6923.
- Trettel, A., Larsson, J., 2016. Mean velocity scaling for compressible wall turbulence with heat transfer. *Phys. Fluids* 28 (2), 026102.
- van Driest, E.R., 1956. The problem of aerodynamic heating. *Aeronaut. Eng. Rev.* 15, 26–41.
- Volpiani, P.S., Iyer, P.S., Pirozzoli, S., Larsson, J., 2020. Data-driven compressibility transformation for turbulent wall layers. *Phys. Rev. Fluids* 5 (5), 052602.
- Wallace, J.M., 2016. Quadrant analysis in turbulence research: history and evolution. *Annu. Rev. Fluid Mech.* 48, 131–158.
- Wallace, J.M., Eckelmann, H., Brodkey, R.S., 1972. The wall region in turbulent shear flow. *J. Fluid Mech.* 54 (1), 39–48.
- Wensing, M., Vogel, T., Götz, G., 2016. Transition of diesel spray to a supercritical state under engine conditions. *Int. J. Engine Res.* 17 (1), 108–119.
- Willmarth, W., Lu, S., 1972. Structure of the Reynolds stress near the wall. *J. Fluid Mech.* 55 (1), 65–92.
- Xia, G., Li, D., Merkle, C.L., 2007. Consistent properties reconstruction on adaptive cartesian meshes for complex fluids computations. *J. Comput. Phys.* 225 (1), 1175–1197.
- Yoo, J.Y., 2013. The turbulent flows of supercritical fluids with heat transfer. *Annu. Rev. Fluid Mech.* 45 (1), 495–525.
- Zonta, F., Marchioli, C., Soldati, A., 2012a. Modulation of turbulence in forced convection by temperature-dependent viscosity. *J. Fluid Mech.* 697, 150–174.
- Zonta, F., Onorato, M., Soldati, A., 2012b. Turbulence and internal waves in stably-stratified channel flow with temperature-dependent fluid properties. *J. Fluid Mech.* 697, 175–203.
- Zonta, F., Soldati, A., 2018. Stably stratified wall-bounded turbulence. *Appl. Mech. Rev.* 70 (4).

BIBLIOGRAPHY

- [1] G. P. Sutton and O. Biblarz. *Rocket propulsion elements*. John Wiley & Sons, 2016.
- [2] D. K. Huzel and D. K. Huang. *Modern Engineering for Design of Liquid-Propellant Rocket Engines*. Vol. 147. Washington, DC: American Institute of Aeronautics and Astronautic, 1992.
- [3] O. J. Haidn. “Advanced rocket engines”. In: *Advances on propulsion technology for high-speed aircraft* 1 (2008), pp. 6–1.
- [4] F. Hötte, O. Günther, C. von Sethe, M. C. Haupt, P. Scholz, and M. Rohdenburg. “Lifetime Experiments of Regeneratively Cooled Rocket Combustion Chambers and PIV Measurements in a High Aspect Ratio Cooling Duct”. In: *Future Space-Transport-System Components under High Thermal and Mechanical Loads: Results from the DFG Collaborative Research Center TRR40*. Springer International Publishing Cham, 2020, pp. 279–293.
- [5] F. Gorelli, M. Santoro, T. Scopigno, M. Krisch, and G. Ruocco. “Liquidlike Behavior of Supercritical Fluids”. In: *Phys. Rev. Lett.* 97 (24 2006), p. 245702.
- [6] G. G. Simeoni, T. Bryk, F. A. Gorelli, M. Krisch, G. Ruocco, M. Santoro, and T. Scopigno. “The Widom line as the crossover between liquid-like and gas-like behaviour in supercritical fluids”. In: *Nature Physics* 6 (2010), 503 – 507.
- [7] D. T. Banuti. “Crossing the Widom-line - Supercritical pseudo-boiling”. In: *Journal of Supercritical Fluid* 98 (2015), pp. 12 –16.
- [8] D. Peng and D. B. Robinson. “A New Two-Constant Equation of State”. In: *Industrial & Engineering Chemistry Fundamentals* 15 (1976), pp. 59 –64.
- [9] E. W. Lemmon, M. L. Huber, and M. O. McLinden. “NIST Standard Reference Database 23: Reference Fluid Thermodynamic and Transport Properties-REFPROP, Version 9.1”. In: *National Institute of Standards and Technology* (2013).
- [10] B. E. Poling, J. M. Prausnitz, and J. P. O’Connell. *The Properties of Gases and Liquids*. Fifth Edition. McGraw-Hill, 2001.
- [11] J. R. Elliott and C. T. Lira. *Introductory chemical engineering thermodynamics*. Vol. 668. Prentice Hall Upper Saddle River, NJ, 2012.
- [12] T. Chung, M. Ajlan, L. L. Lee, and E. Starling. “Generalized Multiparameter Correlation for Nonpolar and Polar Fluid Transport Properties”. In: *Industrial & Engineering Chemistry Research* 27 (1988), pp. 671 –679.
- [13] U. Setzmann and W. Wagner. “A new equation of state and tables of thermodynamic properties for methane covering the range from the melting line to 625 K at pressures up to 1000 MPa”. In: *Journal of Physical and Chemical reference data* 20.6 (1991), pp. 1061–1155.

- [14] A. Doehring, S. J. Schmidt, and N. A. Adams. “Numerical investigation of transcritical turbulent channel flow”. In: *2018 Joint Propulsion Conference*. 2018, p. 4768.
- [15] A. Doehring, S. J. Schmidt, and N. A. Adams. “Momentum boundary layers in transcritical channel flows”. In: *International Journal of Heat and Fluid Flow* 103 (2023), p. 109201.
- [16] M. Pizzarelli. “The status of the research on the heat transfer deterioration in supercritical fluids: A review”. In: *International Communications in Heat and Mass Transfer* 95 (2018), pp. 132–138.
- [17] J. Y. Yoo. “The turbulent flows of supercritical fluids with heat transfer”. In: *Annual review of fluid mechanics* 45 (2013), pp. 495–525.
- [18] I. L. Pioro, H. F. Khartabil, and R. B. Duffey. “Heat transfer to supercritical fluids flowing in channels—empirical correlations (survey)”. In: *Nuclear engineering and design* 230.1-3 (2004), pp. 69–91.
- [19] J. H. Bae, J. Y. Yoo, and H. Choi. “Direct numerical simulation of turbulent supercritical flows with heat transfer”. In: *Physics of Fluids* 17.10 (2005), p. 105104.
- [20] J. H. Bae, J. Y. Yoo, and D. M. McEligot. “Direct numerical simulation of heated CO₂ flows at supercritical pressure in a vertical annulus at Re=8900”. In: *Physics of Fluids* 20.5 (2008), p. 055108.
- [21] H. Nemati, A. Patel, B. J. Boersma, and R. Pecnik. “Mean statistics of a heated turbulent pipe flow at supercritical pressure”. In: *International Journal of Heat and Mass Transfer* 83 (2015), pp. 741–752.
- [22] J. W. R. Peeters, R. Pecnik, M. Rohde, T. H. J. J. Van Der Hagen, and B. J. Boersma. “Turbulence attenuation in simultaneously heated and cooled annular flows at supercritical pressure”. In: *Journal of Fluid Mechanics* 799 (2016), pp. 505–540.
- [23] G. Ribert, D. Taieb, and V. Yang. “Large-eddy simulation of a supercritical channel flow using a shock capturing numerical scheme”. In: *Computers & Fluids* 117 (2015), pp. 103–113.
- [24] P. C. Ma, X. I. A. Yang, and M. Ihme. “Structure of wall-bounded flows at transcritical conditions”. In: *Physical Review Fluids* 3.3 (2018), pp. 1–24.
- [25] H. Terashima and M. Koshi. “Approach for simulating gas–liquid-like flows under supercritical pressures using a high-order central differencing scheme”. In: *Journal of Computational Physics* 231.20 (2012), pp. 6907–6923.
- [26] J. Matheis and S. Hickel. “Multi-component vapor–liquid equilibrium model for LES of high-pressure fuel injection and application to ECN Spray A”. In: *International Journal of Multiphase Flow* 99 (2018), pp. 294–311.
- [27] S. Kawai. “Heated transcritical and unheated non-transcritical turbulent boundary layers at supercritical pressures”. In: *Journal of Fluid Mechanics* 865 (2019), pp. 563–601.
- [28] E. R. van Driest. “The problem of aerodynamic heating”. In: *Aeronautical Engineering Review* 15 (1956), pp. 26–41.

-
- [29] P. G. Huang, G. N. Coleman, and P. Bradshaw. “Compressible turbulent channel flows: DNS results and modelling”. In: *Journal of Fluid Mechanics* (1995), pp. 185–218.
- [30] A. Trettel and J. Larsson. “Mean velocity scaling for compressible wall turbulence with heat transfer”. In: *Physics of Fluids* 28.2 (2016), p. 026102.
- [31] K. Kim, J.-P. Hickey, and C. Scalo. “Pseudophase change effects in turbulent channel flow under transcritical temperature conditions”. In: *Journal of Fluid Mechanics* 871 (2019), pp. 52–91.
- [32] T. Chen, B. Yang, M. C. Robertson, and R. F. Martinez-Botas. “Direct numerical simulation of real-gas effects within turbulent boundary layers for fully-developed channel flows”. In: *Journal of the Global Power and Propulsion Society* 5 (2021), pp. 216–232.
- [33] F. Li, J. Guo, B. Bai, and M. Ihme. “Analysis of real-fluid thermodynamic effects on turbulent statistics in transcritical channel flows”. In: *Physical Review Fluids* 8.2 (2023), p. 024605.
- [34] J. Guo, X. Yang, and M. Ihme. “Structure of the thermal boundary layer in turbulent channel flows at transcritical conditions”. In: *Journal of Fluid Mechanics* 934 (2022).
- [35] P. S. Volpiani, P. S. Iyer, S. Pirozzoli, and J. Larsson. “Data-driven compressibility transformation for turbulent wall layers”. In: *Physical Review Fluids* 5.5 (2020), p. 052602.
- [36] K. P. Griffin, L. Fu, and P. Moin. “Velocity transformation for compressible wall-bounded turbulent flows with and without heat transfer”. In: *Proceedings of the National Academy of Sciences* 118.34 (2021).
- [37] T. Bai, K. P. Griffin, and L. Fu. “Compressible velocity transformations for various noncanonical wall-bounded turbulent flows”. In: *AIAA Journal* 60.7 (2022), pp. 4325–4337.
- [38] G. Indelicato and F. Creta. “Assessment of an algebraic equilibrium wall-function for supercritical flows”. In: *International Journal of Heat and Mass Transfer* 197 (2022), p. 123350.
- [39] A. S. Monin and A. M. Yaglom. *Statistical Fluid Mechanics: Mechanics of Turbulence*. Vol. 2. MIT Press, 1975.
- [40] T. Kaller, A. Doehring, S. Hickel, S. J. Schmidt, and N. A. Adams. “Assessment of RANS Turbulence Models for Straight Cooling Ducts: Secondary Flow and Strong Property Variation Effects”. In: *Future Space-Transport-System Components under High Thermal and Mechanical Loads: Results from the DFG Collaborative Research Center TRR40*. Springer International Publishing, 2021, pp. 309–321. DOI: 10.1007/978-3-030-53847-7_20.
- [41] A. Doehring, T. Kaller, S. J. Schmidt, and N. A. Adams. “Large-eddy simulation of turbulent channel flow at transcritical states”. In: *International Journal of Heat and Fluid Flow* 89 (2021), p. 108781.
- [42] S. J. Schmidt. “A low Mach number consistent compressible approach for simulation of cavitating flows”. PhD thesis. Technische Universität München, 2015.
- [43] I. H. Sezal. “Compressible Dynamics of Cavitating 3-D Multi-Phase Flows”. PhD thesis. Technische Universität München, 2009.

BIBLIOGRAPHY

- [44] C. P. Egerer. “Large-Eddy Simulation of Turbulent Cavitating Flows”. PhD thesis. Technische Universität München, 2016.
- [45] ANSYS, Inc. *ANSYS Fluent, Release 19.2, HelpSystem, Theory Guide*.
- [46] ANSYS, Inc. *ANSYS Fluent, Release 19.2, HelpSystem, User’s Guide*.
- [47] C. Brun, M. P. Boiarciuc, M. Haberkorn, and P. Comte. “Large eddy simulation of compressible channel flow.” In: *Theoretical and Computational Fluid Dynamics* 22 (2008), pp. 189–212.
- [48] Z. Liu, J. Liang, and Y. Pan. “Construction of thermodynamic properties look-up table with block-structured adaptive mesh refinement method”. In: *Journal of Thermophysics and Heat Transfer* 28.1 (2014), pp. 50–58.
- [49] H. Burkhardt, M. Sippel, A. Herbertz, and J. Klevanski. “Kerosene vs Methane: A Propellant Tradeoff for Reusable Liquid Booster Stages”. In: *Journal of Spacecraft and Rockets* 41.5 (2004), pp. 762–769.
- [50] NIST. *National Institute of Standards and Technology*. 2023. URL: <http://webbook.nist.gov/chemistry/fluid>.
- [51] S. J. Schmidt, I. H. Sezal, and G. H. Schnerr. “Compressible simulation of high-speed hydrodynamics with phase change”. In: *European Conference on Computational Fluid Dynamics*. TU Delft, The Netherlands, 2006.
- [52] J. H. Ferziger and M. Peric. *Computational methods for fluid dynamics*. 2002.
- [53] C. P. Egerer, S. J. Schmidt, S. Hickel, and N. A. Adams. “Efficient implicit LES method for the simulation of turbulent cavitating flows”. In: *Journal of Computational Physics* 316 (2016), pp. 453–469.
- [54] F. Ducros, V. Ferrand, F. C. Nicoud, C. Weber, D. Darracq, C. Gacherieu, and T. Poinso. “Large-Eddy Simulation of the Shock/Turbulence Interaction”. In: *Journal of Computational Physics* 152.2 (1999), pp. 517–549.
- [55] S. Hickel, C. P. Egerer, and J. Larsson. “Subgrid-scale modeling for implicit large eddy simulation of compressible flows and shock-turbulence interaction”. In: *Physics of Fluids* 26 (2014).
- [56] B. Koren. *A robust upwind discretization method for advection, diffusion and source terms*. Vol. 45. Centrum voor Wiskunde en Informatica Amsterdam, 1993.
- [57] P. L. Roe. “Characteristic-based schemes for the Euler equations”. In: *Annual review of fluid mechanics* 18.1 (1986), pp. 337–365.
- [58] N. A. Adams, S. Hickel, and S. Franz. “Implicit subgrid-scale modeling by adaptive deconvolution”. In: *Journal of Computational Physics* 200.2 (2004), pp. 412–431.
- [59] S. Hickel, N. A. Adams, and J. A. Domaradzki. “An adaptive local deconvolution method for implicit LES”. In: *Journal of Computational Physics* 213 (2006), pp. 413–436.
- [60] E. R. Van Driest. “On turbulent flow near a wall”. In: *Journal of the aeronautical sciences* 23.11 (1956), pp. 1007–1011.

-
- [61] S. Hickel and N. A. Adams. “On implicit subgrid-scale modeling in wall-bounded flows”. In: *Physics of Fluids* 19.10 (2007).
- [62] W. M. Kays and M. E. Crawford. *Convective Heat and Mass Transfer*. 3rd. McGraw-Hill, Inc., 1993.
- [63] B. A. Kader. “Temperature and concentration profiles in fully turbulent boundary layers”. In: *International journal of heat and mass transfer* 24.9 (1981), pp. 1541–1544.
- [64] J. Larsson, S. Kawai, J. Bodart, and I. Bermejo-Moreno. “Large eddy simulation with modeled wall-stress: recent progress and future directions”. In: *Mechanical Engineering Reviews* 3.1 (2016), pp. 15–00418.
- [65] S. Pirozzoli. “Revisiting the mixing-length hypothesis in the outer part of turbulent wall layers: mean flow and wall friction”. In: *Journal of Fluid Mechanics* 745 (2014), 378–397.
- [66] Y. Y. Bae. “A new formulation of variable turbulent Prandtl number for heat transfer to supercritical fluids”. In: *International Journal of Heat and Mass Transfer* 92 (2016), pp. 792–806.
- [67] S. Kawai and Y. Oikawa. “Turbulence modeling for turbulent boundary layers at supercritical pressure: A model for turbulent mass flux”. In: *Flow, Turbulence and Combustion* 104.2 (2020), pp. 625–641.
- [68] A. S. Ghate and S. K. Lele. “Subfilter-scale enrichment of planetary boundary layer large eddy simulation using discrete Fourier–Gabor modes”. In: *Journal of Fluid Mechanics* 819 (2017), pp. 494–539.
- [69] A. S. Ghate and S. K. Lele. “Gabor mode enrichment in large eddy simulations of turbulent flow”. In: *Journal of Fluid Mechanics* 903 (2020), A13.
- [70] K. P. Griffin, L. Fu, and P. Moin. “Near-wall model for compressible turbulent boundary layers based on an inverse velocity transformation”. In: *Journal of Fluid Mechanics* 970 (2023), A36.
- [71] C. Hansen, X. I. A. Yang, and M. Abkar. “A POD-mode-augmented wall model and its applications to flows at non-equilibrium conditions”. In: *Journal of Fluid Mechanics* 975 (2023), A24. DOI: 10.1017/jfm.2023.857.
- [72] T. Kaller, V. Pasquariello, S. Hickel, and N. A. Adams. “Turbulent flow through a high aspect ratio cooling duct with asymmetric wall heating”. In: *Journal of Fluid Mechanics* 860 (2019), 258–299.